AD-A133 078 RAMAN-SHIFTED XECL LASER DEVELOPMENT FOR A SPACEBORNE BLUE-GREEN SOURCE..(U) NORTHROP RESEARCH AND TECHNOLOGY CENTER PALOS VERDES PENINSUL.. E A STAPPAERTS ET AL. 1/2

UNCLASSIFIED FEB 82 NRTC-82-5R N00123-80-C-1137 F/G 20/5 NL

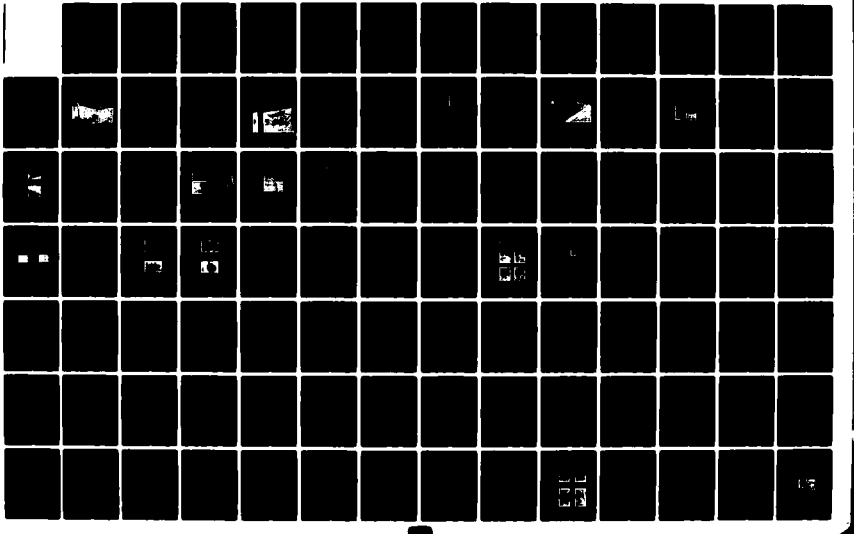

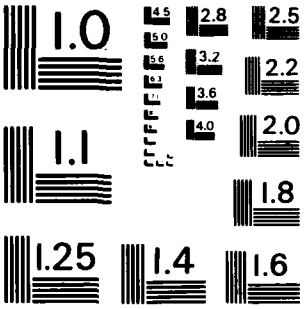

REPORT NRTC 82-5R

RAMAN-SHIFTED XeCl LASER DEVELOPMENT FOR A SPACEBORNE BLUE-GREEN SOURCE

E. A. Stappaerts, M. J. Plummer, W. H. Long, Jr., S. J. Brosnan, H. Komine, and J. B. West

Northrop Corporation
Northrop Research and Technology Center
One Research Park
Palos Verdes Peninsula, California 90274

February 1982

Interim Report for the Period July 1980 through May 1981

Prepared For:

NAVAL OCEAN SYSTEMS CENTER
271 Catalina Boulevard
San Diego, California 92152

The views and conclusions contained in this document are those of the authors and should not be interpreted as necessarily representing the official policies, either expressed or implied, of the Defense Advanced Research Projects Agency, the Naval Ocean Systems Center, or the U. S. Government.

SECURITY CLASSIFICATION OF THIS PAGE (When Data Entered)

REPORT DOCUMENTATION PAGE		READ INSTRUCTIONS BEFORE COMPLETING FORM
1. REPORT NUMBER NRTC 82-5R	2. GOVT ACCESSION NO.	3. RECIPIENT'S CATALOG NUMBER
4. TITLE (and Subtitle) Raman-Shifted XeCl Laser Development for a Spaceborne Blue-Green Source: Interim Report		5. TYPE OF REPORT & PERIOD COVERED Technical Report 6. PERFORMING ORG. REPORT NUMBER
7. AUTHOR(s) E. A. Stappaerts, M. J. Plummer, W. H. Long, Jr., S. J. Brosnan, H. Komine, J. West		8. CONTRACT OR GRANT NUMBER(s) N00123-80-C-1137
9. PERFORMING ORGANIZATION NAME AND ADDRESS Northrop Research and Technology Center One Research Park Palos Verdes Peninsula, CA 90274		10. PROGRAM ELEMENT, PROJECT, TASK AREA & WORK UNIT NUMBERS
11. CONTROLLING OFFICE NAME AND ADDRESS Naval Ocean Systems Center 271 Catalina Boulevard San Diego, CA 92152		12. REPORT DATE February, 1982 13. NUMBER OF PAGES 94
14. MONITORING AGENCY NAME & ADDRESS(if different from Controlling Office)		15. SECURITY CLASS. (of this report) UNCLASSIFIED 15a. DECLASSIFICATION/DOWNGRADING SCHEDULE

16. DISTRIBUTION STATEMENT (of this Report)

Approved for public release; distribution unlimited.

17. DISTRIBUTION STATEMENT (of the abstract entered in Block 20, if different from Report)

18. SUPPLEMENTARY NOTES

19. KEY WORDS (Continue on reverse side if necessary and identify by block number)

Laser, blue-green laser, excimer laser, XeCl laser, electric discharge laser, Raman conversion, Pb-vapor converter, electronic Raman scattering, experimental, theoretical.

20. ABSTRACT (Continue on reverse side if necessary and identify by block number)

This report describes work performed under the Navy/DARPA Submarine Laser Communications Program. Phase I of this program calls for a laboratory demonstration of a 1 joule laser source emitting in the 450-510 nm region of the spectrum with an efficiency of 1%. In order to meet these goals, Northrop Research and Technology Center has developed a Raman down-converted XeCl laser. Results of this experimental/theoretical research are summarized below:

DD FORM 1 JAN 73 1473 EDITION OF 1 NOV 65 IS OBSOLETE

SECURITY CLASSIFICATION OF THIS PAGE (When Data Entered)

TABLE OF CONTENTS

TABLE OF CONTENTS (CONTINUED)

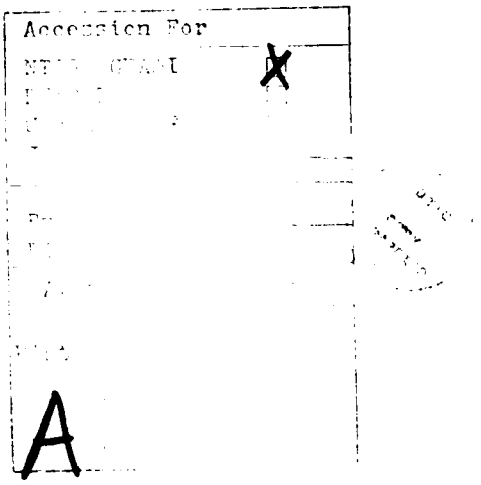

LIST OF FIGURES

LIST OF TABLES

1.0 INTRODUCTION AND SUMMARY

1.1 Introduction

This report is submitted in compliance with requirements of Navy Contract N00123-80-C-1137, which is part of the Navy/DARPA Submarine Laser Communications Program calling for development of a space-based blue-green laser for use in submarine communications. Phase I of this program specifies a laboratory demonstration of a 1 joule laser source emitting in the 450-510 nm region of the spectrum with an efficiency of 1%. In order to meet these goals, NRTC has developed a Raman down-converted XeCl laser. The results of this research are described in detail in this report.

During Phase I, a major breakthrough was achieved at NRTC by the demonstration of an efficiency in excess of two percent for the XeCl pump laser. In these experiments, an intrinsic efficiency of nearly 5% was also measured, indicating the possibility for considerable further improvements. The measured efficiency is in very good agreement with the value predicted by the NRTC XeCl laser performance code, run for the experimental conditions. Very encouraging is the prediction of the same code that an efficiency of 3 to 4% may be achieved in an optimized device. Significant advances in Raman conversion technology were also made at NRTC by demonstrating, for the first time, that energy conversion efficiencies in excess of 60% can be achieved at higher energies (joule level) using Pb vapor in an oscillator configuration.

Besides this Introduction and Summary, this report consists of four sections. Section 2 describes the Raman down-converted XeCl laser in detail. Section 3 describes the experimental results, Section 4 describes the XeCl laser computer model, and Section 5 is an analysis of the experimental results.

1.2 Summary

An electric-discharge pumped XeCl laser was designed, built, and tested. Stable self-sustained discharges for ~100 ns were obtained by using an adequate X-ray preionization, a fast risetime (10 ns) rail gap switch, and a constant voltage pulse provided by a water Blumlein. The water line was pulse

charged from primary storage capacitors through a spark gap. An important feature of the design was to provide for variable impedances for both the Blumlein and the discharge. This was essential to achieve a high laser efficiency by maximizing the power transfer from the driver to a matched load.

Laser tests were carried out using He and Ne diluents. The best results to date were obtained at 4 atm of Ne with 57 Torr Xe and 3.7 Torr HCl. With a charging voltage of 28 kV and a discharge volume of 4 x 4 x 90 cm, a laser output of 4.4 J was achieved with an efficiency of 2.1%, based on the energy stored in the PFN In subsequent experiments, using an unstable resonator, a laser linewidth of ≤ 0.01 nm was achieved by means of injection locking. Typically, a 10% increase in efficiency was observed upon injection locking, presumably due to a shortening of the laser build-up time. A near diffraction limited beam was obtained with the unstable resonator and careful sandblasting of the electrodes to reduce parasitics.

Extensive diagnostic tests were carried out to characterize the laser operation as well as to validate the comprehensive computer code. These studies conclusively showed that bottlenecking was not a significant problem in a XeCl laser and also that efficient pumping of the laser can be achieved through ionization of the excited Xe states at high pump densities. Excellent agreement was found between the observed results and the comprehensive code predictions under a variety of conditions, indicating the validity of the code. This code also predicts that under optimum conditions, a XeCl laser efficiency of 3% or possibly 4% may be achieved.

The injection locked XeCl laser output at 308 nm was down-converted to 459 nm by stimulated electronic Raman scattering in Pb vapor. First experiments were done using a high energy Raman oscillator cell of Pb vapor operated in the heat pipe mode at a temperature of 1238C. Stokes pulses approaching 1 J in energy were obtained, and excellent (91%) pump depletion was observed, yielding an energy conversion of 63% as compared with the quantum limit of 67%. A somewhat lower 50% energy conversion was measured from direct output/input measurements. This is due to the divergence of the Stokes beam that is inherent in the high energy oscillator approach. To eliminate this problem, the

Stokes output from a low energy, high beam quality oscillator cell was injected into a power amplifier cell and an energy conversion of 50% was again obtained in an output Stokes wave of much improved optical quality. This already high efficiency and performance may be increased by further improving the pump laser beam quality.

2.0 PHASE I DEVICE CONFIGURATION

The Phase I device is composed of two major subsystems, the XeCl laser and the Raman converter. The XeCl laser is an electric discharge laser which emits pulsed energy in the ultraviolet portion of the spectrum at 308 nm. Injection locking is used to control the output wavelength and improve beam quality as well as to enhance efficiency. The Raman converter is composed of two lead vapor cells which, through the Raman effect, convert the ultraviolet output of the XeCl laser to 459 nm in the blue-green portion of the spectrum. The two cells are used in an oscillator-amplifier configuration which yields high conversion efficiency with good beam quality and high power handling capability.

2.1 XeCl Laser

The XeCl laser has six major components. These are: (1) X-ray preionizer, (2) discharge cavity, (3) injection locking and optical resonator system, (4) Blumlein pulse forming network, (5) rail gap switch, and (6) primary energy store. Except for the injection locking and optical resonator system, these components will be described in detail below, along with their operating characteristics. The injection locking and optical resonator system will be described in Section 2.2. Figure 2.1-1 shows an overall view of the XeCl laser device.

Operation of the laser is best explained with reference to the system schematic, Figure 2.1-2. The primary energy storage capacitors, C_1, are initially charged to a DC voltage, V_o, of from 25 kV to 40 kV through resistors, R_1 and R_2. The two-stage Marx bank is also initially charged to 50 kV DC. Spark gap, SG, is then triggered, temporarily grounding one side of capacitors, C_1. Charge then flows from capacitors, C_1, to the Blumlein PFN. In this case, the Blumlein PFN approximates two capacitors of capacitance, C_B. Capacitors, C_1, are chosen equal to C_B. The voltage across the Blumlein, V_B, is given by

$$V_B = V_o \left(\frac{C_1}{C_1 + C_B} \right) (1 - \cos \omega t)$$

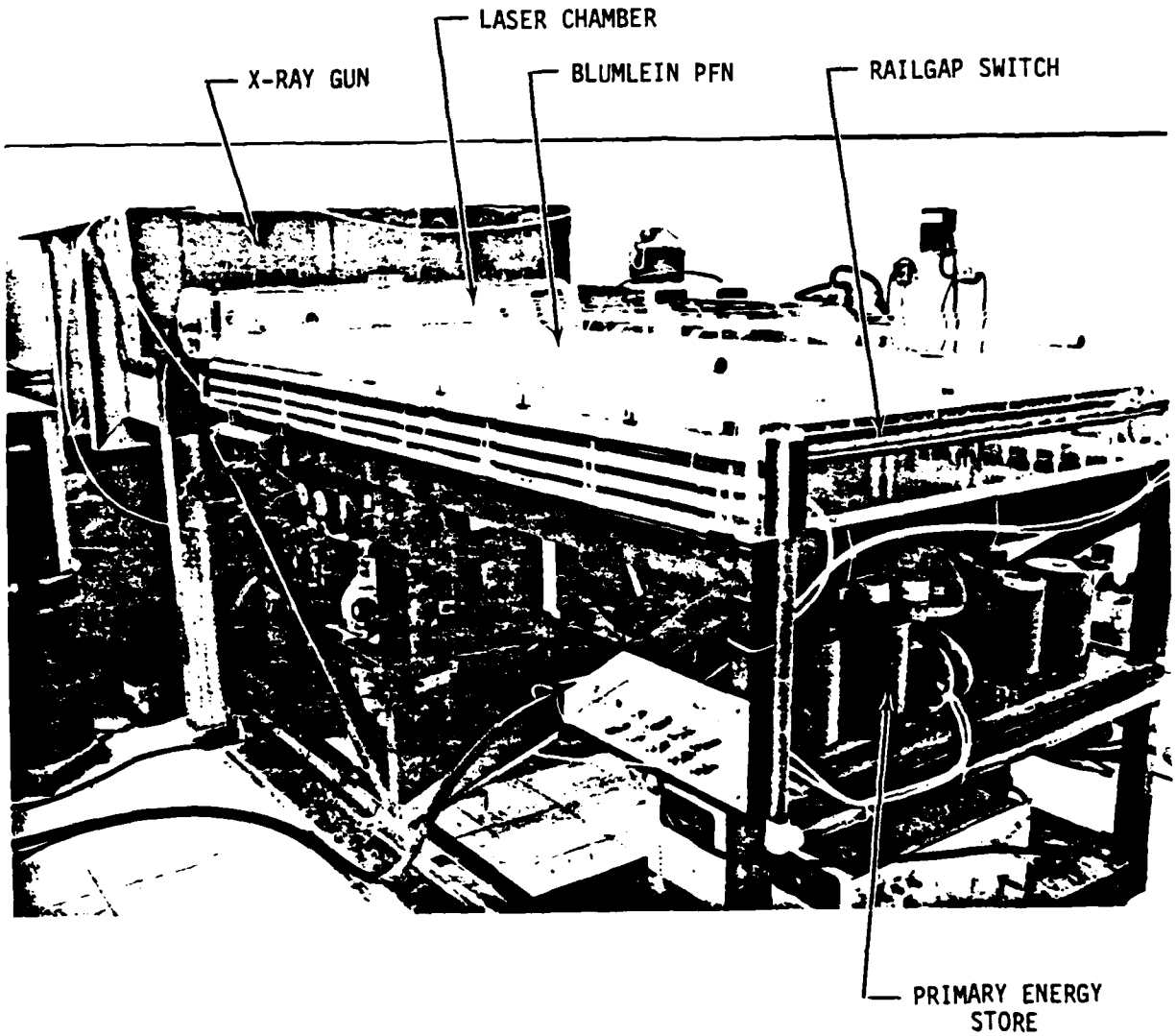

FIGURE 2.1-1 OVERALL VIEW OF XeCl LASER SYSTEM

$$\omega = \left[\frac{1}{L_1} \left(\frac{1}{C_1} + \frac{1}{C_B} \right) \right]^{\frac{1}{2}} .$$

For $C_1 = C_B$, V_B reaches a maximum of V_o at time

$$\tau = \frac{\pi}{\omega} = \pi \left(\frac{L_1 C_1}{2} \right)^{\frac{1}{2}} .$$

At this time (~1.2 μs), the X-ray gun is triggered emitting a 50 ns to 100 ns X-ray pulse. The X-rays ionize the gas in the laser cavity to a low level ($< 10^9$ electrons/cm^3) and also initiate breakdown of the rail gap switch, RG.

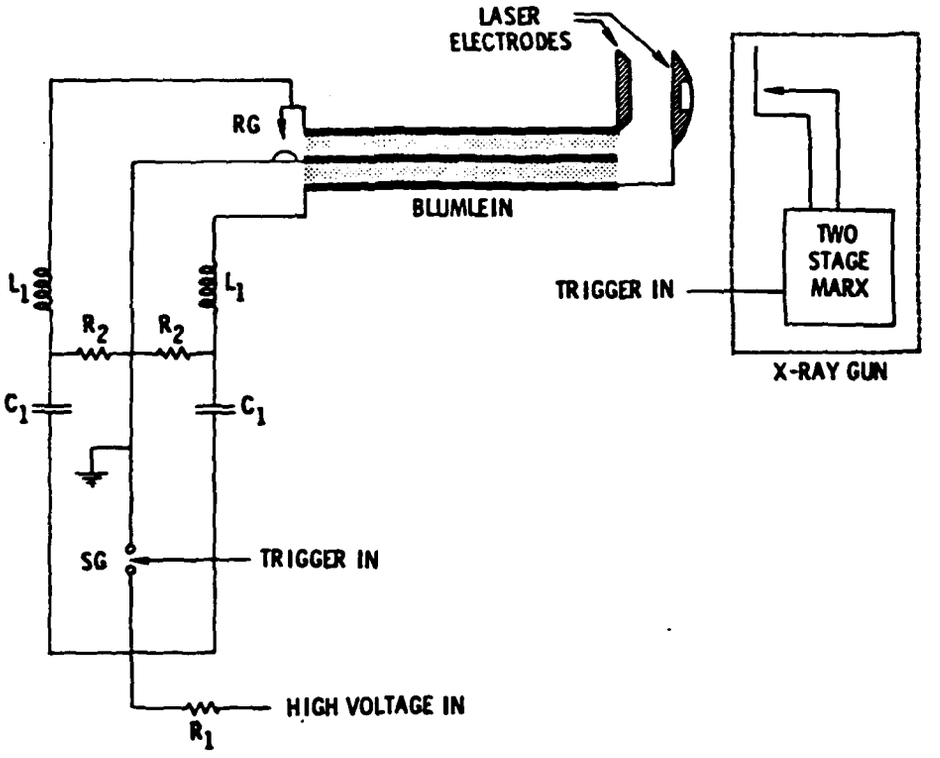

FIGURE 2.1-2 SYSTEM SCHEMATIC

The rail gap switch closes in about 10 ns, shorting the upper Blumlein transmission line. This short results in the propagation of a wave down the upper line towards the electrodes removing the voltage on the line. When this wave reaches the electrodes, it initially encounters a large impedance (effectively infinite compared to the line impedance). To preserve the boundary conditions at the end of the line, a voltage reflection is required which causes a reversal of the voltage on the top part of the line. As the bottom part of the line is undisturbed at this point, the voltage reversal on the top of the line causes the impression of a voltage difference of 2 V_o across the electrodes. Due to the applied voltage, a rapid avalanche of the initial ionization takes place in the gas reaching a quasi-steady-state value determined by the balance of the ionization processes with recombination and attachment loss processes. This balance determines the steady-state operating voltage, V_{ss}, of the discharge and is a function of only the gas mixture, gas density, and electrode gap spacing. As the gas breaks down, current is drawn from the Blumlein PFN. A quasi-steady-state value of current, I_{ss}, is reached which is determined by

$$I_{ss} = \frac{2V_o - V_{ss}}{2 Z_o}$$

where Z_o is the impedance of one side of the Blumlein PFN.

This quasi-steady-state voltage and current lasts for the two-way transit time of 120 ns of the Blumlein PFN during which the energy of the PFN is transferred to the discharge. The efficiency of transfer depends on how well the PFN impedance matches the discharge impedance. As power is transferred to the gas, a population inversion is created, eventually reaching threshold and lasing commences.

2.1.1 X-Ray Preionizer. The X-ray preionizer is a converted electron beam gun of NRTC design and construction. Figure 2.1-3 is a photograph of the unit showing the 5 cm by 100 cm e-beam window. The cold cathode electron gun is driven by a two-stage Marx generator with a peaking capacitor. These circuits are located in an oil tank behind the electron gun. Figure 2.1-4 is a schematic of the Marx circuit and electron gun diode. Two high voltage

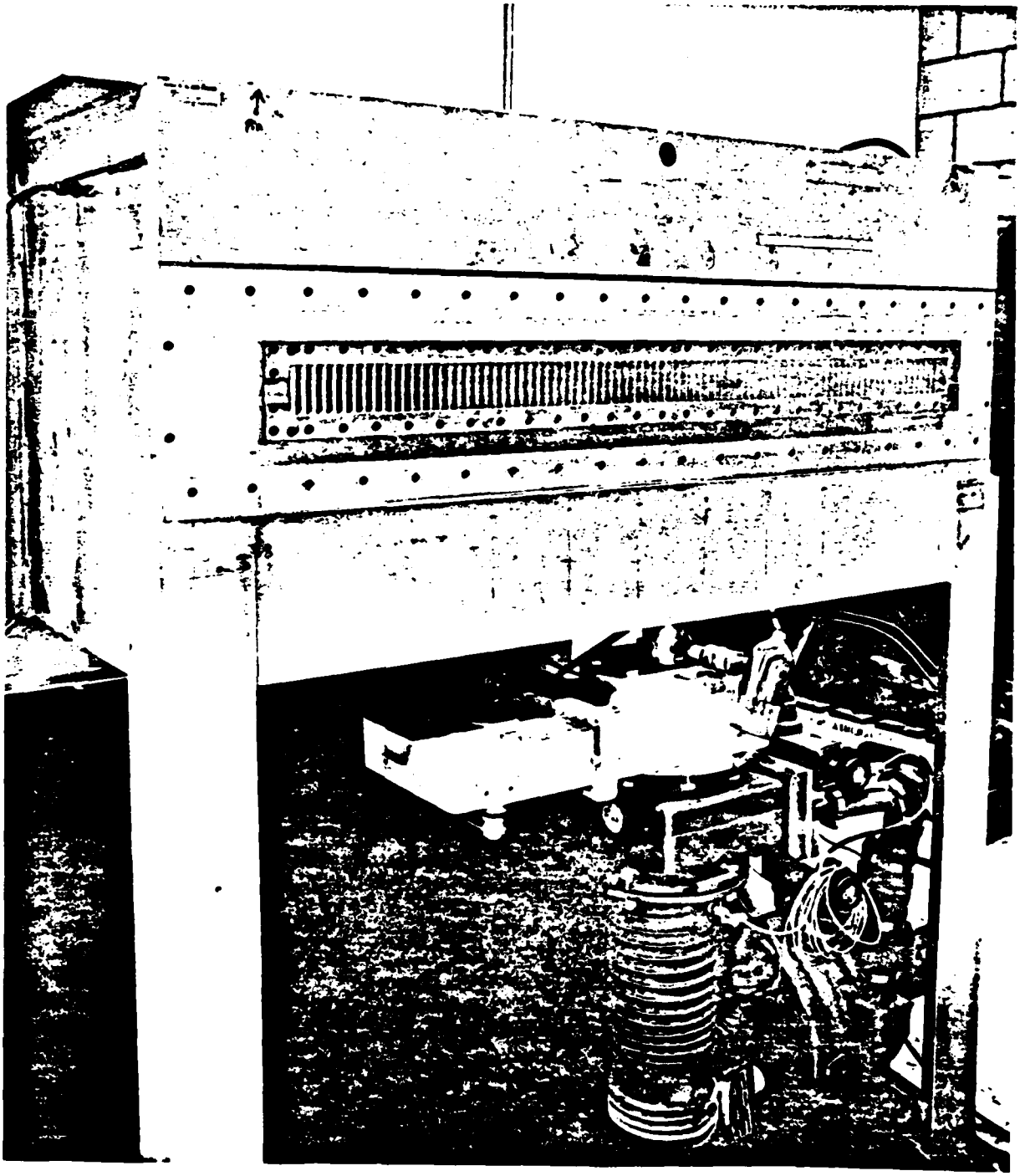

FIGURE 2.1-3 X-RAY GUN

78-19

feedthroughs connect the Marx circuit to the e-gun diode, which has an anode-cathode spacing adjustable between 2 and 5 cm. The Marx bank is command triggered with a pulse to the first spark gap. The second gap breaks down due to an overvoltage condition.

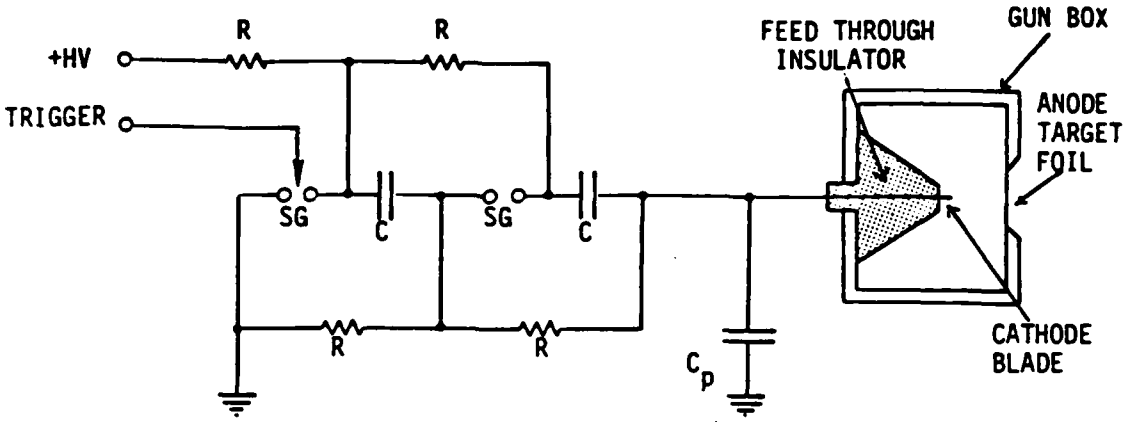

C MARX CAPACITOR, 0.06 μf

C_p PEAKING CAPACITOR, 0.86 nf

R CHARGING RESISTOR

SG SPARK GAP

FIGURE 2.1-4 X-RAY GUN SCHEMATIC

For use as an X-ray generator, the thin, titanium e-beam foil window is replaced by a 25 μm thick tantalum target. A 0.25 mm thick aluminum window is used as a pressure-bearing component to remove mechanical stresses from the thin tantalum target.

Operating characteristics of the X-ray gun are summarized below. The gun is operated at 50 kV charging voltage on the Marx bank which gives approximately 120 kV on the diode at peak voltage. Dosimeter measurements taken at the foil window give from 60 to 130 mR, depending on the dosimeter used. This is equivalent to about 10^8 ion pairs in air. Figure 2.1-5 shows peak X-ray flux measurements obtained with a silicon pin diode used as a detector. One set is taken with the detector within a centimeter of the foil window while

the other set is taken with the detector at the centerline of the laser chamber without the chamber in place. These measurements illustrate the smoothing of the flux obtained with distance. With the cavity in place, further smoothing would take place due to scattering by the acrylic cavity wall and the aluminum electrode. Figure 2.1-6 is an oscilloscope trace obtained with a silicon pin diode showing the time history of the X-ray flux.

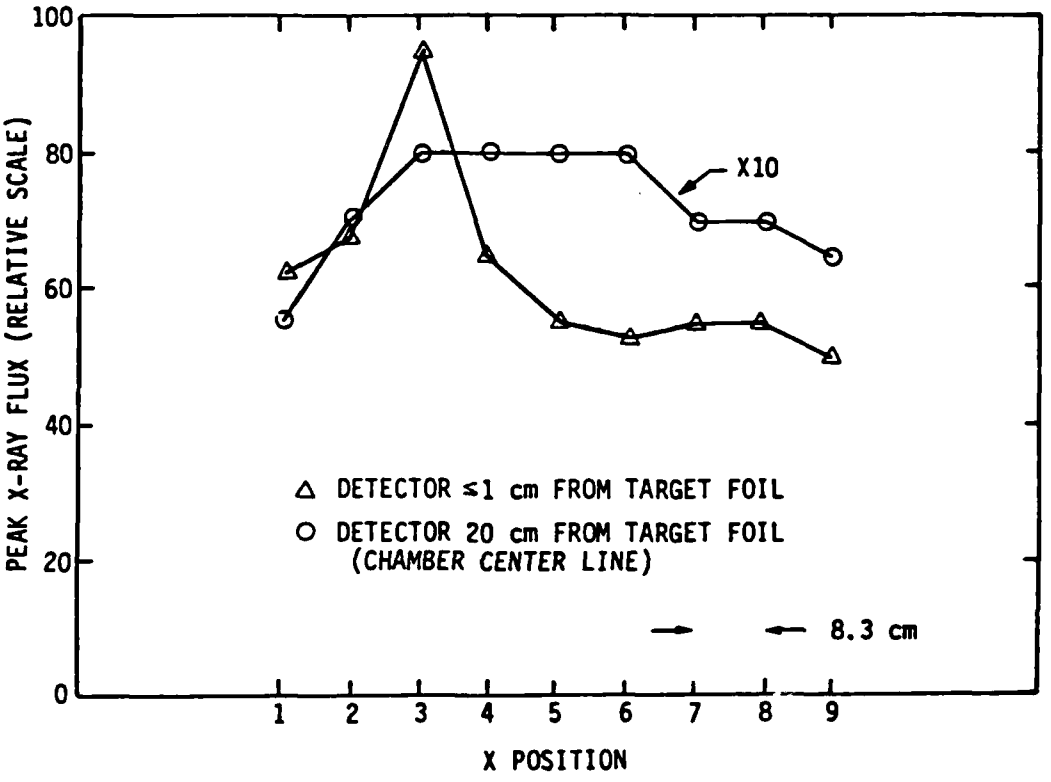

FIGURE 2.1-5 X-RAY FLUX DISTRIBUTION

2.1.2 Discharge Cavity. The discharge cavity is a cylindrical acrylic chamber with aluminum end plates. The chamber is 119 cm long and 17 cm in diameter with a 0.95 cm wall thickness. Optical windows or mirrors can be mounted on the aluminum end plates. Optics up to 10 cm in diameter can be accommodated with an 8.9 cm clear aperture. Design pressure is 5 atmospheres absolute. Figure 2.1-7 is a cross sectional view of the discharge chamber as it mounts on the Blumlein PFN, and Figure 2.1-8 is a photograph of the chamber mounted on the PFN.

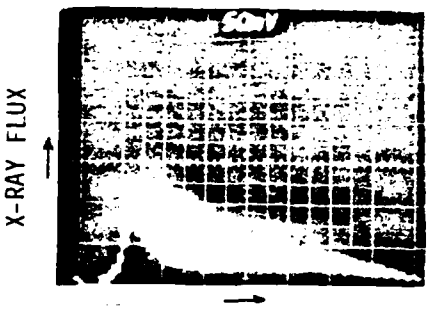

FIGURE 2.1-6 OSCILLOSCOPE TRACE OF X-RAY FLUX

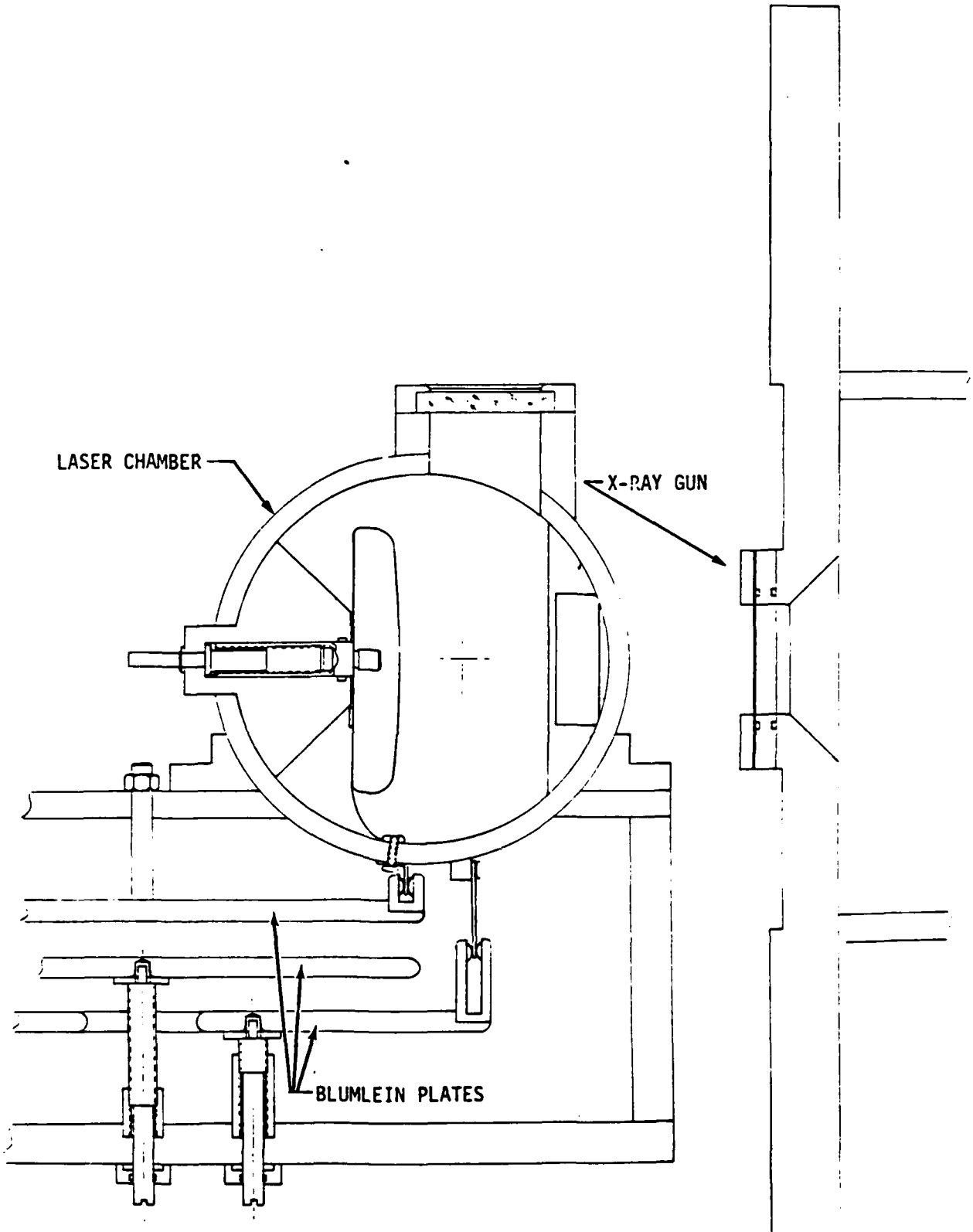

FIGURE 2.1-7 CROSS SECTIONAL VIEW-LASER CHAMBER & BLUMLEIN PFN

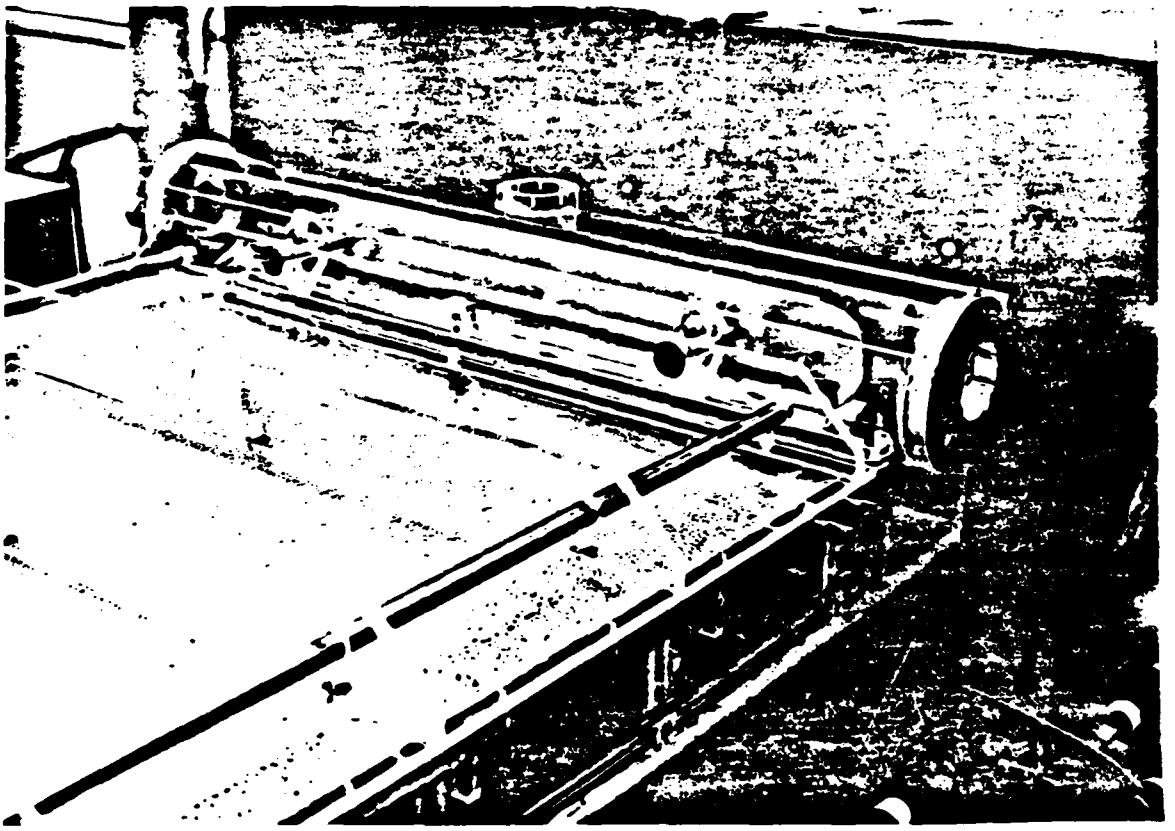

FIGURE 2.1-8 LASER CHAMBER - MOUNTED ON BLUMLEIN

The electrodes are both made of aluminum. The anode has a Chang profile [Ch73] in order to obtain a uniform electric field. It mounts on two studs which are driven in and out by a threaded adjusting mechanism. This allows adjustment of the electrode spacing without having to open the chamber to the atmosphere. The cathode has a flat surface. Its back side is radiused to match the chamber inside diameter to which it is bolted directly. A rectangular pocket is machined out of the back side to improve X-ray transmission. The minimum thickness traversed by the X-rays is 3.2 mm. The electrodes are designed for a nominal 5 cm X 5 cm X 90 cm discharge volume. A maximum electrode gap spacing of 7.2 cm may be obtained through the adjusting mechanism. Figure 2.1-9 shows an end view of the laser chamber with the end plates removed. The electrode shapes and adjusting mechanism are visible in this view.

Electrical feed to the electrodes from the Blumlein PFN is designed to minimize the inductance of this part of the circuit. Figure 2.1-7 shows these electrical connections. The anode is fed from the top Blumlein plate. The end of the Blumlein plate has a slotted contact block which is contacted by a copper strip with spring finger stock. Both the copper strip and contact block are full width of the Blumlein plate (90 cm). The copper strip is bolted to the acrylic cavity with eighteen screws which also serve as electrical feedthroughs. The screws engage another copper strip on the inside of the cavity which then extends in an arc up to the anode to which it is bolted. This strip is also 90 cm wide. Similarly, the cathode is fed from the bottom Blumlein plate by another copper strip with spring finger stock engaging a slotted contact block. In this case, the contact block has a deep slot to allow the lower Blumlein plate to be adjusted up and down in order to change the Blumlein plate spacing. The copper strip extends up to the chamber and engages another copper strip that follows the outside diameter of the chamber around to the point where the cathode is bolted to the chamber by eighteen screws. These screws also serve as electrical feedthroughs. As in the case of the anode connection, the contact block and copper strips are 90 cm wide. This electrical feed arrangement has a geometrical inductance of 10 nH, depending on electrode and Blumlein spacing.

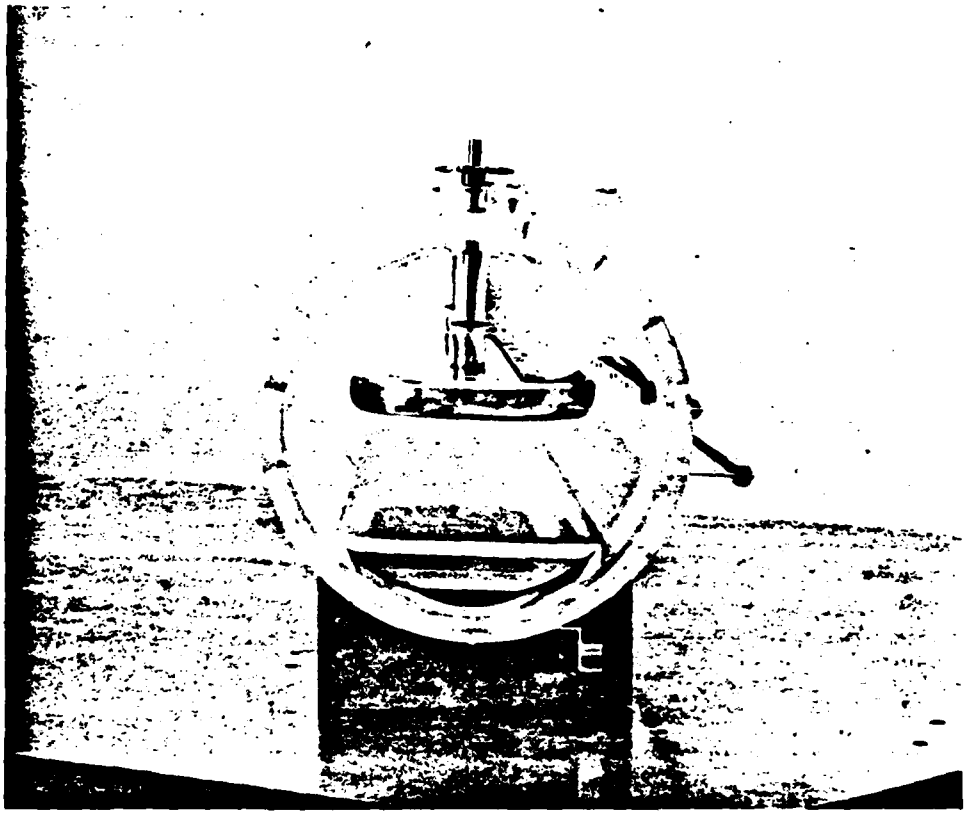

FIGURE 2.1-9 LASER CHAMBER - END VIEW

2.1.3 Blumlein Pulse Forming Network. A Blumlein PFN is used for electrical excitation which allows efficient quasi-steady-state operation of the discharge at nearly constant discharge voltage and current. A water dielectric is used because of its high dielectric constant which results in a compact design and because of its excellent dielectric strength for short pulse excitation. Furthermore, electrical breakdown through the water is self healing. The Blumlein PFN is constructed with variable plate spacing so that the impedance of the PFN may be changed to better match the discharge impedance.

Blumlein construction is illustrated in Figure 2.1-7. Three aluminum plates are suspended in the water dielectric which is contained in an acrylic box. The top plate is hung from the top and is stationary while the bottom two plates are supported on adjustable posts from the bottom. Spacing is changed by screwing these posts up or down.

Important parameters for the Blumlein PFN are summarized in Table 2.1-1. They are based on a dielectric constant of 80 for the water. The 200 cm PFN length gives a 120 ns long discharge excitation pulse. The impedance and capacitance values given correspond to the minimum (4 mm) and maximum (16 mm) plate spacings, respectively. Minimum spacing is based on breakdown at 40 kV. Closer spacings or lower impedance can be obtained at lower charging voltages.

TABLE 2.1-1 BLUMLEIN PARAMETERS

Dimensions	90 cm Wide X 200 cm Long
Two Way Transit - Time	120 ns
Decay Time Constant	35 μs (ρ = 5 MΩ cm)
Plate Separation	4 mm to 16 mm
Impedance	.38Ω to 1.5Ω
Capacitance	640 nF to 160 nF
Stored Energy	512 J to 128 J (V_o = 40 kV)
Break Down Limit on Storage Time	1.2 μs to 74 μs (V_o = 40 kV)

Water resistivity is maintained by a deionizer system. Aluminum Blumlein parts are nickel plated and copper parts are either nickel plated or gold plated to reduce ionic contamination of the water. Resistivities of 5 MΩ-cm were achieved upon initital operation, but the resistivity has deteriorated to about 1.5 MΩ-cm as the system has slowly become contaminated. With a thorough cleaning and a faster flow rate between the plates, water resistivities of 10 MΩ-cm or greater should be achieved.

Figure 2.1-10a shows the voltage ringup of the Blumlein plates illustrating the 1 - cos ωt behavior of the voltage transfer from the primary energy storage capacitor. In this case, the rail gap is pressurized with two atmospheres of nitrogen so that it will not self fire. Time to peak voltage is 1.2 μs. Figure 2.1-10b shows the voltage ringup on a longer time scale. In this trace, the voltage decay due to the finite resistance of the water is evident. The decay time constant is 9.6 μs which corresponds to a water resistivity of 1.4 MΩ-cm, in agreement with the measured range of 1.3 MΩ-cm to 1.6 MΩ-cm. This decay results in an 8% loss of the energy stored on the primary capacitor. This loss could be reduced to 2.6% for a water resistivity of 5 MΩ-cm and to 1.3% for a resistivity of 10 MΩ-cm.

2.1.4 Rail Gap Switch. A rail gap switch is used to short one side of the Blumlein PFN and thereby initiate electrical excitation of the gas. This type of switch is well suited to this application because of its low inductance and excellent geometric match to a flat plate type transmission line such as a Blumlein PFN. Low inductance is achieved through multiple spark channel operation. This multi-channel operation also lends itself to long life through distribution of the current among many channels over a large area. Such a switch also has low losses due to a short resistive phase as compared to a spark gap.

A cross sectional view of the rail gap switch mounted on the Blumlein PFN is shown in Figure 2.1-11. The switch consists of a 1.9 cm diameter brass anode and a 0.25 mm thick stainless steel blade cathode mounted in an acrylic box. Both electrodes are 82 cm long. The anode to cathode spacing

(a)

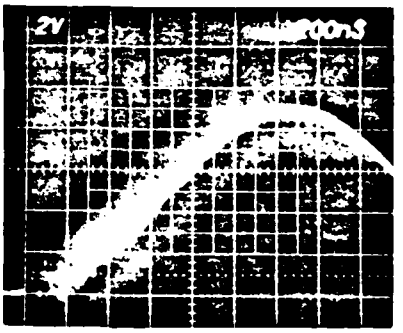

(b)

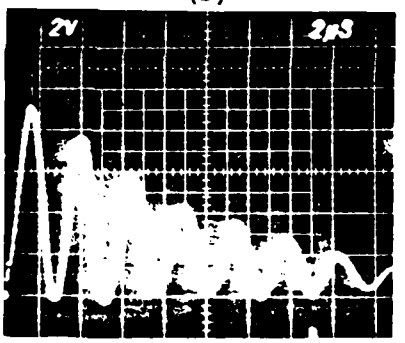

FIGURE 2.1-10 OSCILLSCOPE TRACES OF VOLTAGE RINGUP OF BLUMLEIN PLATES

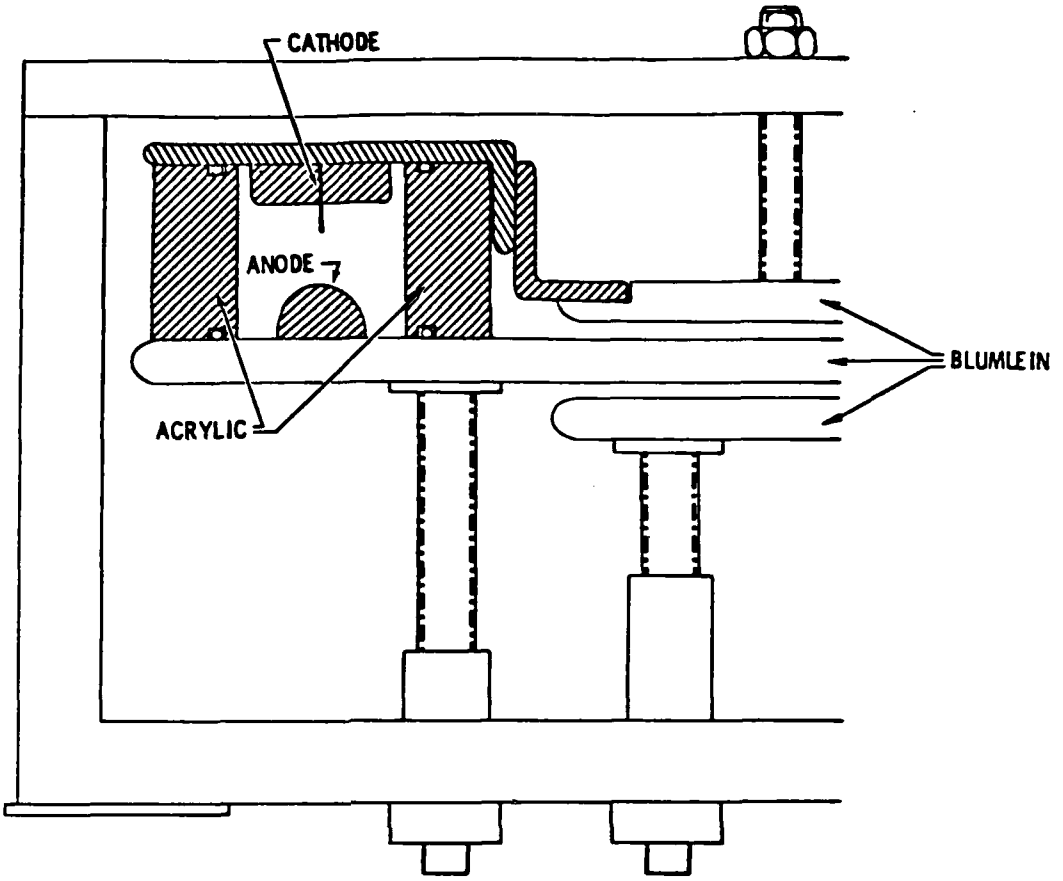

FIGURE 2.1-11 RAILGAP SWITCH CROSS SECTION

is 5.4 mm. The middle Blumlein plate forms the bottom of the switch box, and the top of the switch box serves as part of the electrical connection to the top Blumlein plate.

Untriggered multi-channel operation of the switch has been achieved with voltage fall times (resistive phase) of the order of 10 ns or less. However, it was found that the rail gap switch was being triggered by X-rays when the switch was operated in conjunction with operation of the X-ray gaun. Subsequent investigation of this triggering action revealed that the triggering was reliable and reduced the jitter of the switch operation from about 50 ns to 20 ns or less. Since it was difficult to shield the switch against the X-rays, it was decided to take advantage of the X-rays as a trigger. This is

possible because there is a 60 ns delay between the firing of the rail gap switch and the application of any voltage to the discharge electrodes. This delay is due to the transit time of the voltage wave from the switch down the Blumlein to the laser cavity. The delay allows adequate preionization of the gas by the X-rays if the X-ray flux has a fast enough risetime. An X-ray flux risetime of 25 ns was achieved by addition of peaking capacitors to the X-ray gun Marx bank. Reliable discharge operation was obtained with this arrangement.

Figure 2.1-12 shows a close up view of the rail gap switch. The bar anode is visible on the bottom and the blade cathode is visible on the top. Multi-channel operation is shown in Figure 2.1-13. There is approximately one arc channel per centimeter. An oscilloscope trace of the rail gap voltage is shown in Figure 2.1-14. As indicated in the figure, the resistive fall time is about 6 ns in agreement with Martin's [Ma70] empirical formula.

2.1.5 Primary Energy Store. The primary energy store is a simple capacitive energy store. The capacitors used are high quality paper-plastic film type and of low inductance design. Each capacitor, C_1, (refer to system schematic, Figure 2.1-2) is made up of four individual capacitors with values chosen so that a range of values of Blumlein capacitance can be matched. They are charged through resistors, R_1 and R_2, using a conventional DC high voltage power supply. The spark gap, SG, used to initiate Blumlein PFN charging is a triggered gap. (Physics International Model 670). The PFN charging inductors, L_1, consist of the inherent inductance of the connecting circuitry which is trimmed and balanced by wire length.

2.2 Optical Resonator and Injection Locking Configurations. To control the beam divergence of the laser to within the tolerance required for the blue-green laser system, an injection-locked, positive-branch confocal unstable resonator was used.

The resonator, shown in Figure 2.2-1 has several pertinent features. A scraper mirror, consisting of a highly reflecting central rectangle, forms the corner of an L-shaped resonator. This geometry has several advantages:

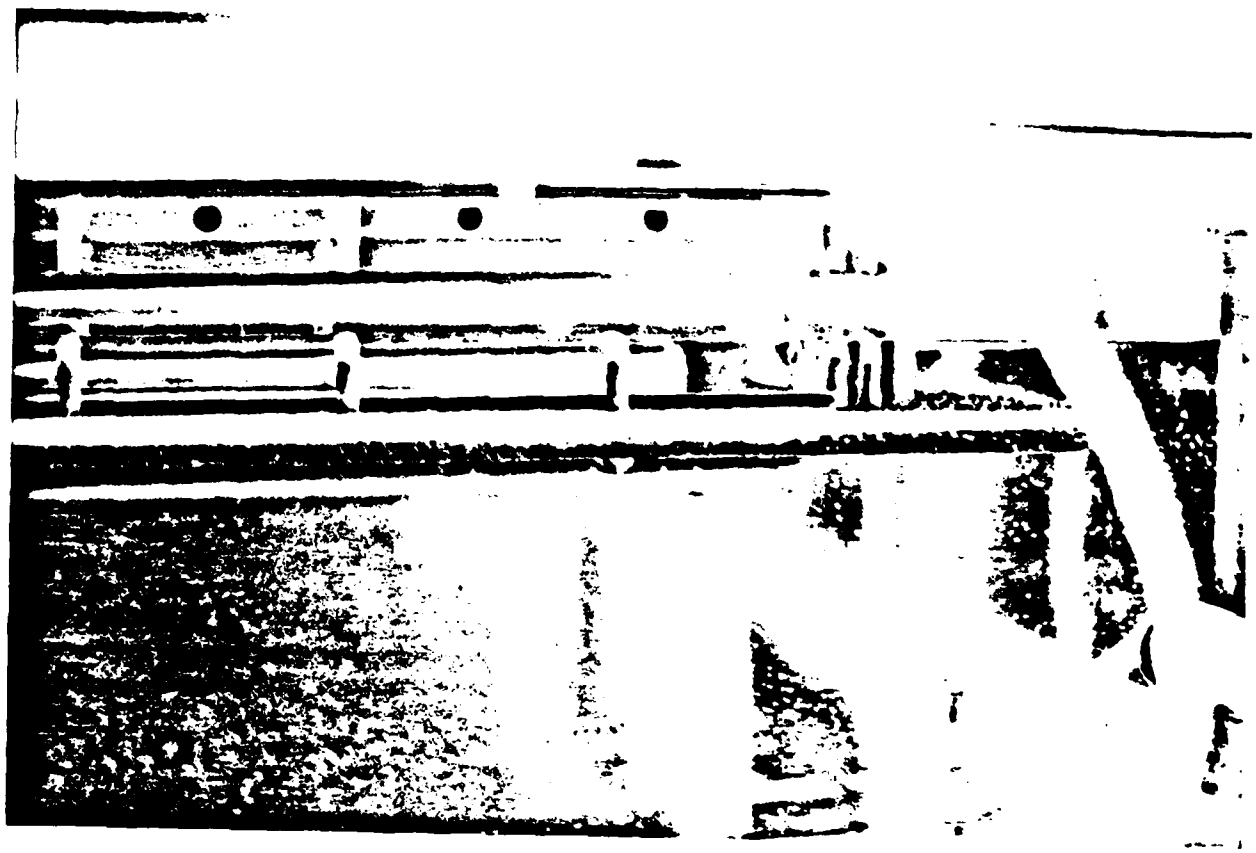

FIGURE 2.1-12 RAILGAP - CLOSE UP VIEW

FIGURE 2.1-13 MULTICHANNEL RAILGAP OPERATION

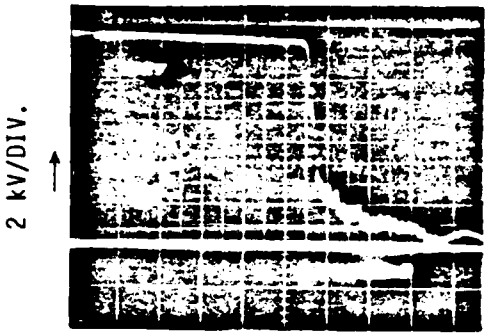

RESISTIVE FALL TIME

- MARTIN'S FORMULA

$$\tau_R = 88(\rho/\rho_o)^{\frac{1}{2}}/(NZ_oE^4)^{\frac{1}{3}}$$

$$\tau_R = 5 \text{ ns}$$

- MEASURED D VALUE 6 ns

FIGURE 2.1-14 OSCILLOSCOPE TRACE OF RAILGAP VOLTAGE

RESONATOR

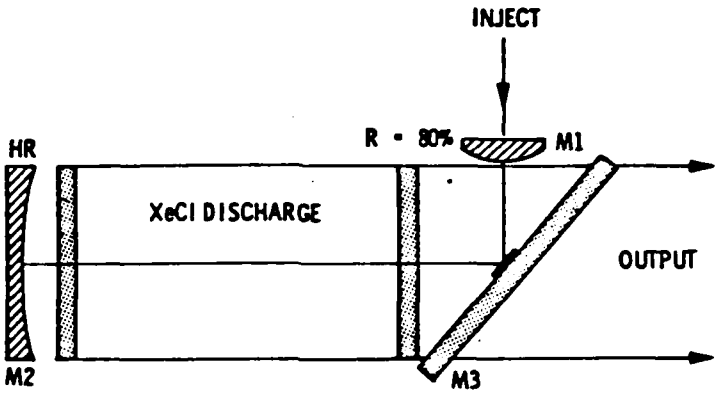

FIGURE 2.2-1 RESONATOR

(Legend: M = Mirror, HR = High Reflector)

(1) A shorter cavity is possible using standard optical mounts; (2) fewer large optical components are needed; and (3) the scraper M3 is not an internal transmissive optic and therefore produces no astigmatism in the output beam.

The use of near-normal anti-reflection coated windows rather than Brewster windows had the advantages of reducing the resonator length and of minimizing the astigmatism in the output beam. A window tilt of 3° was required to eliminate feedback.

In flat/flat resonator tests a 96% output coupling performed well. This corresponded to an unstable resonator magnification of 5 where the geometric output coupling, δ, for the lowest order mode is given by

$$\delta = 1 - \frac{1}{M^2}$$

Magnifications of 4 and 8 were then chosen for tests. Given a magnification M and cavity length L, the proper mirror curvatures are found from

$$R_1 = \frac{2L}{M-1}$$

$$R_2 = \frac{2ML}{M-1}$$

The two configurations tested were: 1) M = 4, L = 150 cm, R_1 = 100 cm, R_2 = 400 cm; 2) M = 8, L = 175 cm, R_1 = 50 cm, R_2 = 400 cm.

The injection locking of this resonator was accomplished by transmitting the injection beam through the convex resonator mirror which was partially transmissive. A nominal transmittance of 20% was chosen.

The injection laser schematic is shown in Figure 2.2-2. A Lambda-Physik XeCl laser was used in a novel oscillator/amplifier configuration. A hemispherical oscillator cavity was formed by the uncoated concave surface of the front optic and the diffraction grating which in combination with a prism beam expander and an optional etalon provided linewidth narrowing. The oscillator output was reflected by the flat surface of the front optic and returned through the gain medium at a small angle to be amplified. The diverging amplifier output was reflected clear of the laser by the scraper and then was

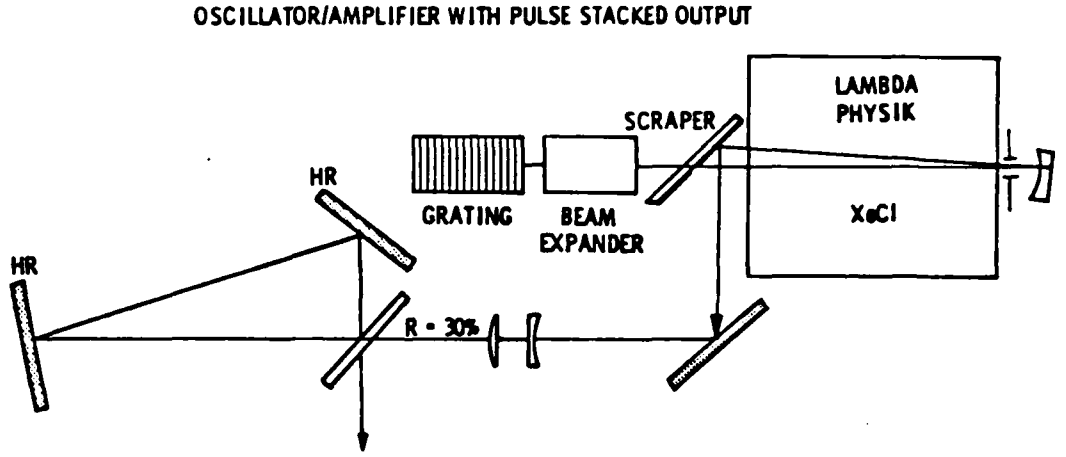

FIGURE 2.2-2 INJECTION LASER SCHEMATIC

collimated by an external telescope. A high quality 2 mJ beam with a spectral width of 1 cm^{-1} was obtained from the laser. However, the pulsewidth of 6 ns was too short to fully lock the primary laser. Therefore, a pulse-stacking technique was used to stretch the pulse width to 12 ns.

The matching of the injection laser into the primary resonator was a straightforward matter, as shown in Figure 2.2-3. The injection beam was focused at the virtual focal point of the unstable resonator concave mirror. The aperture provided isolation of the injection laser from the unstable resonator.

The energy, temporal pulseshape, and frequency spectrum of the injection-locked laser were then measured with the setup as shown in Figure 2.2-3.

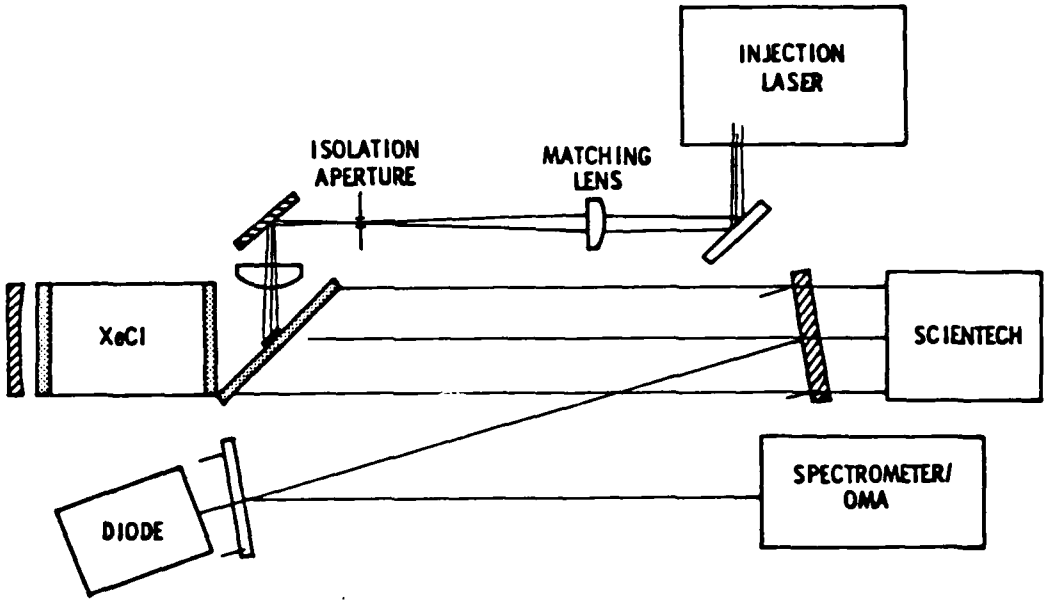

FIGURE 2.2-3 INJECTION-LOCKED SETUP

2.3 Raman Converter

Raman conversion experiments were performed with a single high energy oscillator as well as an oscillator/amplifier combination. Because of its ease of alignment (spatially and temporally), the early experiments were done with a high energy oscillator.

Figure 2.3-1 shows the Raman oscillator setup with diagnostics.

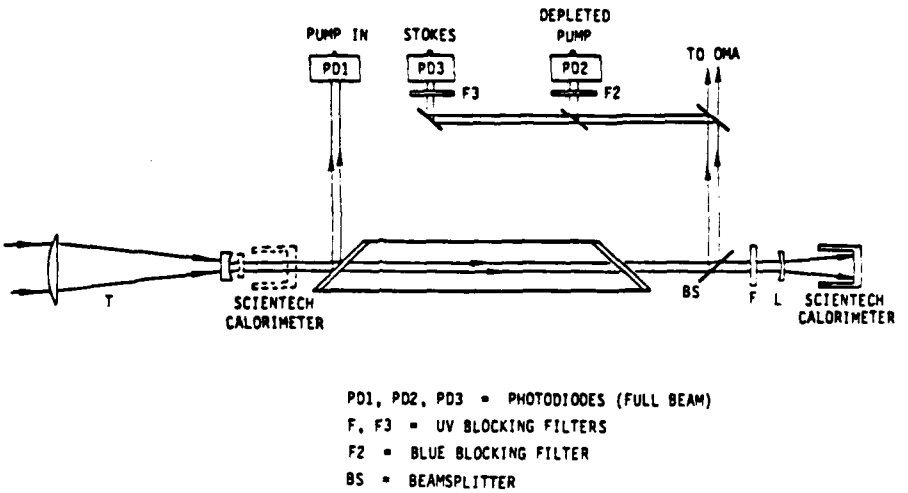

FIGURE 2.3-1 HIGH ENERGY RAMAN OSCILLATOR SETUP WITH DIAGNOSTICS

An inverse telescope, T, with a demagnification of 6.7 was used to reduce the beam area from 15 cm^2 to approximately 0.34 cm^2. The Raman cell was operated in the heat pipe mode at a temperature of 1238 C and a vapor zone length of 50 cm. A Scientech calorimeter was used to measure the energies of the UV and Stokes pulses. A diverging lens in front of the calorimeter was necessary to prevent burning its sensitive surface. The same calorimeter and lens were used for both UV and blue measurements. A beamsplitter, BS, was used to

sample the output beam for diagnostics which included time-resolved measurements of the input UV pulse, the depleted UV pulse, and the Stokes pulse. The filter, F, was used to block the UV from entering the calorimeter.

The collimated geometry of the high energy oscillator experiment incurs a penalty in reduced beam quality and unavoidable beam divergence of the Stokes radiation. This intrinsic shortcoming of the oscillator approach is overcome by using an oscillator-amplifier combination, which is shown schematically in Figure 2.3-2. A small fraction (8%) of the UV energy is split off from the main beam and focused in the oscillator cell. The operating parameters of this oscillator are selected such that a Stokes beam of high spatial quality is generated. In particular, by limiting the input energy and fosucing it relatively tightly into the cell, the Stokes beam is effectively generated by a spatially-filtered pump beam, yielding a Gaussian-type beam profile of high spatial quality. (The pump distribution near the focus is the Fourier transform of the incident distribution.) The conversion efficiency for the oscillator will be relatively low unless the UV beam is near diffraction-limited, but this is not important because most of the energy resides in the amplifier pump beam. The oscillator output and the remainder of the UV energy are directed into the amplifier cell. In this cell, which is operated at a much lower gain than the oscillator (e.g., e^{20} versus e^{90}), most of the UV energy is transferred to the high quality Stokes beam.

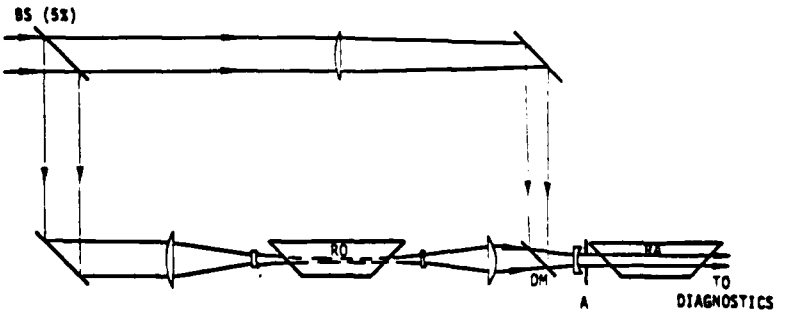

RO = RAMAN OSCILLATOR
RA = RAMAN AMPLIFIER
BS = BEAMSPLITTER
DM = DICHROIC MIRROR
A = APERTURE

FIGURE 2.3-2 RAMAN OSCILLATOR/AMPLIFIER CONFIGURATION

The Stokes injection level into the amplifier in our experiment was on the order of 10^{-3} joules, and the peak gain based on pump parameters was approximately e^{17}. However, spatial intensity variations of the pump laser make the firm assignment of a gain difficult. In addition, the temporal-matching gain enhancement technique [SLM80] was not used in this experiment due to the difficulty of its implementation on a low repetition rate device. This lack of proper timing might significantly decrease the gain for Stokes amplification.

3.0 PHASE I EXPERIMENTAL RESULTS

The results of the Phase I experiments are presented below. They are divided into four sections: (1) XeCl laser, (2) injection locking, (3) beam quality, and (4) Raman converter. Results obtained from the sidelight fluorescence measurements and the small signal gain measurements are discussed in Section 5.0.

3.1 XeCl Laser

Significant advances in the XeCl laser technology were made. A laser output of 4.4 joules at 2.1% efficiency (based on energy stored in the Blumlein PFN) has been achieved. Extensive data on gain, absorption, and sidelight fluorescence has led to a better understanding of the XeCl kinetics. Theoretical modeling of the laser is in excellent agreement with the experiments.

Best results to date have been obtained with gas mixtures using neon as the buffer gas. Using helium as the buffer gas, outputs of 2.5 J at 0.9% were obtained. Because of the poor results in helium mixtures, efforts at optimizing the laser have largely been concentrated on neon mixtures.

Table 3.1-1 lists the XeCl laser system parameters for which the best operation was obtained. All parameters marked with an asterisk are experimentally measured quantities. Stored energies are calculated from the measured voltages and capacitances. The Blumlein PFN spacing and impedance are calculated from the PFN capacitance, dimensions, and the dielectric constant of water. The output coupler is an uncoated fused silica flat (Fresnel reflection of 3.8%). The other side is AR coated at 308 nm.

The output energy was measured with a Scientech Model 36-0401 disk calorimeter. This instrument is a commercial version of a NBS design [JW70]. The total beam was incident on the calorimeter (10 cm aperture), therefore requiring no assumptions on beam uniformity or beam sampling optics. This calorimeter has a built-in resistance heater so that it may be calibrated by electrical substitution. To simulate the laser pulsed output, a capacitor was discharged through the heater resistance. If the discharge time is short

TABLE 3.1-1 SYSTEM PARAMETERS FOR OPTIMUM OPERATING CONDITIONS

Primary Energy Store			
Total Capacitance*		472 nF	
Charge Voltage*		33.7 kV	
Stored Energy		268 J	
Blumlein PFN			
	Top	Bottom	Total
Spacing	4.6 mm	4.7 mm	
Capacitance*	259 nF	254 nF	513 nF
Impedance	.22 Ω	.23 Ω	.45 Ω
Charge Voltage*	28.0 kV	28.5 kV	
Stored Energy	102 J	103 J	205 J
Water Resistivity*			1.3-1.6 MΩcm
Water Temperature*			35°C
Dielectric Constant			74.8
Laser Cavity			
Gas Mixture*			3.7 Torr HCl 57 Torr Xe 4 atm Ne
Electrode Spacing*			4 cm
Nominal Discharge Volume			4cmx4cmx90cm
Resonator			
Type			Flat-Flat
Output Coupling			96.2%
Length*			122 cm
Laser Output*			4.4 J
Pulse Width (FWHM)*			70 ns
Efficiency			
Based on Energy in PFN			2.1%
Based on Energy in Primary Capacitor			1.6%

*Experimentally Measured Parameters

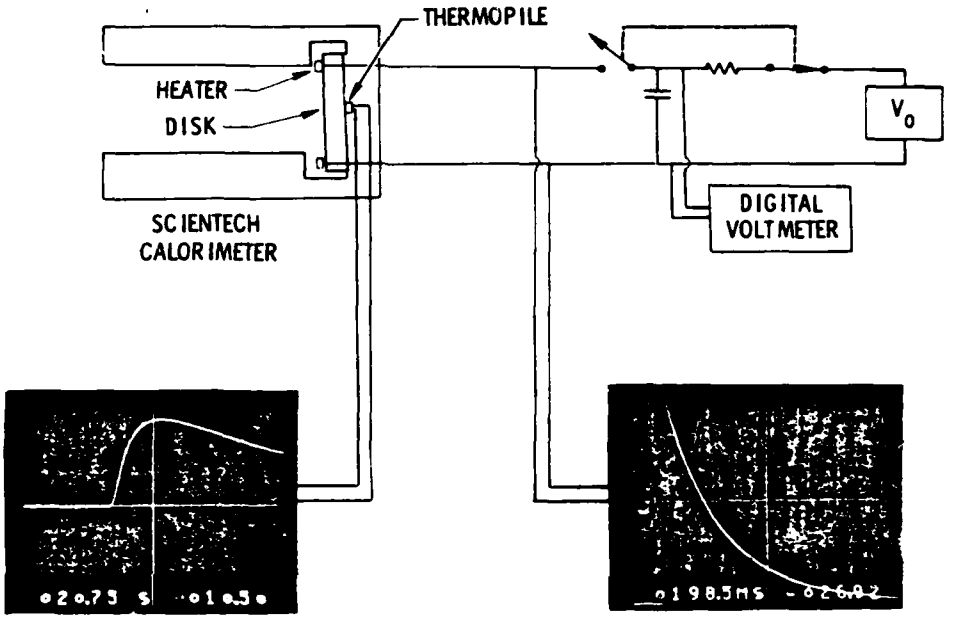

81-67

FIGURE 3.1-1 CALORIMETER CALIBRATION SETUP

compared to the calorimeter thermal time constant (22 seconds), the calorimeter output is independent of the pulse duration of the energy input, be it optical or electrical. The calibration setup is illustrated in Figure 3.1-1. The resistance heater voltages were measured with a digital oscilloscope and then integrated to obtain the energy input. According to the manufacturer's literature, the absorption of the coated disk surface is 98% from 250 nm to 35 μm. If the absorption were actually less, the actual output would be higher than measured, while if the absorption were actually 100%, the actual output would be at most 2% lower than measured.

There is a 23% loss in transferring energy from the primary energy store to the Blumlein PFN. This loss is attributed to the low resistivity of the water and to the spark gap switch. The energy loss in the water is calculated to be 8% (see Section 2.1.3) for a water resistivity of 1.5 MΩ-cm will reduce this loss to 1.3%. The rest of the loss is attributed to the spark gap switch. Replacing this switch with a thyratron would reduce this loss to negligible proportions. Thus an efficiency of energy transfer from the primary energy store to the PFN of 98% or greater should be obtainable.

Figure 3.1-2 shows the laser output and the sidelight fluorescence at 308 nm for optimum operating conditions. Both traces were taken with a vacuum planar photodiode with an S-4 cathode. The laser output pulse is 70 ns wide at full width half-maximum. The sidelight fluorescence trace shows that it takes 45 ns to achieve turn on.

Figure 3.1-3 shows voltage and current waveforms. The voltage trace was obtained by measuring the current through a 500Ω resistor which was a precision high voltage metal film resistor of low inductance design (Caddock type MG-815). The current through the resistor was measured with a Model 4100 Pearson current transformer. Since there is no electrical contact between the current transformer and the voltage being measured, this method can be used to measure voltage differences between points where neither point is ground such as in this application. The L/R time constant of the measuring circuit is about 0.5 ns. Risetime of the voltage measurement is limited by the risetime of the current transformer which is 10 ns. Current measurements are made with a linear Rogowski type probe (Physics International Model No.

4 atm Ne 1.88% Xe 0.12% HCl

V_o = 28 kV, d = 4 cm

LASER  U_ℓ = 3.9 J

50 ns/DIV.

SIDE LIGHT 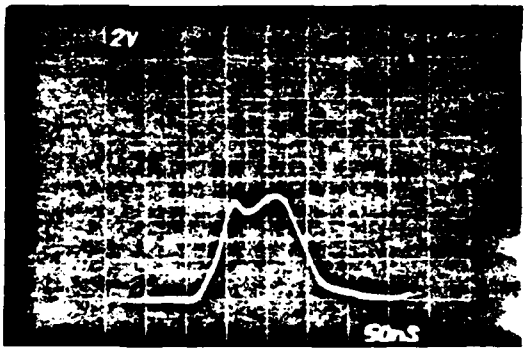

50 ns/DIV.

FIGURE 3.1-2 LASER PULSE AND SIDE LIGHT FLUORESCENCE

4 atm Ne 1.88% Xe 0.12% HCl

V_o = 28 kV, d = 4 cm

10 kV/DIV.

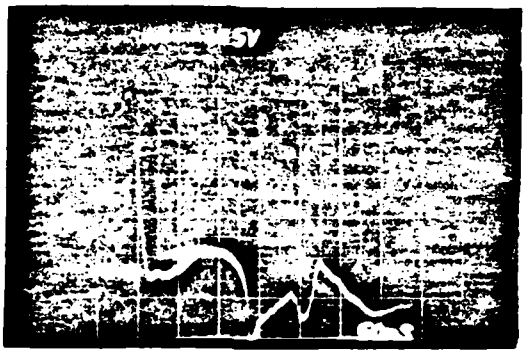

η_t = 46%

50 ns/DIV.

20 kA/DIV.

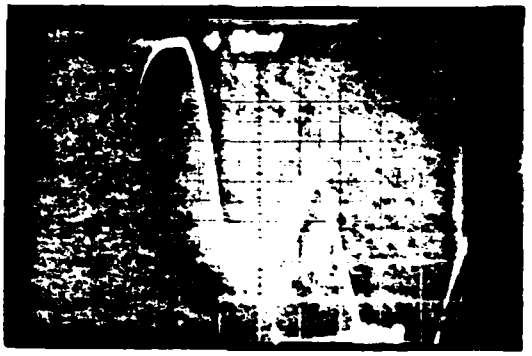

50 ns/DIV.

FIGURE 3.1-3 VOLTAGE AND CURRENT WAVEFORMS

PIM-221-0.45-10-2X). This device is well suited for current measurement in sheet type conductors and flat plate transmission lines, but requires in situ calibration. For this application, the current probe is placed next to the connecting strip between the Blumlein lower plate and the discharge electrode. Calibration is performed as follows. The voltage across the discharge is measured at the peak current when $\partial I/\partial t = 0$ and therefore there is no inductive voltage component. At this time, the equivalent circuit of the Blumlein PFN and the discharge is

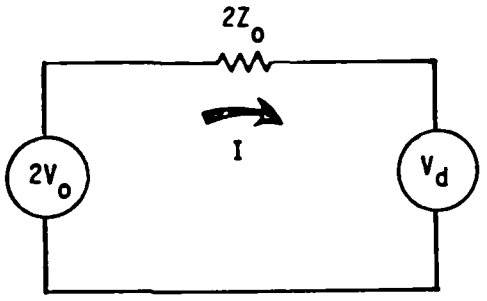

where

V_o = Blumlein PFN charge voltage per side
Z_o = Blumlein impedance per side
V_d = Discharge voltage at current peak.

The current is then simply given as

$$I = (2V_o - V_d)/2Z_o.$$

Since all quantities on the right-hand side are known, the actual value of the current at the peak can be calculated.

The rise time of the voltage pulse is about 25 ns. This risetime is determined by the voltage fall time of the rail gap switch and the inductance of the switch and its connection to the Blumlein PFN. The voltage rises to 50 kV, at which point electron avalanching breaks down the gas and current starts to be drawn. If the gas did not break down, the voltage would continue to rise to 56 kV or $2V_o$. The current risetime is determined by the PFN impedance and the inductance of the laser head and its connections to

the PFN. The voltage falls to a quasi-steady-state value, 5-10 kV, which is determined by the balance of electron production and loss processes. During this period the current rises to a quasi-steady-state value determined by the quasi-steady-state discharge voltage (V_d) Blumlein charging voltage, V_o, and the Blumlein impedance, $2Z_o$, as described previously.

This quasi-steady-state phase lasts for one round trip time of the PFN at which point the voltage and current fall to zero. The shape of the pulses after this period are due to the reflection of the various waves back and forth in the PFN. These waves would not be present if all the stored energy in the PFN were deposited in the discharge. For the present case, 46% of the stored energy was transferred to the discharge. This is determined by integrating the product of the voltage and current over time.

An optimization of the gas mixture for a neon buffer was performed at 5 atm pressure. The results are shown in Figure 3.1-4. Near the optimum mixture, the laser output is not a strong function of either the Xe or HCl concentration. It is seen that high Xe to HCl ratios from 10:1 to 20:1 are preferred. Optimum HCl concentrations are around 0.1%. A mixture optimization has not yet been performed at 4 atm. Some improvement can be expected. However, based on the results at 5 atm, the improvement probably will not be large.

A limited amount of data has been obtained on the effect of charging voltage. This is presented in Table 3.1-2. The voltage and energies are for a PFN impedance of 0.45Ω. The He mixture was 0.4% HCl, 5% Xe, and the Ne mixture was 0.12% HCl and 1.9% Xe.

TABLE 3.1-2 LASER ENERGY VS CHARGING VOLTAGE

		2 atm He		4 atm Ne	
V_o	U_o	U_ℓ	η	U_ℓ	η
32kV	262 J	2.5 J	0.9%		
28 kV	205 J	1.9 J	0.9%	4.4 J	2.1%
24 kV	151 J			2.8 J	1.8%

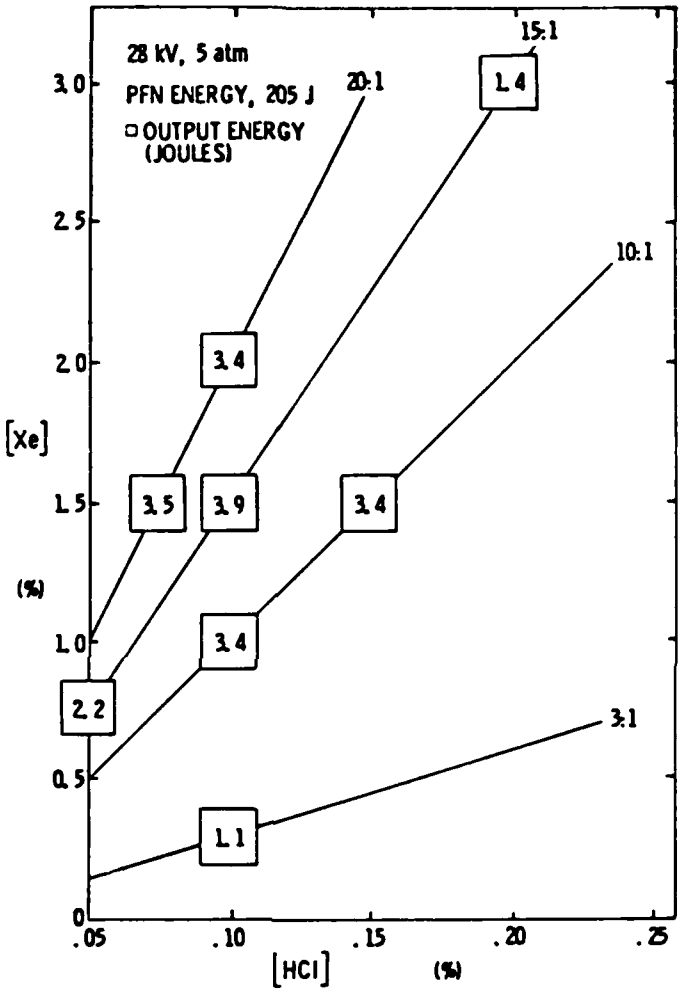

FIGURE 3.1-4 NEON MIXTURE OPTIMIZATION

3.2 Injection Locking

The injection beam had an energy of 2 mJ, a frequency bandwidth of 1 cm^{-1} (0.1A), and a pulse half-width of 12 ns. The pulse-stacked beam exhibited approximately 50% modulation and had a baseline width of 20 ns. This was satisfactory to lock the primary laser since the cavity round-trip time was 10 ns for the 150 cm, M = 4 resonator.

In tests with the M = 8 resonator, loss of locking was observed for an injection pulse energy of 0.5 mJ, which corresponds to an intensity in the unstable resonator mode volume of 1 kW/cm^2. This minimum injection energy should be even lower for the case of an M = 4 resonator due to the increased feedback.

A comparison of free-running versus injection-locked operation is shown in Figure 3.2-1. The sidelight traces show that injection eliminates the peak due to laser build-up, thereby increasing laser efficiency. The spectral traces clearly show the suppression of non-injected frequency components. The laser bandwidth measurement is resolution limited to be less than 0.6A.

3.3 Beam Quality

The beam quality of the primary laser was qualitatively studied using burn patterns and by performing Raman threshold experiments in H_2 gas.

Typical burn patterns, taken after a high quality lens, are shown in Figure 3.3-1. The beam is very uniform, although of slightly higher intensity in the lower third of the beam. This is due to the single-sided electrode connection which provides slightly more inductance for current flowing between the tops of the electrodes than at the bottom. This inceased inductance results in a hotter discharge on the bottom, and therefore higher laser output on the bottom.

A better test of optical quality was a Raman threshold experiment in H_2 gas. A comparison of the threshold powers was made between the third harmonic beam of a Nd:YAG unstable resonator and the XeCl laser. The injection-locked XeCl laser was found to have a comparable Raman threshold power to the solid-state

V_o = 28 kV, R_o = 0.45

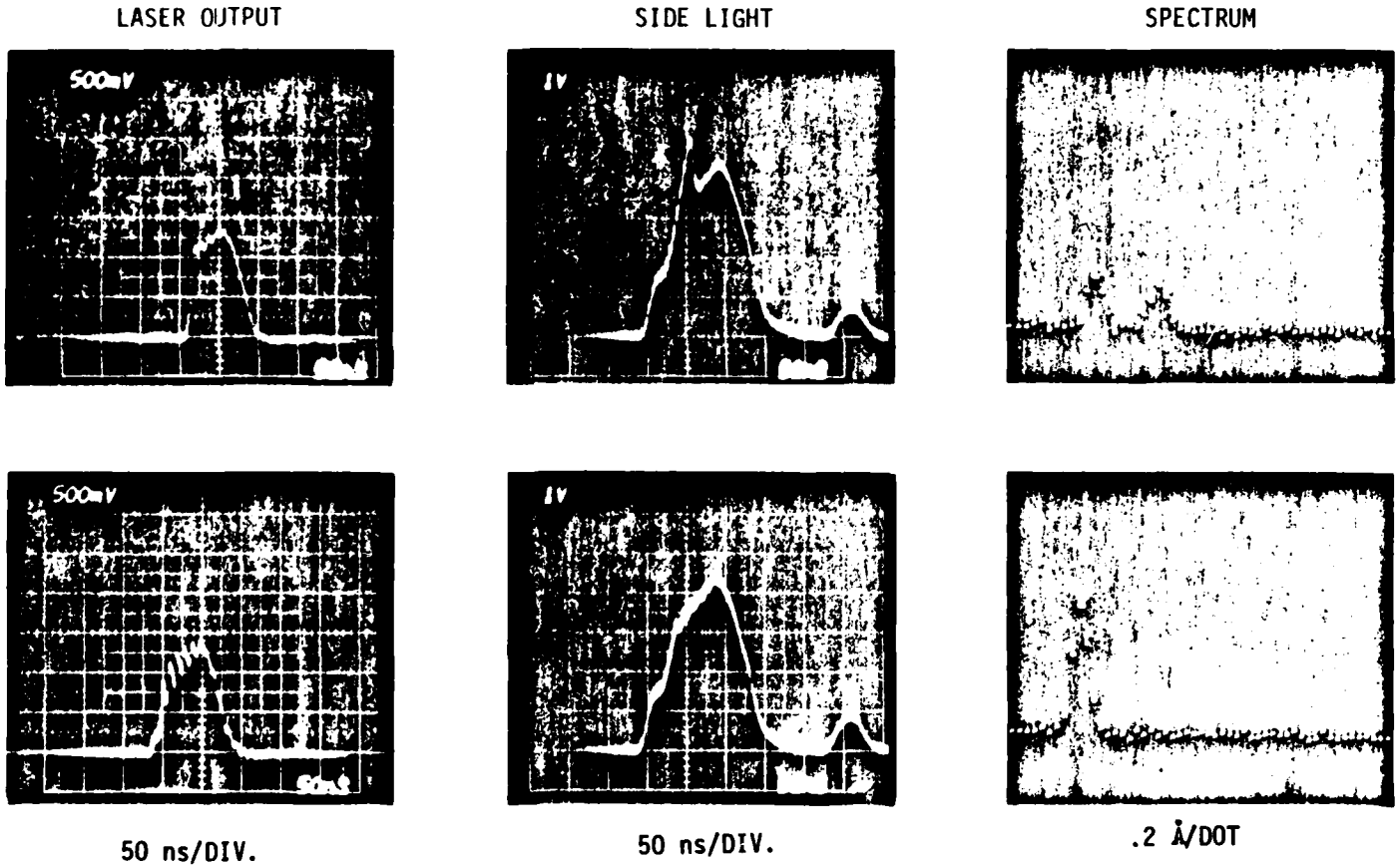

2 atm He, 2% Xe, 0.2% HCl

FIGURE 3.2-1 INJECTION LOCKING DATA

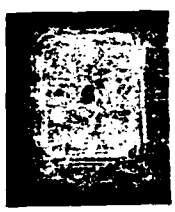

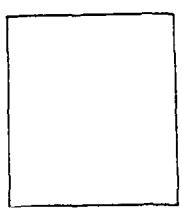

FIGURE 3.3-1 BURN PATTERNS TAKEN AFTER A HIGH QUALITY LENS

laser. The free-running XeCl laser was significantly worse. This clearly showed that the optical quality of the injection locked laser was at least as good as a solid-state laser with its consequent long buildup time and better mode definition. We estimate that the injection locked laser is less than twice diffraction limited.

3.4 Blue-Green Conversion Results

Significant advances were made in the Raman conversion experiments. Two sets of experiments were performed, one using a simple high energy Raman oscillator and the other using an oscillator/power-amplifier combination to improve the optical quality of the blue output beam. Both experiments yielded 50% Raman energy conversion, to be compared with the quantum limit of 67%. The highest blue-green output was 0.8 J at an energy conversion efficiency of 44%.

3.4.1 Raman Oscillator. Because of the ease of temporal and spatial alignment, early experiments were done with a high energy Raman oscillator pumped by the injection-locked XeCl discharge laser equipped with unstable resonator optics. Injection locking improved the optical quality of the pump laser and constrained the spectral output to only the (0,1) band of XeCl at 308.0 nm. The laser was operated off its optimum performance point because the converter optical train had been designed for an input energy of approximately 2 joules. The experimental setup for the oscillator experiments is shown in Figure 2.3-1.

Oscilloscope traces for the experiment are shown in Figure 3.4-1. Note that the Stokes pulse covers the entire pump pulse, showing that saturation of the Pb medium is not an issue at these energy levels.

The transmitted UV pulse shapes for the hot and cooled Pb cell, shown in Figure 3.4-1b clearly demonstrate excellent pump depletion, and a Raman energy conversion of 63% is deduced from the areas under the UV traces. Calorimeter measurements gave a UV input energy of 1.45 J (corrected for Fresnel losses), and a blue output energy of 0.73 J (corrected for Fresnel losses and the transmission of filter F). This corresponds to a Raman energy conversion efficiency of 50%.

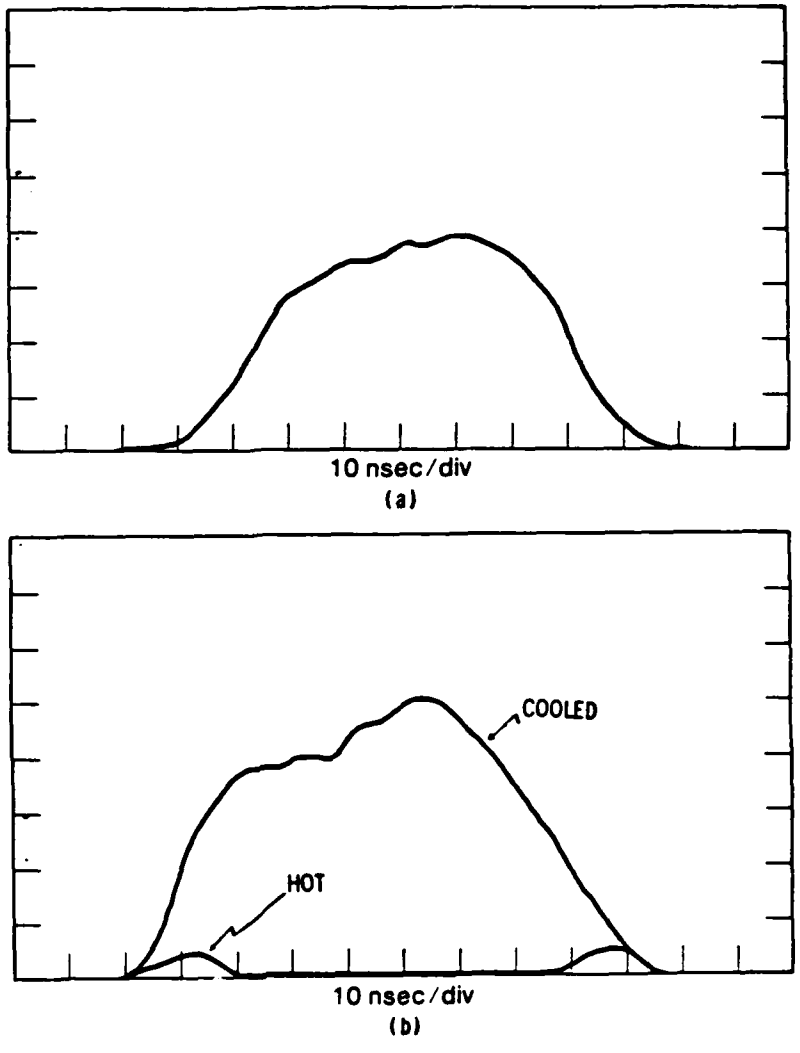

FIGURE 3.4-1 HIGH ENERGY OSCILLATOR EXPERIMENTAL PULSE SHAPES
(a) Stokes, (b) transmitted pump for hot and cooled Pb cell, superimposed. Arbitrary vertical scales.

The discrepancy between the efficiencies based on pump depletion and measured energies is due to two deficiencies in the oscillator experiment: 1) the quality of the UV pump beam; and 2) the beam divergence of a collimated geometry Raman oscillator.

The quality of the UV pump is reduced because of scatter (particulates on windows, lenses, etc.), air currents and optics imperfections, so that the main UV beam was surrounded by a relatively large low intensity background which typically contained as much as 15 to 20 percent of the total pump energy. This background radiation was not converted because of its large aperture. Most of this radiation was also not detected by the photodiode, PD2, because of its large size at the location of this diode. This condition may be rectified by using high quality optical materials in a well controlled and stable environment.

Another possible source of beam quality imperfections is that the XeCl resonator length may not have been exactly matched to the injection laser beam or to the lowest loss unstable resonator mode. The sensitivity of locking efficiency to changes in resonator length was noted recently by Bigio, et al [BS81].

The collimated geometry of the high energy oscillator experiment incurs a penalty in reduced beam quality and unavoidable beam divergence of the Stokes radiation. Since the oscillator gain was approximately three times the threshold value, a large fraction of the Stokes energy was generated in approximately one-third of the vapor zone length. The resulting large divergence of the output beam caused a reduction in the collected Stokes energy, due to aperturing by the Pb cell and by lens L (Figure 2.3-1). This effect is believed to be primarily responsible for a measured conversion efficiency lower than that deduced from pump depletion.

3.4.2 Raman Amplifier. As explained in Section 2.3, the shortcomings of the oscillator approach are overcome by using an oscillator-amplifier combination (See Figure 2.3-2). In this approach, a high quality, low energy Stokes beam is generated in the oscillator cell and then amplified in the amplifier cell. Since the amplifier is operated below threshold, its beam quality is controlled by the high quality injected beam.

Energy conversion efficiencies in the amplifier were determined using three different methods yielding close agreement. In these experiments, the weak UV background surrounding the main beam was blocked with an aperture, A. Oscilloscope traces for the input pump, output pump, and Stokes pulses are shown in Figure 3.4-2. With an input pump energy (behind the aperture) of 510 mJ, an output Stokes energy of 250 mJ was measured. This corresponds to an energy conversion efficiency of 49%. Based on the areas under the undepleted and depleted pump pulse shapes, the conversion efficiency is 48%. In addition, the efficiency can be calculated from the measured Stokes energy, E_s, and the measured total energy, E_{out}, behind the cell. The energy conversion efficiency, η_s, can be written in terms of these quantities as:

$$\eta_s = \frac{1}{E_{out}/E_s + (\omega_p/\omega_s) - 1}$$

where ω_p and ω_s are the pump and Stokes frequencies, respectively. The efficiency calculated using this expression is 52%. The close agreement of these separate measurements adds confidence to our amplifier energy conversion of 50%, corresponding to a 75% photon conversion. This value could be further improved by increasing the amplifier gain. From the depletion trace in Figure 3.4-2, we note also that Pb medium saturation was beginning to occur at the end of the pulse. An increase of Pb density in the heat pipe would eliminate this effect.

From the present work we conclude that Raman down-conversion in Pb vapor is well understood and has no significant loss mechanisms, such as dimer absorption, in the 1×10^{17} cm^{-3} density region. Also, only trace amounts of second Stokes emission were observed in optical multichannel analyzer measurements. The measured 50% conversion has been observed in both oscillator and amplifier experiments. This efficiency may be improved by proper spatial and temporal tailoring of the UV pulse toward square profiles and by improvement of the optical quality of the UV beam through the use of very high quality optical surfaces and media.

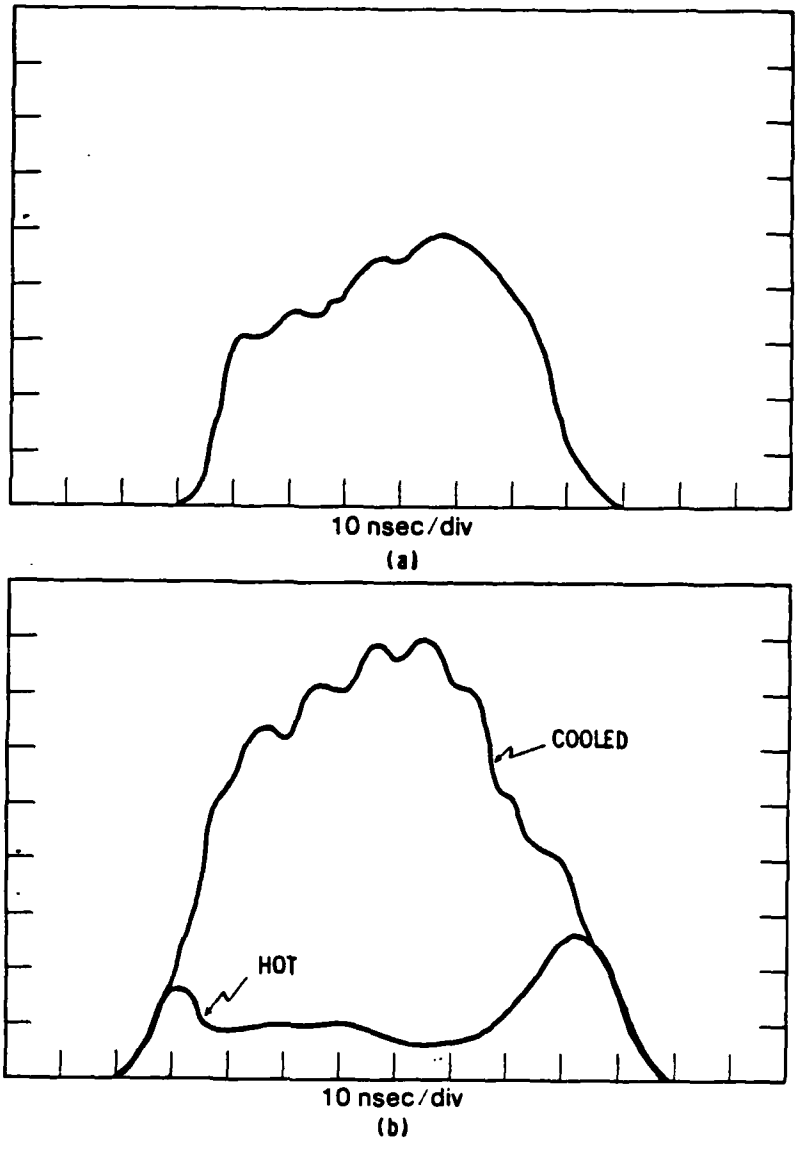

FIGURE 3.4-2 OSCILLATOR-AMPLIFIER EXPERIMENTAL PULSE SHAPES (a) Stokes, (b) transmitted pump for hot and cooled Pb cell, superimposed. Arbitrary Vertical scales.

4.0 LASER PERFORMANCE MODELING

Analysis of the XeCl laser during Phase I resulted in the development of a comprehensive computer model of the XeCl laser. This mode, called XeCl, couples an external circuit model to a comprehensive kinetics model and an optical resonator model. The influence of circuit and cavity configuration on laser efficiency can be examined in a self-consistent manner.

The details of the code, along with baseline results and parametric analysis, will be presented below.

4.1 External Circuit and Preionization

Charging Cycle. Charging of the Blumlein is achieved by resonant transfer from a matched capacitor through a spark gap or thyratron switch as shown in Figure 4.1-1. The inductor is selected to achieve the desired charging time.

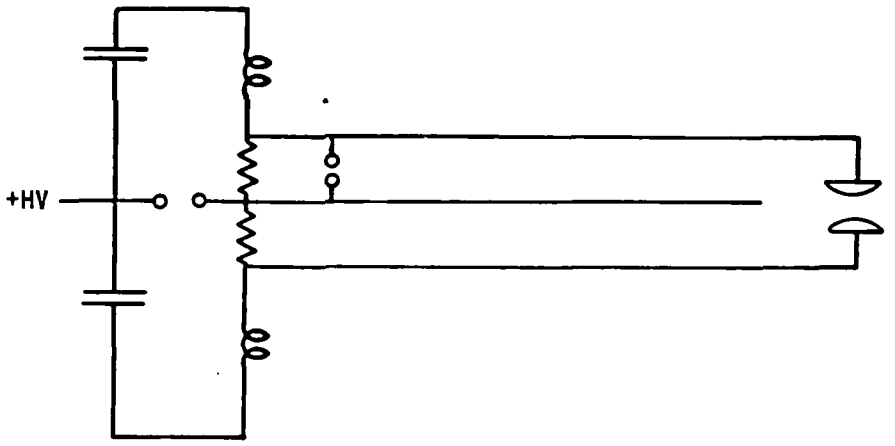

FIGURE 4.1-1 BLUMLEIN CHARGING SCHEMATIC

The two sides of the Blumlein are charged in parallel to minimize prevoltage across the discharge. Any voltage present on the electrodes before breakdown will cause electrons to drift away from the cathode, reducing the preionization density in that region. This effect is minimized by reducing the prevoltage and by maintaining a strong preionization source right up to breakdown. The thickness of the cathode depletion zone in the presence of preionization is

$$\ell_d = \frac{\mu_e}{\beta} E$$

where μ_e is the electron mobility, E is the electric field, and β is the attachment rate. In a typical laser mixture with a 2% prevoltage, the depletion zone is about 0.01 cm thick. The average distance between electrons at 10^6 cm^{-3} is also 0.01 cm, which is adequate for the development of a uniform glow [Pa74]. However, larger prevoltage may lead to arcing.

The charging of each side of the Blumlein was modeled as shown in Figure 4.1-2. The voltage waveforms were assumed to propagate without dispersion in the line.

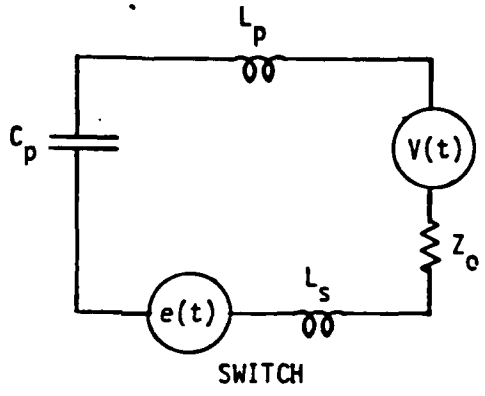

$$V(t) = V(t - \tau_p)$$

FIGURE 4.1-2 MODEL FOR CHARGING A DISTRIBUTED LINE

Voltage on the line rises in steps as indicated in Figure 4.1-3. The peak voltage is slightly less than the primary voltage due to inductive energy present in the line. This effect is only a few percent for charging times, T_{ch}, which are more than ten times the electrical length of the line. The resistive loss in the dielectric is much more significant.

The dielectric loss can easily be calculated for $T_{ch} \gg \tau_p$ (Blumlein transit time) by replacing the distributed line with a capacitor and shunt resistor.

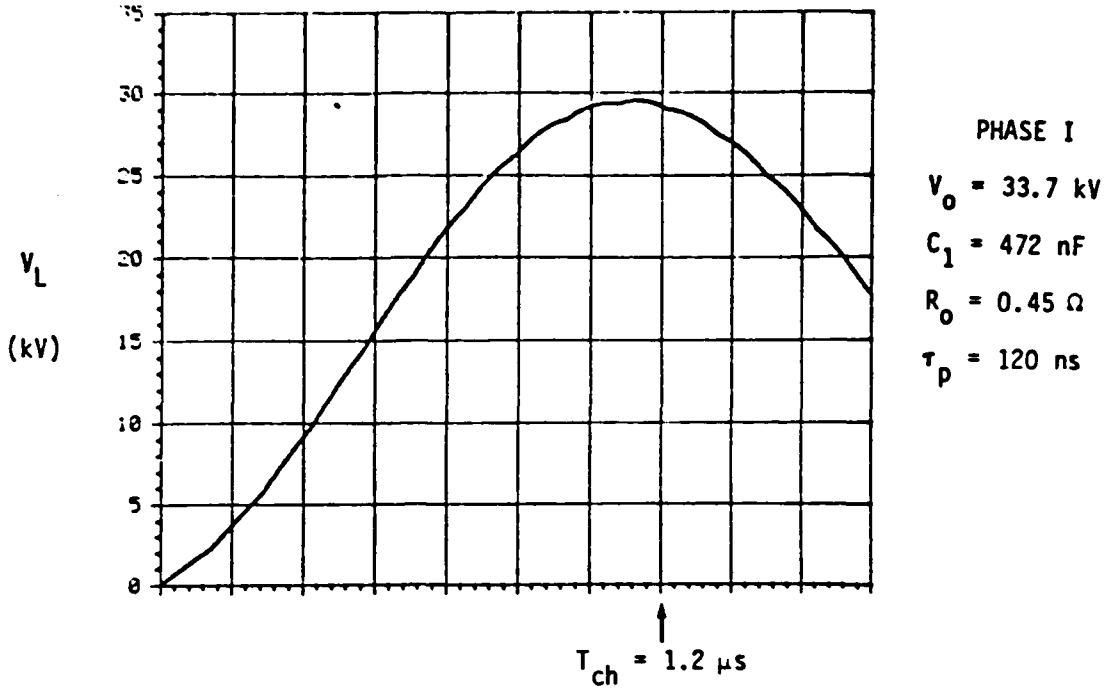

FIGURE 4.1-3 CHARGING VOLTAGE ON A DISTRIBUTED LINE

Then, for $T_{ch} \gg T_{st}$, the fraction of stored energy lost in the dielectric during the first cycle is $0.75\ T_{ch}/T_{st}$, where T_{st} is the RC time constant, which for water at 10 MΩ-cm is 70 μs. The fractional energy loss in the switch is given approximately by τ_R/T_{ch} where τ_R is the resistive time. In the laser model the switch is characterized by a voltage source and a series inductor. The voltage during the resistive phase is given by [CFM79]

$$e(t) = V_o\ (2 - 3^{t/\tau_i}) \qquad t < \tau_i\ \ln 2$$

$$= 0 \qquad t > \tau_i\ \ln 2$$

where V_o is the charging voltage and $\tau_R \approx \tau_i/n2$.

The steady-state voltage drop is on the order of 100 V and is neglected.

Preionization. Preionization of the discharge is achieved by uniform illumination with X-rays of 50 to 75 KeV. This produces a source density, S, of electrons and ions in the volume which depends on the X-ray flux and the stopping cross sections of the gas, integrated over the X-ray spectrum.

Assuming a source density which is constant in time, the electron density is given by

$$n_e = \frac{S}{\beta}(1-e^{-\beta t})$$

where β is the attachment rate. To maximize the electron density for a given X-ray dose, the preionization pulse length, T_p, should be as short as possible. Long pulses result in the production of a majority of negative ions which are less effective in producing avalanches after the field is applied.

It has been postulated [Hs76] that negative ions may lead to avalanching through electron detachment in heavy particle collisions. The primary negative ion formed by electrons at 1 eV is $C\ell^-$ with a binding energy of 3.7 eV. The probability of $C\ell^-$ losing its electron in a neutral collision is negligible. The formation of HCl^- in three-body collisions with slow electrons is also possible. The inverse of this latter reaction would result in an equilibrium population of thermal electrons available for acceleration once the field is applied.

Presently, the electron density is assumed to be uniform with an initial value determined by experiment. With $\beta T_p = 1$, the initial negative ion density is about one half the electron density.

Discharge Cycle. In the XeCl model, the circuit equations are coupled directly with the kinetics and optical cavity equations. The Blumlein line and rail gap switch models are discussed below.

- Blumlein Line

The Blumlein line model is shown schematically in Figure 4.1-4. The two delay lines are connected in series across the load which consists of the discharge itself and a series inductor, L_d. The multi-channel switch is represented by the voltage source, e(t), and inductor, L_s. The voltage waveforms traveling in each line are reflected at line termination according to the formula

$$V_{reflected} = V_{incident} - Z_o I$$

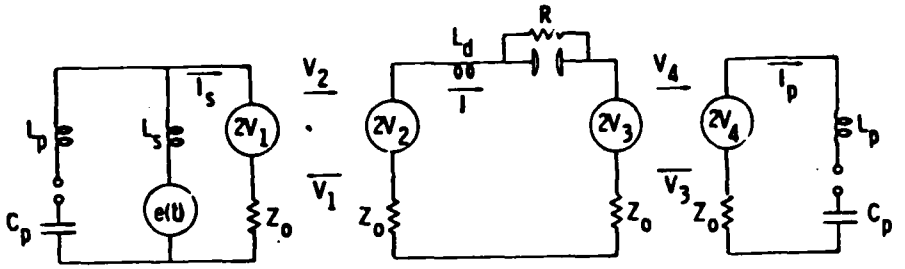

FIGURE 4.1-4 BLUMLEIN MODEL SCHEMATIC

$$V_{REFLECTED} = V_{INCIDENT} - Z_o I$$

$$\text{TRANSIT TIME} = \frac{\tau_D}{2}$$

where Z_o is the characteristic impedance of the line and I is the current flowing in the terminating circuit. The discrete elements are treated with differential equations for each current loop as in standard circuit analysis. The voltage across a constant impedance load with $L_s = L_d = 1nH$ is shown in Figure 4.1-5. Note the characteristic inging when operating into an unmatched load. The same voltages with $L_s = 5nH$ and $L_d = 9nH$ are shown in Figure 4.1-6. The fraction of stored energy transferred to the load is indicated next to each plot. Finally, the voltage into an open circuit and the voltage across the switch are shown in Figure 4.1-7. Only one-fourth of the switch inductance is included in the measurement so as to accurately reflect the experimental conditions.

The major losses in the discharging cycle are the switch loss and the skin effect losses. The switch losses will be treated in the next section. The skin effect losses can be estimated, if they are small, by a Fourier analysis of the current waveform at each point in the line. The power loss for each component is given by

$$\frac{1}{2}\sqrt{\frac{\omega\mu}{2\sigma}}\,\frac{dx}{w}\,\left|\,I_\omega\,\right|^2$$

where ω is the angular frequency, μ is the permeability of the plates, σ is the conductivity of the plates, and w is the width of the line. The total power loss is found by integrating this expression over the Fourier spectrum

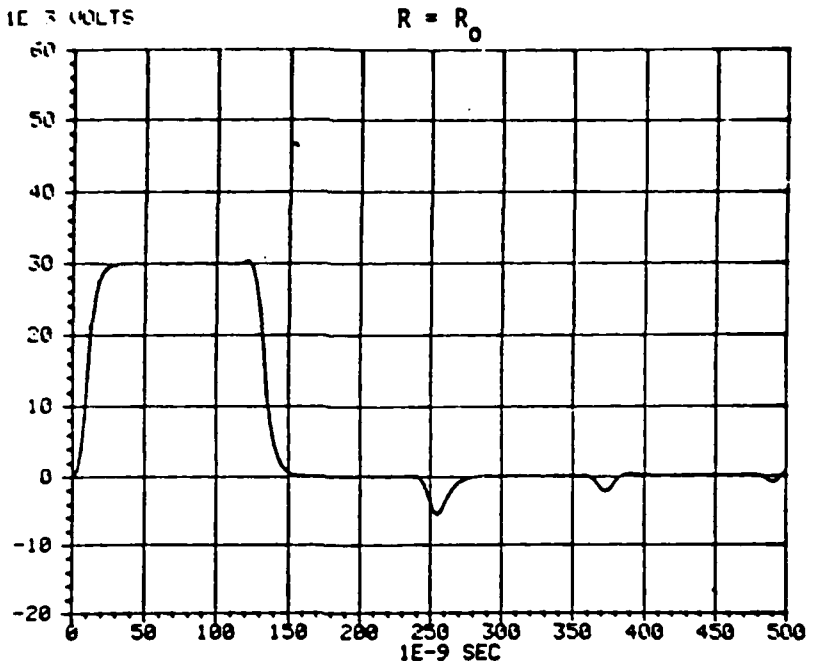

η_t = 98%

V_o = 30 kV

L_s = 1 nH

L_d = 1 nH

R_o = 0.5 Ω

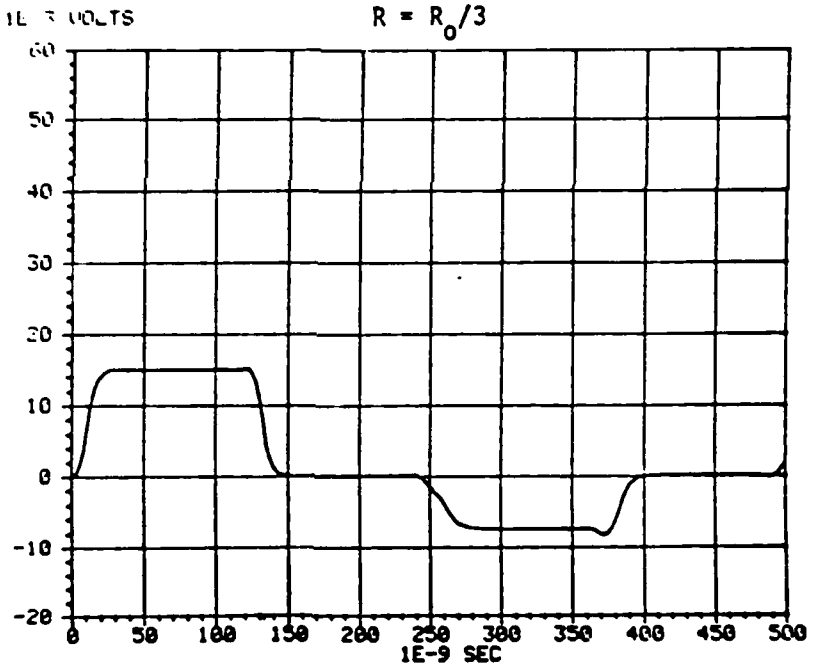

η_t = 73%

FIGURE 4.1-5 BLUMLEIN WITH CONSTANT LOAD

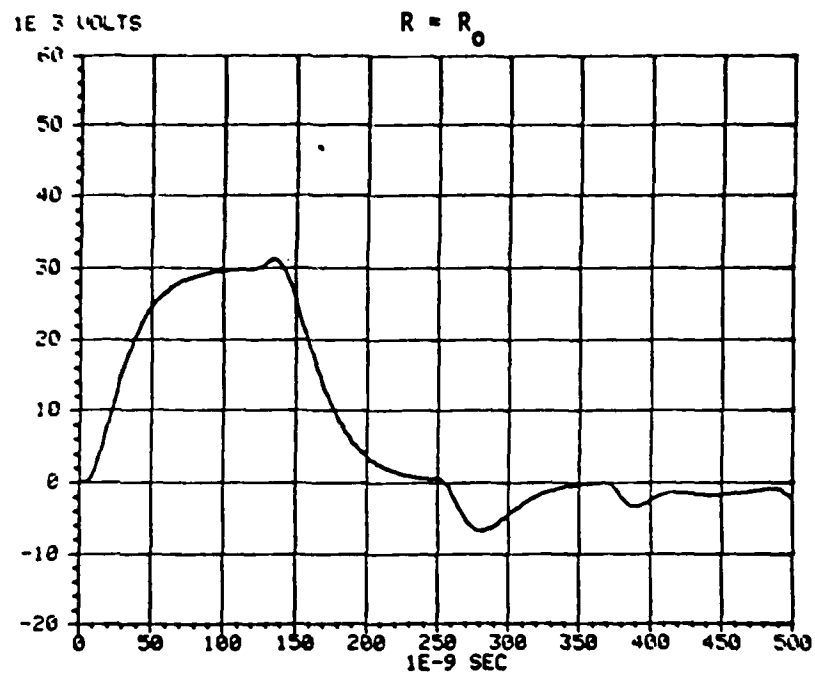

η_t = 97%

V_o = 30 kV

L_s = 5 nH

L_d = 9 nH

R_o = 0.5 Ω

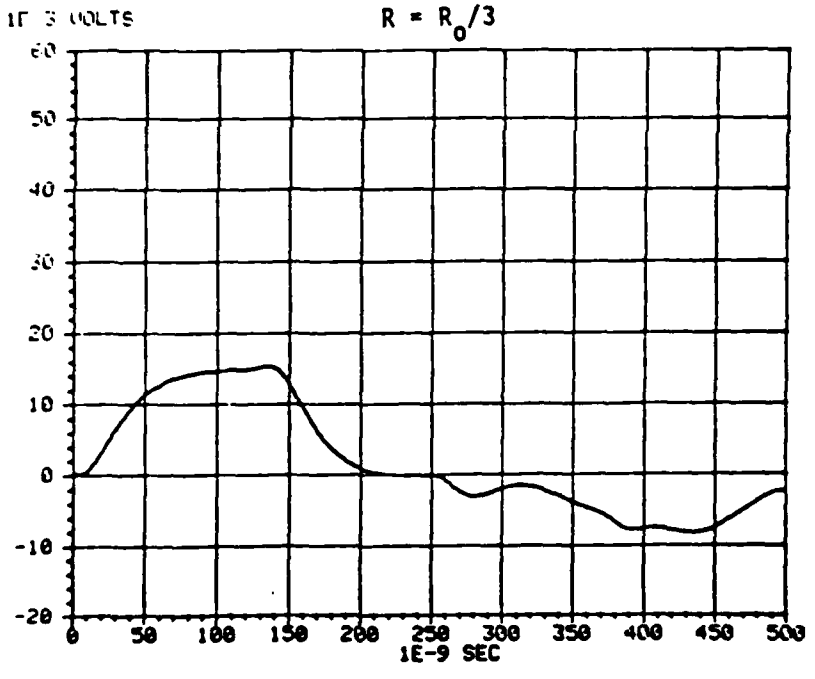

η_t = 68%

FIGURE 4.1-6 BLUMLEIN VOLTAGES WITH INDUCTANCE

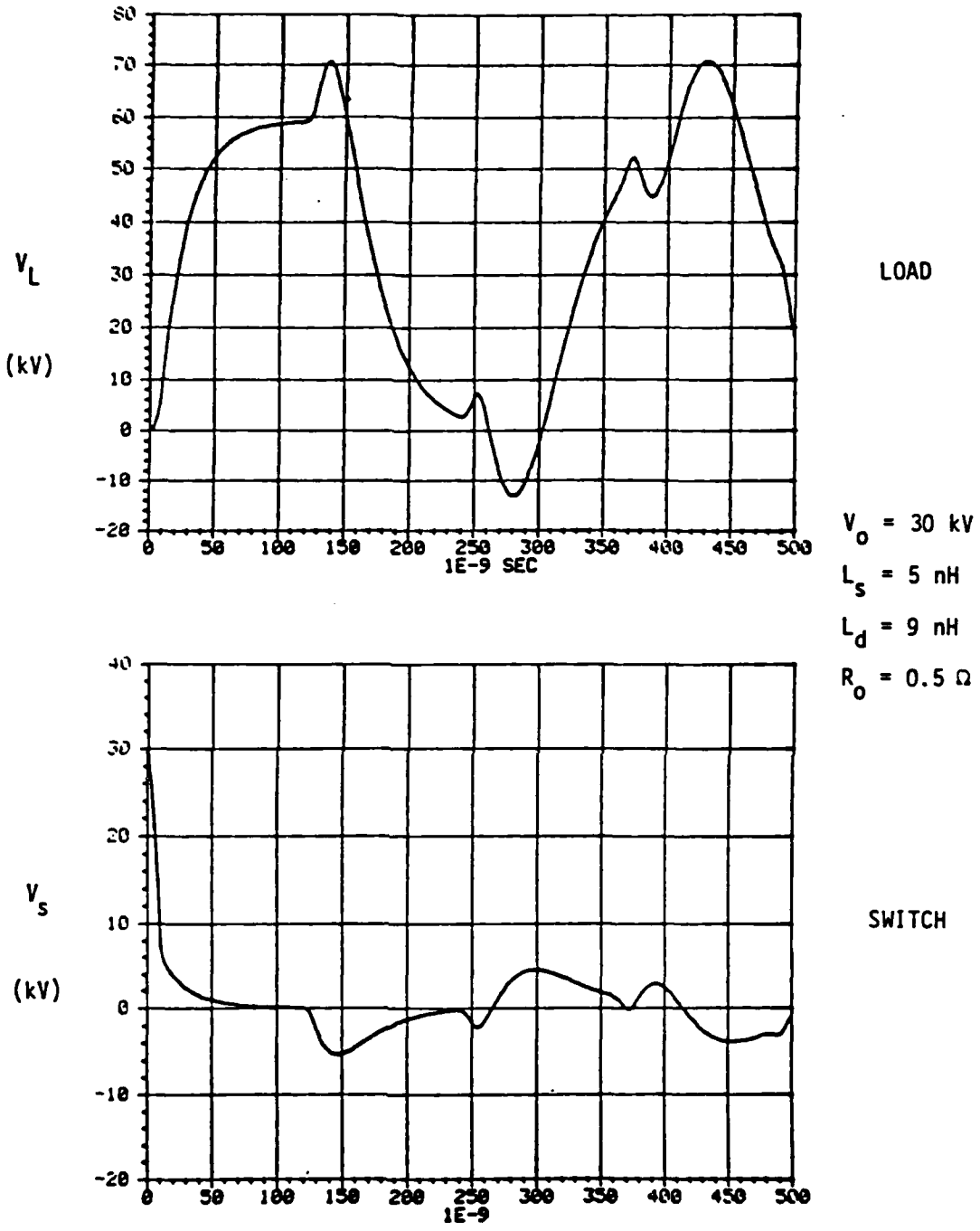

FIGURE 4.1-7 OPEN LOAD AND SWITCH VOLTAGES: BLUMLEIN

at each point in the line and then integrating over the length of the line. The fractional loss for a Blumlein switched onto a matched load is

$$\frac{\Delta U}{U} \text{ (Blumlein)} = 4.2\sqrt{\frac{\mu\tau_p}{\sigma\epsilon}}\ \frac{c}{w R_o}$$

where e is the dielectric constant and R_o is the load impedance.

- Multi-Channel Switch

The multi-channel switch is treated in the model as a time-dependent voltage source in series with an inductor, just as with the charging switch or thyratron. The length of the resistive phase is given by the empirical formula [Ma70]

$$\tau_R = \tau_i \ln 2 = \frac{88}{(nZ_o E^4)^{\frac{1}{3}}} \left(\frac{\rho}{\rho_o}\right)^{\frac{1}{2}} \text{(ns)}$$

where n is the number of arc channels, Z_o (in Ω) is the characteristic impedance of the line, E (in 10kV.cm) is the average field at breakdown, and ρ/ρ_o is the gas density normalized to standard density. For the Phase I switch, τ_i = 7 ns.

The resistive switch loss is found by integrating the product of current and voltage over the resistive time period. The fraction of stored energy lost in the switch is thus

$$\frac{\Delta u}{u} \text{ (Switch Loss)} = 0.56\,\tau_R/\tau_p\ .$$

For the Phase I device, this fractional loss was 2.3%. The inductive time constant is

$$\tau_L = L_s/Z_o\ .$$

The switch inductance was found experimentally to be 3nH, which makes τ_L = 13 ns and gives a 10-90% voltage risetime of about 30 ns across the discharge.

4.2 Electron and Ion Kinetics

Boltzmann Analysis and Cross Sections. The electron energy distribution is calculated using a steady-state Boltzmann code with the latest available cross section data. The code includes stepwise excitation, superelastic collisions and electron-electron collisions. Ionization and attachment are treated as an electron source and loss, respectively. The code provides rate constants as functions of E/N for use in the kinetics model. The excited state populations are fed back from the kinetics model into the Boltzmann code to provide self-consistency.

The momentum transfer cross sections for He, Ne, and Ar are shown in Figure 4.2-1. The small scattering cross section in neon is the principal reason for the greater formation efficiency in this buffer gas. Some of the inelastic cross sections used in the code are shown in Figure 4.2-2. Most of the cross sections are known with some degree of confidence. One exception is the dissociation of HCl. This process has a threshold of about 5.45V and a peak of 8V. It is assumed to possess the same resonant character as the

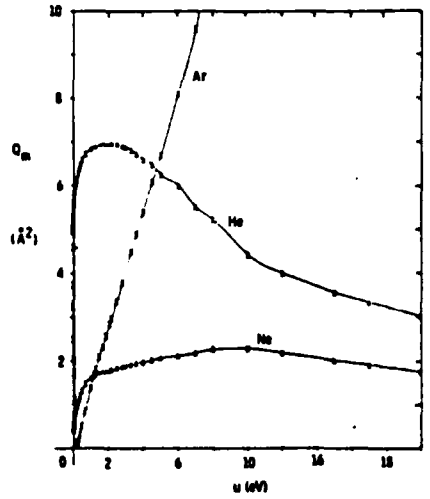

FIGURE 4.2-1 MOMENTUM TRANSFER CROSS SECTIONS

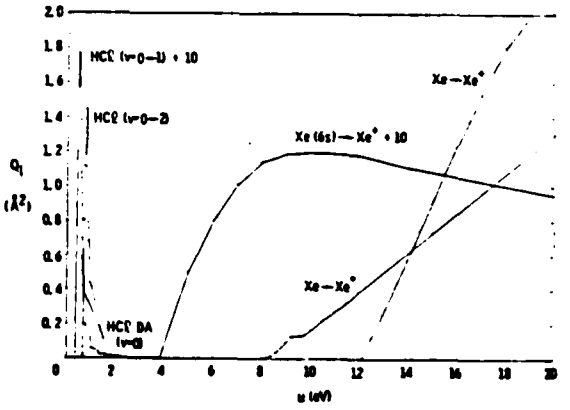

FIGURE 4.2-2 INELASTIC CROSS SECTIONS

underlying H^- formation channel. The dissociation into neutral products is taken to have a peak cross section of 2 $\AA^2$. This process has a significant impact on the formation efficiency in the XeCl laser.

The rate constants for Xe electronic excitation and ionization and for HCl vibrational excitation and dissociative attachment are shown in Figures 4.2-3 and 4.2-4 for He and Ne buffers respectively. The intersection of the ionization and attachment curves coincides with the static breakdown E/N since these are the only two processes occurring at low current densities. The intersection of the Xe electronic excitation and HCl vibrational excitation curves gives an upper limit to the steady-state E/N at high current density since these are the rate limiting processes for stepwise ionization of Xe and dissociative attachment from vibrationally excited HCl.

The fraction of electrical input power distributed into the various excitation channels is shown in Figures 4.2-5 and 4.2-6 for He and Ne buffers respectively. Notice that the pumping efficiency into Xe* at the steady-state E/N is about a factor of three higher in Ne over that in He. In the Ne mixture at 2.5 Td, the total pumping into Xe*, Xe**, and Xe^+ is 45%; and since the quantum efficiency of the ion channel is 33%, the maximum formation efficiency is 15% at this E/N. However, if the steady-state E/N could be pushed to its maximum value of 3.5 Td at high current density, then the formation efficiency would be 22%. This is higher than the value for e-beam pumping of 17% [FCP 80]. These numbers are of course only projections and may never be achieved in practice due to competing processes, but they do indicate that the intrinsic laser efficiency under discharge pumping has the potential for reaching a value of 6%. An intrinsic efficiency greater than 4% was achieved in the Phase I device.

Dissociative Attachment. The rate constants for dissociative attachment to HCl (v = 1) and HCl (v = 2) are taken as constant factors times the HCl (v = 0) rate. These factors were measured experimentally to be 38 and 880, respectively [AW81]. In addition to the vibrational enhancement, there was observed a comparable rotational enhancement. This has also been included in the model. The cross sections used for vibrational excitation are those of Rohr and Linder [RL76] for v = 0→ 1 and 0→ 2 . The cross sections for 1→ 2 and 2→ 3

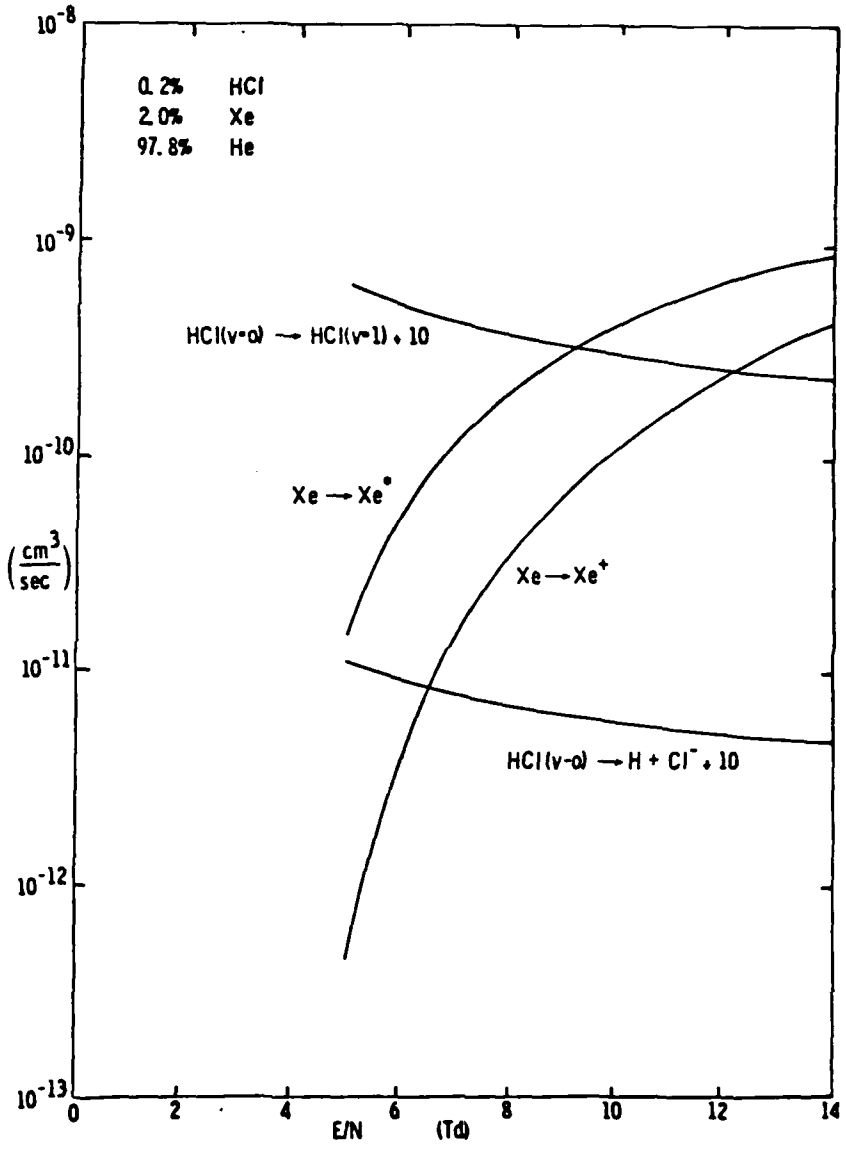

FIGURE 4.2-3 RATE CONSTANTS VS E/N FOR He MIXTURE

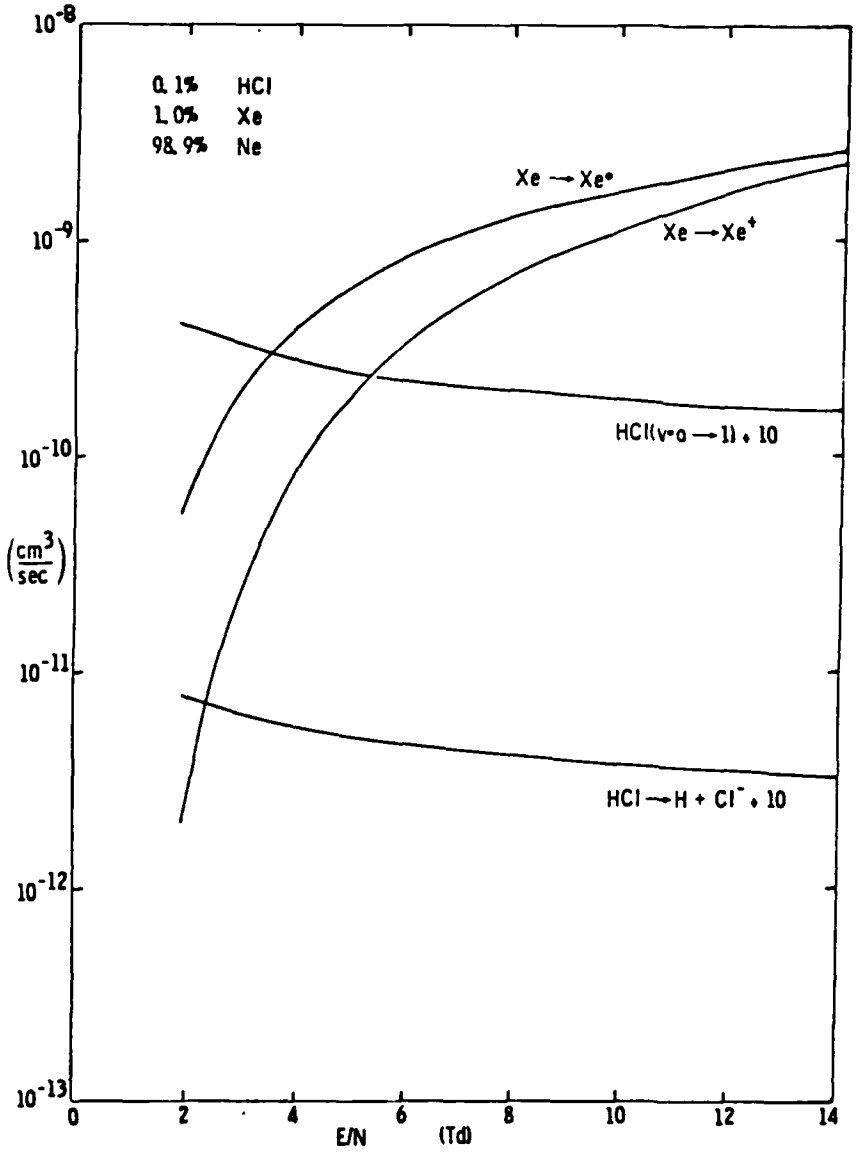

FIGURE 4.2-4 RATE CONSTANT VS E/N FOR Ne MIXTURE

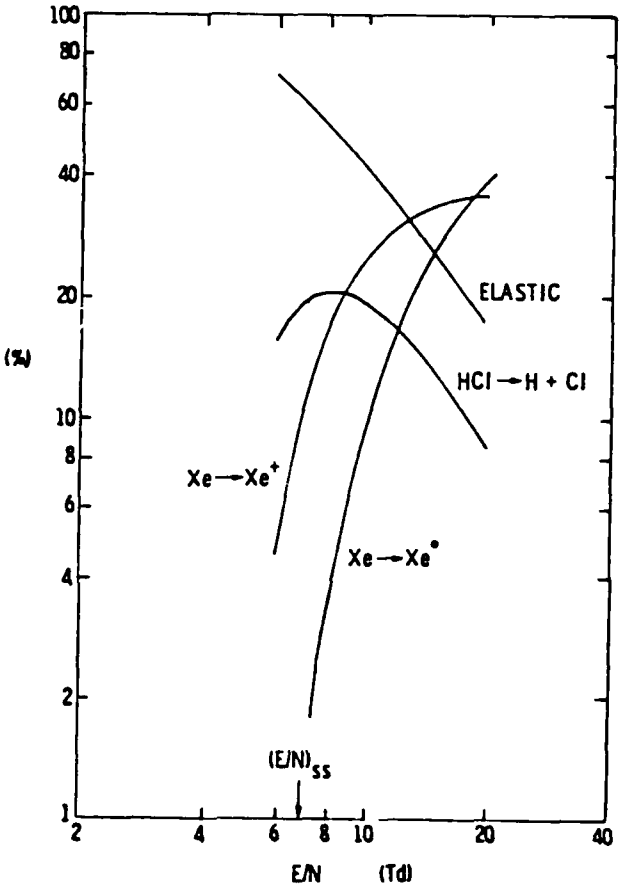

FIGURE 4.2-5 POWER DISTRIBUTION VS E/N
(0.2% HCl, 2% Xe, 97.8% He)

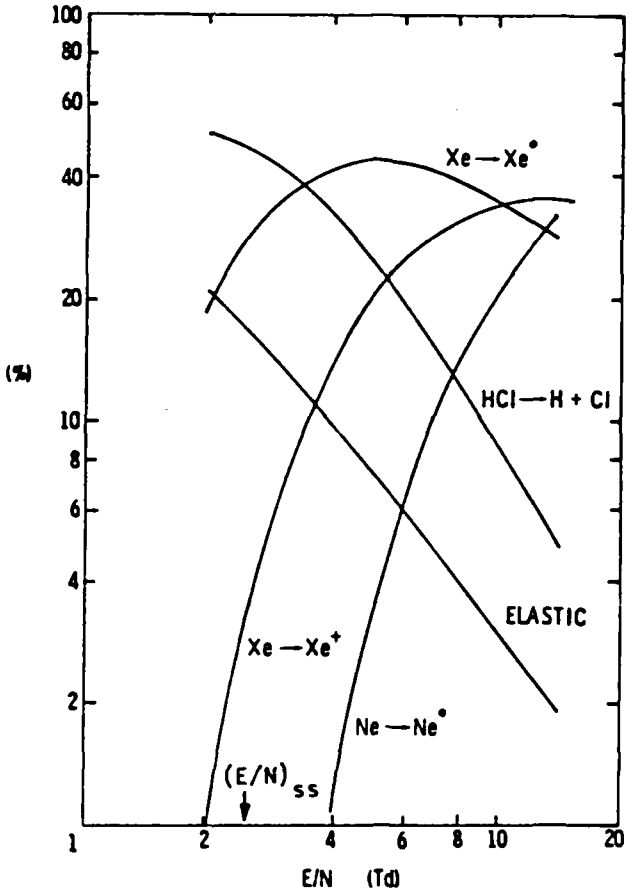

FIGURE 4.2-6 POWER DISTRIBUTION VS E/N
(0.1% HCl, 1% Xe, 98.9% Ne)

were assumed to have the same shape and magnitude as the $0 \rightarrow 1$ cross sections with appropriately shifted thresholds. A similar assumption was made for $1 \rightarrow 3$. The dissociative attachment cross section for v = 0 was taken from Azria et al [ARP74]. It was found from the model that most of the attachment occurs with HCl (v = 2) which is formed by successive excitation via $0 \rightarrow 1$ and $1 \rightarrow 2$. The total effective attachment rate is typically 2×10^{-9} cm^3/s at the peak.

The rotational excitation cross sections in HCl are very large due to the permanent dipole moment of 1.11 Debye. A total cross section of 7×10^{-15} cm^2 was measured in HBr at 5eV, [Ro78] and a value of 4×10^{-15} cm^2 is inferred in HCl at the same energy. The rate constant at this energy is thus 5×10^{-7} cm^3/s and with an electron density of 2×10^{15} cm^{-3}, the rotational excitation rate by electrons is 10^9 s^{-1}. The gas kinetic rate is assumed for rotational relaxation in collisions with the buffer gas. The model predicts final rotational temperatures for HCl of about 1400°K.

Ion Recombination. The principal ion loss mechanisms in the XeCl discharge are ion-ion recombination and electron-ion dissociative recombination. The effective two-body rate constant for the three-body stabilized ion-ion reaction is a function of neutral density [F178] [WB78], gas temperature [BW80], and ion density [MWB80]. The ion-ion rate at 4 atm and 300°K is 2×10^{-6} cm^3 s for Xe^+ and Cl^-. At 400°K, the rate drops by a factor of two. With an ion density of 10^{15} cm^{-3}, the rate drops another factor of three due to plasma screening effects which reduce the interaction potential. The end result of a lower ion-ion recombination rate is a higher Cl^- concentration, which increases absorption at the laser wavelength.

The dissociative recombination rate is principally a function of the electron temperature [SBS77]. For a characteristic electron energy of 3.4 eV the rate constant is 1.4×10^{-7} cm^3/s. Ion-ion and dissociative recombination are about equally effective in neutralizing Xe_2^+.

4.3 Excited State Kinetics

Stepwise Ionization and Superelastic Collisions in Xe. A term diagram for Xenon is shown in Figure 1.2.6-22. The levels are grouped into five categories: Xe, Xe*, Xe**, Xe***, and Xe^+. These composite states are internally mixed by electron collisions. Cross sections for stepwise excitation and ionization from these states are calculated using Gryzinski's classical formulation averaged over individual levels [LD78]. Superelastic cross sections are calculated in the usual manner using the principle of detailed balance.

Penning Ionization by Ne*. During the high voltage breakdown phase, a large fraction of the electrical power goes into electronic excitation of neon. Very little direct neon ionization occurs. The Ne* formed during this phase goes on to ionize Xe and HCl through Penning collisions. The rate constants or this process are 7.4×10^{-11} cm^3/s and 1.7×10^{-10} cm^3/s, respectively. Since there is typically 10 to 15 times as much Xe as HCl, the predominant channel is to form Xe^+. This process contributes only a small fraction to the total discharge pumping but it can affect the shape of the voltage waveform at breakdown.

Quenching of Xe* and Xe** by HCl (v = 0, 1, 2). The quenching of Xe(6s, $^3P_{1,2}$) by HCl (v = 0) has a rate constant of 5.6×10^{-10} cm^3/s [KVS79]. The formation of XeCl(B) in this reaction is negligible. However the reaction of doubly excited Xe** with HCl has been observed to result in XeCl(B) fluorescence [Se80]. The rate constant for this reaction was derived using the "harpoon" model [He66] to be 1.6×10^{-9} cm^3/s which is essentially gas kinetic. The branching ratio into XeCl(B) was predicted by Setzer to be greater than 50%.

The reaction of Xe(6s, $^3P_2$) with HCl (v = 1) to form XeCl(B) was recently measured to proceed with a rate constant of 2×10^{-10} cm^3/s [Ch81]. If the total quenching rate for v = 1 is the same as for v = 0, then the branching ratio is 36%. In the laser discharge, HCl (v = 1) reaches equilibrium at about 30% of the total HCl concentration, and this process plays a significant role in the neutral channel pumping of XeCl.

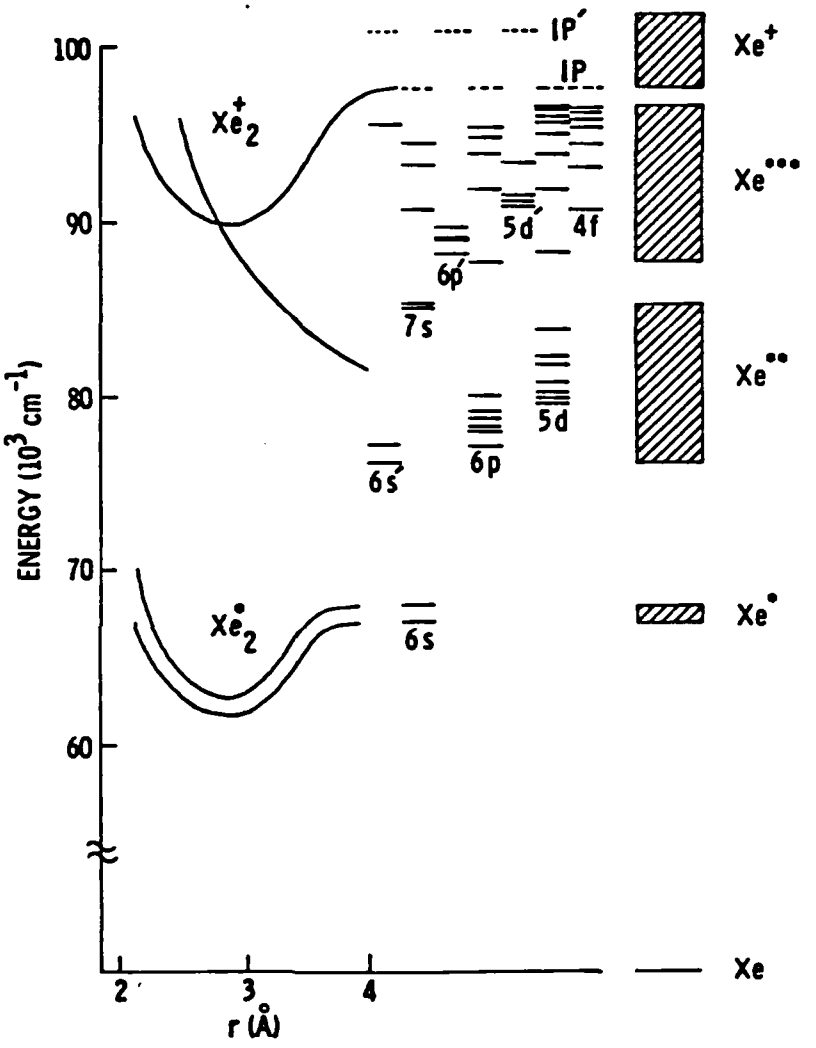

FIGURE 4.3-1 ENERGY LEVEL DIAGRAM FOR XENON

4.4 XeCl(B) Formation and Quenching

A potential energy diagram for XeCl is shown in Figure 4.4-1.

- Ion Channel

  The principal formation channel for XeCl(B) is through the reaction

  $$Xe^+ + Cl^- + M \rightarrow XeCl^* + M$$

  The branching ratios were found experimentally to be 80% into XeCl(B) and 20% into XeCl(C) [FCP80]. A secondary reaction involves the diatomic ion,

  $$Xe_2^+ + Cl \rightarrow XeCl^* + Xe$$

  This is assumed to have the same branching ratios.

- Neutral Channel

  As mentioned previously, the upper laser level is also formed through the neutral reactions,

  $$Xe^{**} + HCl(v = 0,1) \rightarrow XeCl^* + H$$

  and

  $$Xe^* + HCl(v = 1) \rightarrow XeCl^* + H$$

  The branching ratios for these reactions are not known, but are assumed to be the same as for the ion channel. At a power density of 1 MW/cm^3 the neutral channel accounts for roughly 25% of the B-state pumping.

<u>XeCl(B) and XeCl(C) State Mixing</u>. The XeCl(B) and XeCl(C) states are formed in upper vibrational levels and relax quickly at pressures above one atmosphere. While the molecules are in the upper levels, the effect of neutral collisions is to increase the B/C ratio [BS80]. Once they reach the lower vibrational levels, the effect of neutral collisions is reversed. In fact, the high pressure population densities derived from the fluorescence intensity ratio indicate that the C state is located about 230 cm^{-1} below the B state. The rate constant for B-C mixing with Ne is 8×10^{-13} cm^3/s [BS80], which is close

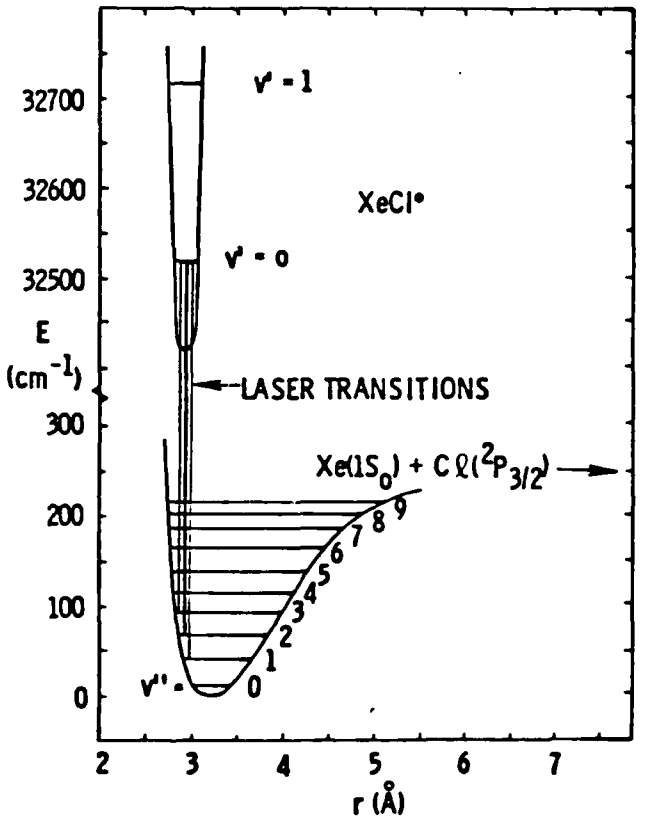

FIGURE 4.4-1 POTENTIAL ENERGY DIAGRAM FOR XeCl

to the two-body Ne quenching rate of 1 X 10^{-12} cm^3/s measured by Finn et al [FCP80]. In the model, the XeCl(B) quenching reactions with Ne, Xe and HCl are all assumed to mix the B and C states. Electrons are also allowed to mix the B and C states with a rate constant of 3 X 10^{-7} cm^3/s. The presence of electron mixing does not significantly influence the B state density in the absence of lasing, but it does affect the saturation of the B state and the degree to which C state energy is extracted.

Quenching of XeCl(B). In addition to mixing with the C state, the B state is quenched to the X state through superelastic collisions with electrons [HR79]. This rate is about 5 X 10^{-8} cm^3/s while the forward rate is 1 X 10^{-8} cm^3/s. There is also assumed to be another quenching reaction with electrons, which may involve higher lying states of XeCl. This process is assigned a rate constant of 2.5 X 10^{-7} cm^{-3}/s, based on our measured saturation intensity as a function of power density. The B and C state radiative lifetimes are taken to be 11 ns and 120 ns, respectively.

Clearing of XeCl(X). The clearing of ground state XeCl is essential for efficient laser operation. The measured clearing rates by neutral collisions are very slow [WE80]. However, recent attempts to repeat this experiment have been unsuccessful [Pa81]. Measurements of sidelight saturation as a function of intracavity intensity made during Phase I indicate that bottlenecking is not a problem, either in He or Ne buffers. Therefore, the ground state must be cleared rapidly with respect to the stimulated emission rate. In order to provide an adequate clearing rate in the model, it is assumed that the XeCl(X) and XeCl(A) states are mixed by electrons with a rate constant of 3 X 10^{-7} cm^3/s. Since the A state is dissociative, this acts as a direct loss, which effectively clears the ground state.

4.5 Optical Extraction

Small-Signal Gain. The gain cross section has been calculated as a function of wavelength and equilibrium temperature using spectroscopic data for the positions of the bandheads and measured Frank-Condon factors [THT76]. The data is plotted in Figures 4.5-1 and 4.5-2 for 300°K and 600°K, respectively.

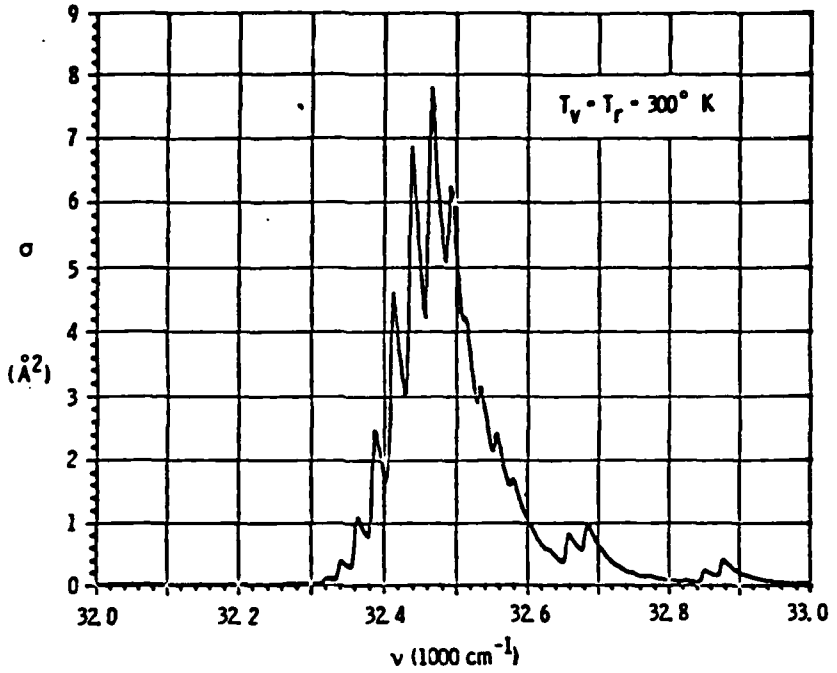

FIGURE 4.5-1 XeCl (B→X) GAIN CROSS SECTION

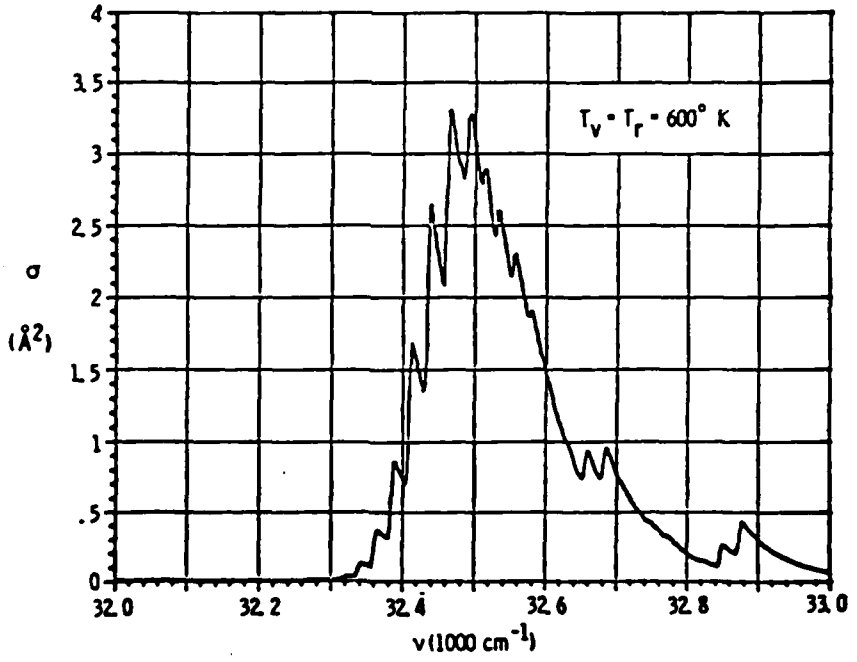

FIGURE 4.5-2 XeCl (B→X) GAIN CROSS SECTION

The peak cross section varies from 7.8 X 10^{-16} cm^2 to 3.3 X 10^{-16} cm^2 over this range. In the laser discharge, it is probable that the vibrational temperature of the upper level does not remain in equilibrium with the background gas, especially during lasing when the loss of v' = 0 by simulated emission reaches 2 X 10^9 s^{-1}. In the absence of detailed vibrational relaxation data in XeCl, the peak cross section has been chosen to give agreement with measured small-signal gain data. A value of 3.8 X 10^{-16} cm^2 is used in the model.

Transient Absorption. Transient absorption at the laser wavelength is due primarily to three species: Xe**, Xe_2^+, and Cl^-. The cross sections are 5 X 10^{-18} cm^2, 2.5 X 10^{-17} cm^2, and 2.2 X 10^{-17} cm^2, respectively [Wa80] [Ro69]. In a neon buffer at 5 atm, absorption by Xe_2^+ and Cl^- are about equally important while Xe** is a factor of two lower. The absorption is saturable in all three cases, but the saturation intensities are much higher than that for the gain. There is also some absorption by XeCl(X), which is assumed to remain in vibrational equilibrium with the gas, but there is enough to cause bottlenecking under lasing conditions.

Cavity Model. The cavity model assumes uniform intensity within the resonator with a decay time determined by the output coupling and the cavity length,

$$\tau_c = \frac{L_c}{c \ln M}$$

where M is the unstable resonator magnification. This optical model has been compared with a detailed Rigrod analysis, and the calculated extraction efficiencies are in excellent agreement for magnifications up to 10. Injection locking is treated as a photon source of known intensity and pulse length.

All the rate constants and cross sections used in the model are summarized in Table 4.5-1.

4.6 Model Results

Correlation with Phase I Experiments. The parameters for the Phase I baseline simulation are given in Table 4.6-1. The model results are shown in Figures 4.6-1 through 4.6-5. The steady-state voltage and current are in excellent agreement with measured values. Even the successive reflections

TABLE 4.5-1 DATA BASE FOR XeCl LASER MODEL

Reaction	Value	Unit	Reference
$XeCl(B) \rightarrow Xe + Cl + h\nu$	11	ns	[HD78]
$XeCl(B) + h\nu \rightarrow Xe + Cl + 2h\nu$	3.8×10^{-16}	cm^2	
$Cl^- + h\nu \rightarrow Cl + e^-$	2.2×10^{-17}	cm^2	[Ro69]
$Xe_2^+ + h\nu \rightarrow Xe^+ + Xe$	2.5×10^{-17}	cm^2	[Wa80]
$Xe^{**} + h\nu \rightarrow Xe^+ + e^-$	5×10^{-18}	cm^2	
$Xe_2^+ + e^- \rightarrow 2Xe$	$2.66 \times 10^{-6} \exp\left(\frac{300^\circ K}{T_e}\right)^{0.6}$	cm^3/S	[SBS77]
$Xe^+ + Cl^- + M \rightarrow XeCl(B) + M$	7×10^{-7}	cm^3/S	[BW80] [MWB80]
$Ne^* + Xe \rightarrow Ne + Xe^+ + e^-$	7.4×10^{-11}	cm^3/S	[La81]
$Xe^* + HCl \rightarrow$ products	5.6×10^{-10}	cm^3/S	[KVS79]
$Xe^{**} + HCl \rightarrow XeCl(B) + H$	1.6×10^{-9}	cm^3/S	
$XeCl(C) \rightarrow Xe + Cl + h\nu$	120	ns	[HD78]
$XeCl(X) + HCl \rightarrow$ products	2.2×10^{-11}	cm^3/S	[WE80]
$XeCl(X) + Xe \rightarrow$ products	5.6×10^{-12}	cm^3/S	[WE80]
$XeCl(X) + Ne \rightarrow$ products	1×10^{-13}	cm^3/S	[WE80]
$Xe^+ + Xe + He \rightarrow Xe_2^+ + He$	1.1×10^{-31}	cm^3/S	[Ch63]
$Xe^+ + Xe + Ne \rightarrow Xe_2^+$	2×10^{-31}	cm^3/S	
$XeCl(B) + HCl \rightarrow$ products	1.4×10^{-9}	cm^3/S	[FCP80]
$XeCl(B) + Xe \rightarrow$ products	3.2×10^{-11}	cm^3/S	[FCP80]
$XeCl(B) + Ne \rightarrow$ products	1×10^{-12}	cm^3/S	[FCP80]
$XeCl(B) + e \rightarrow XeCl(C) + e$	3×10^{-7}	cm^3/S	
$XeCl(B) + e \rightarrow XeCl(X) + e$	5×10^{-8}	cm^3/S	[HR079]
$XeCl(B) + e \rightarrow$ products	2.5×10^{-7}	cm^3/S	
$XeCl(X) + e \rightarrow$ products	3×10^{-7}	cm^3/S	

TABLE 4.6-1 PHASE I BASELINE PARAMETERS

Pressure	p (atm)	4
Active Volume	LXwXd(cm^{-3})	90 x 4 x 4
Stored Energy	U_o (J)	205
Pulse Length	τ_p (ns)	120
Impedance Matching	V_o/V_{ss}	3
Power Density	$\mathcal{P}$(MW/cm^3)	0.76
Charging Voltage	V_o (kV)	28
Characteristic Impedance	R_o (Ω)	0.45
Dielectric Stress	E_w (kV/cm)	68
Switch Inductance	L_s (nH)	3
Head Inductance	L_d (nH)	7
Cavity Length	L_c (cm)	120
Magnification	M	5

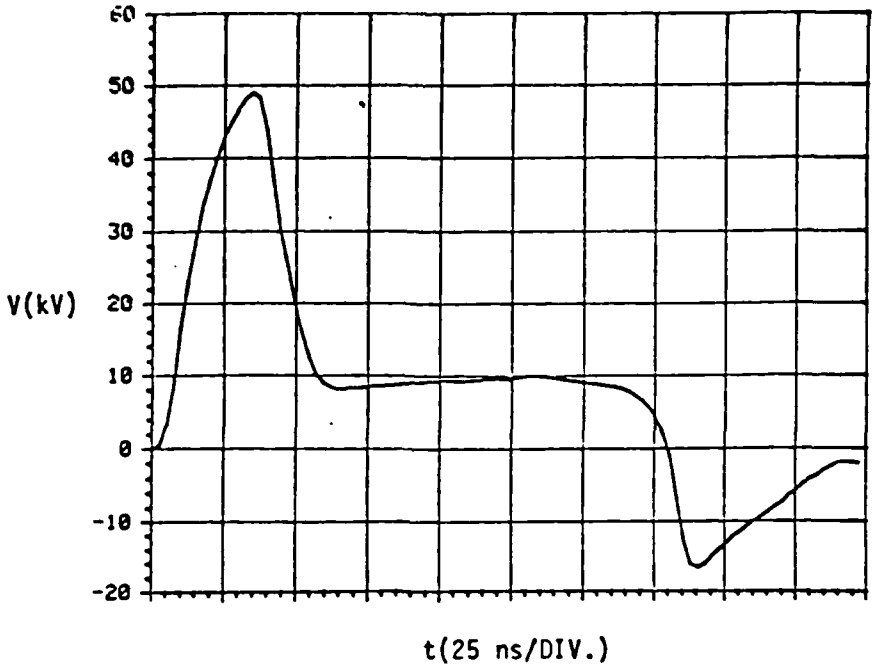

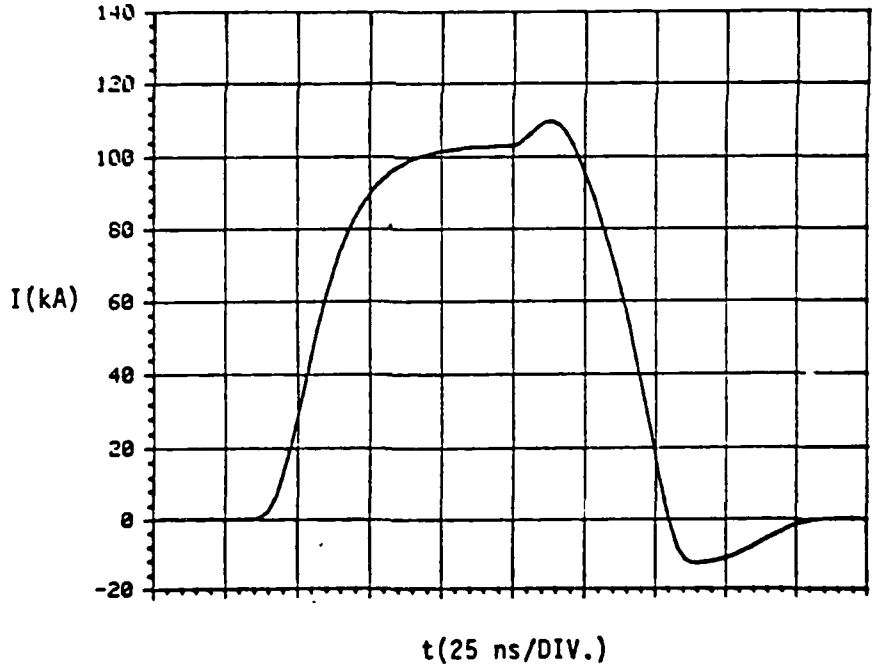

FIGURE 4.6-1 VOLTAGE AND CURRENT WAVEFORMS: PHASE I BASELINE

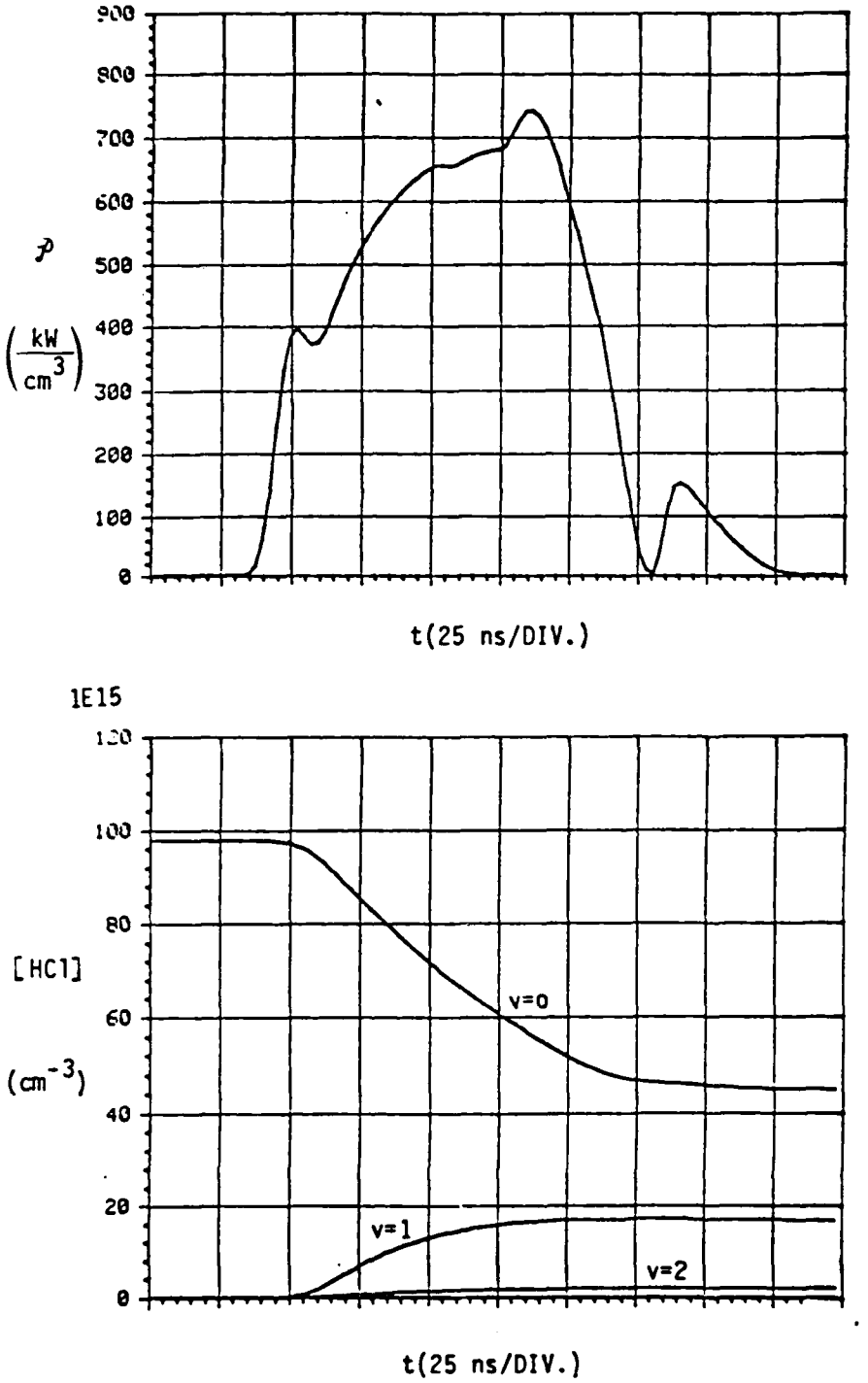

FIGURE 4.6-2 POWER DENSITY AND HCl(v) POPULATIONS: PHASE I BASELINE

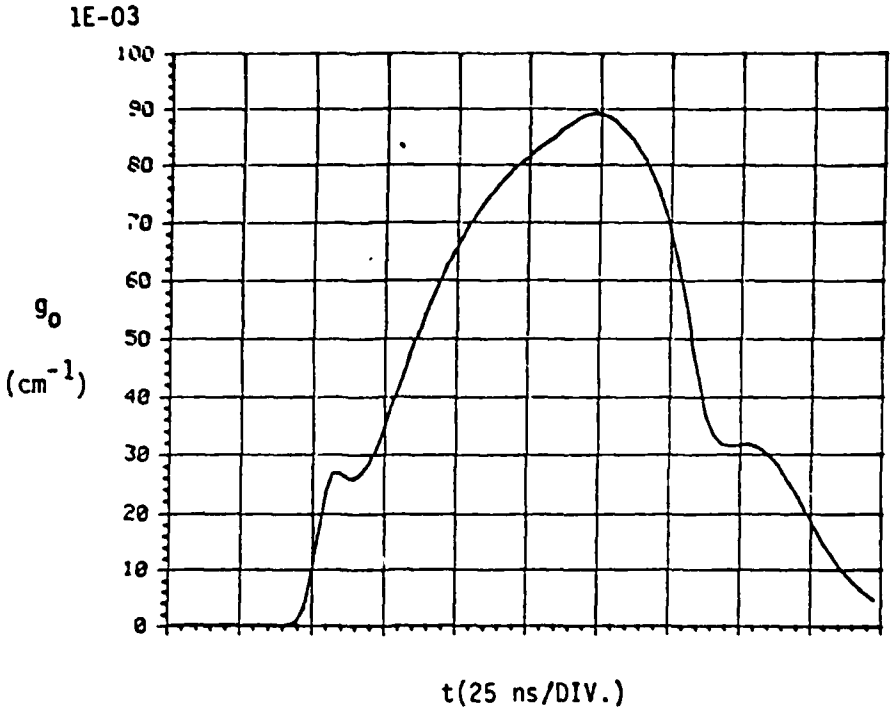

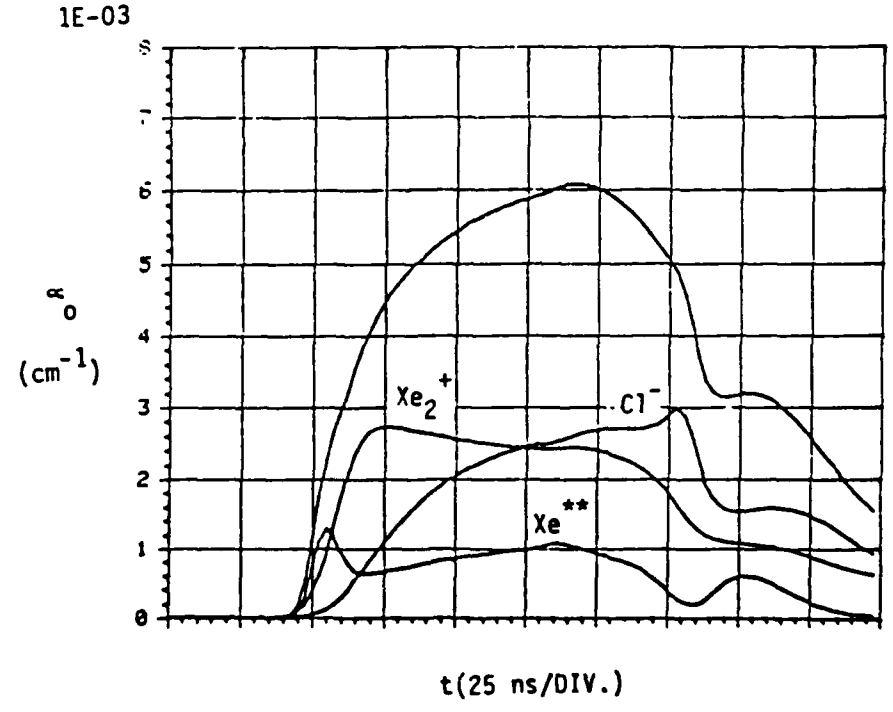

FIGURE 4.6-3 SMALL-SIGNAL GAIN AND ABSORPTION: PHASE I BASELINE

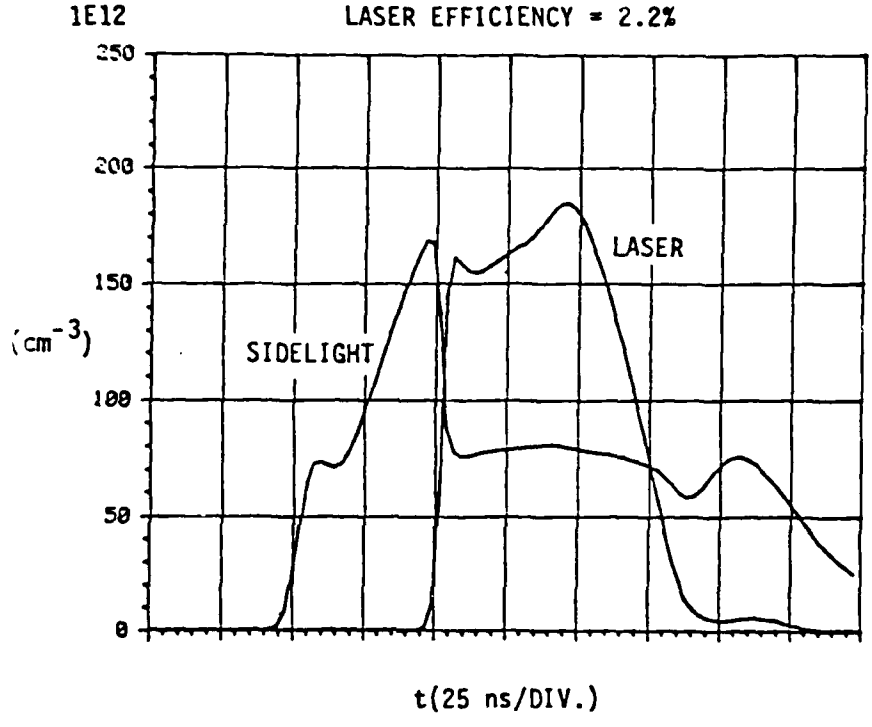

FIGURE 4.6-4 LASER OUTPUT AND SIDELIGHT FLUORESCENCE: PHASE I BASELINE

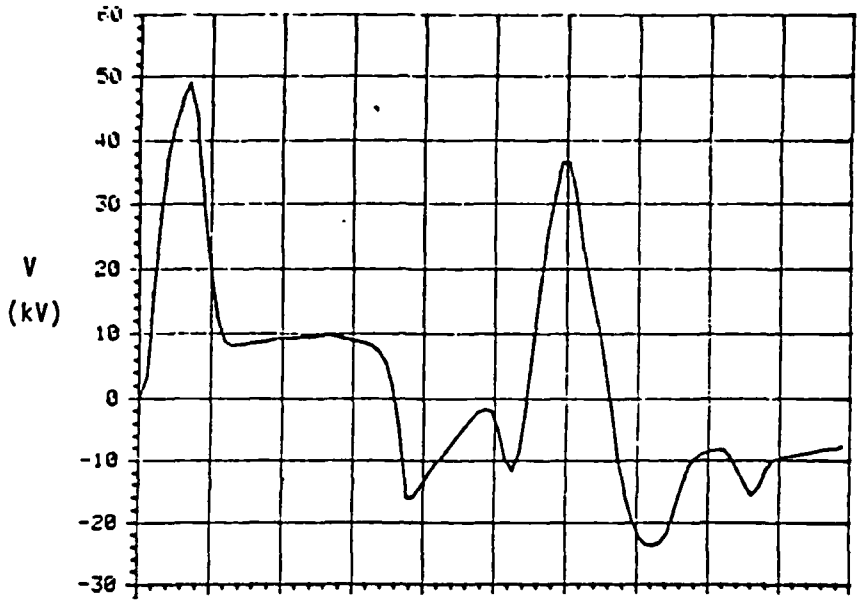

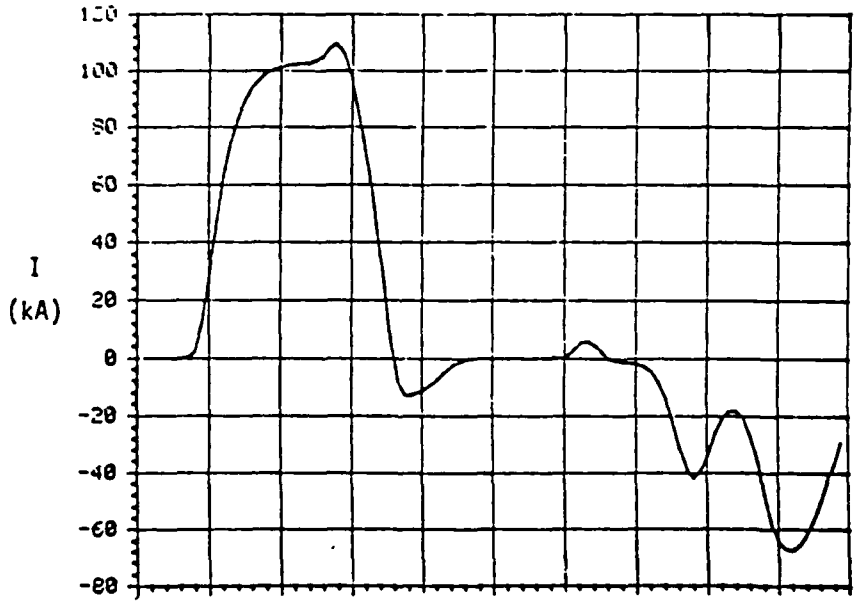

FIGURE 4.6-5 VOLTAGE AND CURRENT WAVEFORMS: PHASE I BASELINE

and inductive effects evident in the voltage waveform are in qualitative agreement with experiment. The early bump on the sidelight fluorescence trace, which is indicative of neutral channel pumping, is clearly seen in the experimental data. The laser pulse is about 70 ns wide. The peak small signal gain is 8.9% cm^{-1} and the absorption is 0.6% cm^{-1}. The overall laser efficiency is 2.2%, which is broken down as 52% energy transferred to the discharge, 12% formation of XeCl and 36% optical extraction. These numbers will be compared with experimental values in the next section.

Critical Constants. All of the constants used in the model were taken from the literature with the exception of those determined under this program by direct comparison with experiment. The latter are listed below along with the quantities from which they are derived.

Stimulated Emission Cross Section	- Small Signal Gain
HCl Dissociation Cross Section	- Formation Efficiency
Neutral Channel Branching Ratio	- Shape of Sidelight Fluorescence
Electron Quenching of XeCl(B)	- Saturation Intensity VS P
Direct Ionization of Xe	- Breakdown Time
Electron Mixing of XeCl(X) and XeCl(A)	- Absence of Bottlenecking

The most important constant which needs further study is the dissociation cross section for HCl. This process not only controls formation efficiency, but also the depletion of HCl which sets a limitation on energy loading. Observations which will lead to a better resolution of this quantity are (1) measurement of HCl concentration before and directly after the discharge, and (2) parametric studies of XeCl sidelight fluorescence versus HCl concentration.

Parametric Study. A limited parametric study centered around the Phase I baseline was conducted to determine the most efficient operating regime. Figure 4.6-6 shows the transfer and laser efficiencies versus charging voltage for three different pressures. A steady increase in efficiency with pressure is indicated. However, when one holds the absolute partial pressures fixed instead of the fractional concentrations, then the dependence on total pressure is much less pronounced. Figure 1.2.6-32 shows the extraction and laser efficiencies as a function of resonator magnification, and Figure 1.2.6-33 indicates the benefit of injection locking as the cavity length is increased.

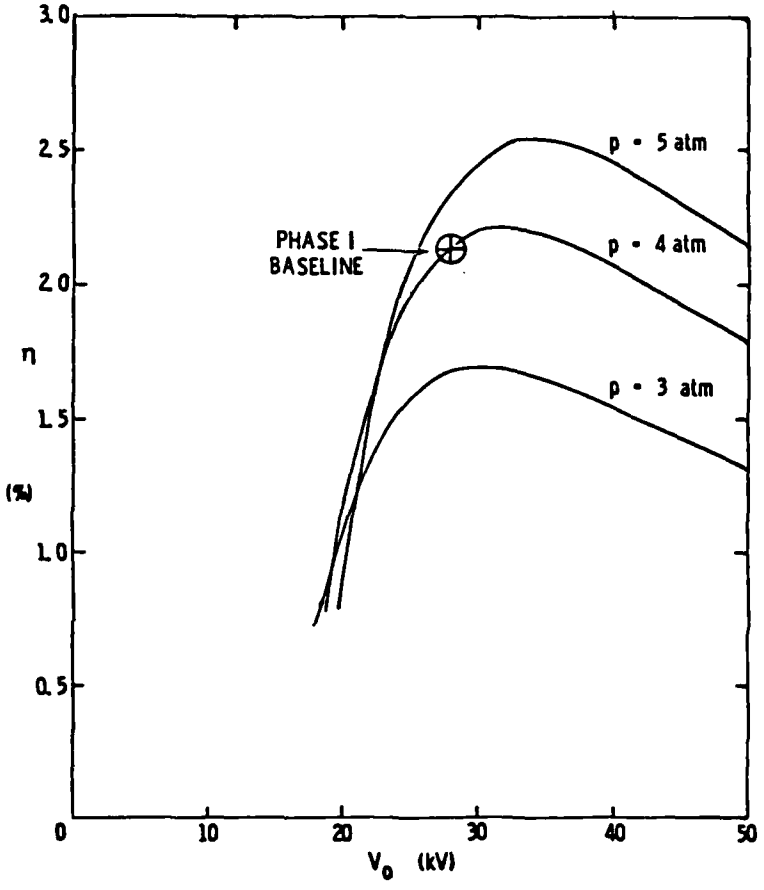

FIGURE 4.6-6 LASER EFFICIENCY VS CHARGING VOLTAGE

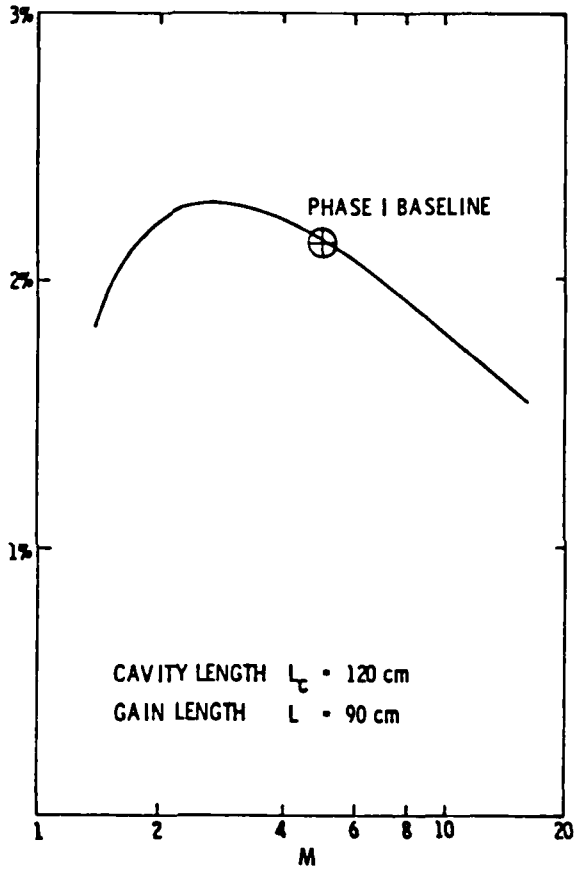

FIGURE 4.6-7 LASER EFFICIENCY VS RESONATOR MAGNIFICATION

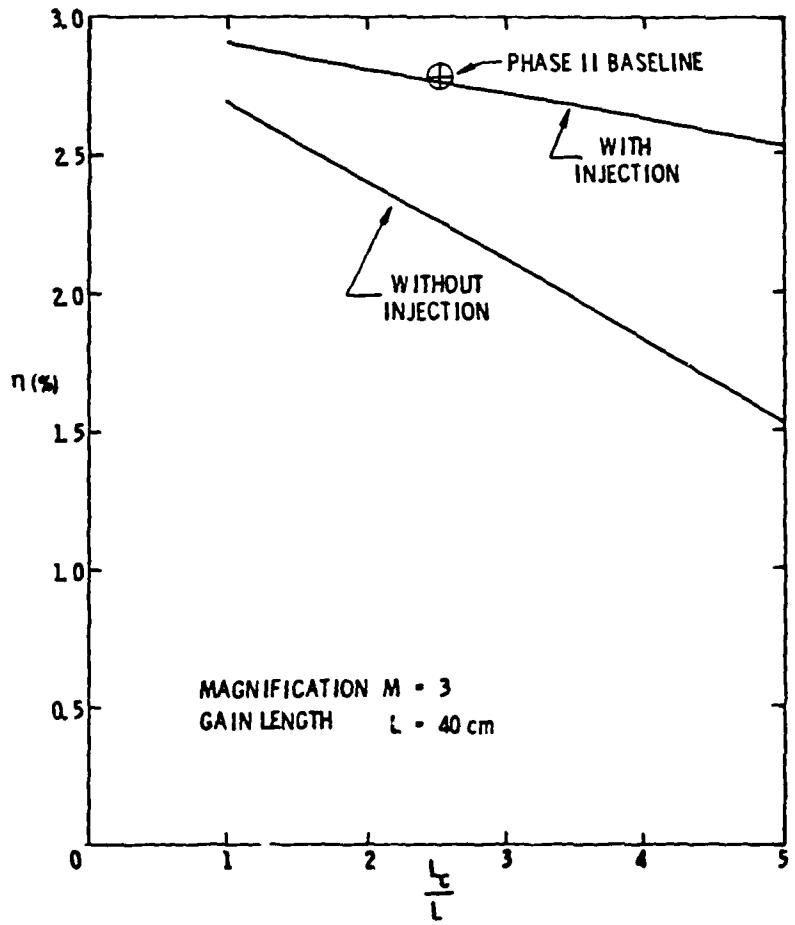

FIGURE 4.6-8 LASER EFFICIENCY VS CAVITY LENGTH WITH AND WITHOUT INJECTION LOCKING

5.0 ANALYSIS OF EXPERIMENTAL RESULTS

5.1 Impedance Matching

One of the critical factors influencing laser efficiency is transfer of energy from the PFL to the discharge. Power transfer is most efficient when the load impedance is equal to the line impedance, R_o. A quick look at the equivalent circuit of Figure 5.1-1(a) reveals that this matching is achieved for a transmission line when the charging voltage, V_o, is equal to twice the discharge voltage, V. (For a Blumlein line the charging voltage should equal the discharge voltage.) The quasi-steady-state discharge voltage, for a given gas mixture and pressure, is a characteristic function of current, shown in Figure 5.1-1(b), as the boundary between the two shaded regions. The term "quasi-steady-state" is used because the discharge never reaches a true steady-state due to such processes as gas heating, depletion of the halogen donor, and growth of nonuniformities. However, for a time on the order of 100 ns after breakdown, the discharge voltage maintains a nearly constant value which is a function of the current. At the same time, the line is supplying a constant voltage at a fixed output impedance. The operating point for the system is then given by the intersection of the discharge characteristic and the "load line" of the driver as indicated in Figure 5.1-1(b). If the charging voltage is set to maximize the transfer efficiency, then the line impedance determines the power density.

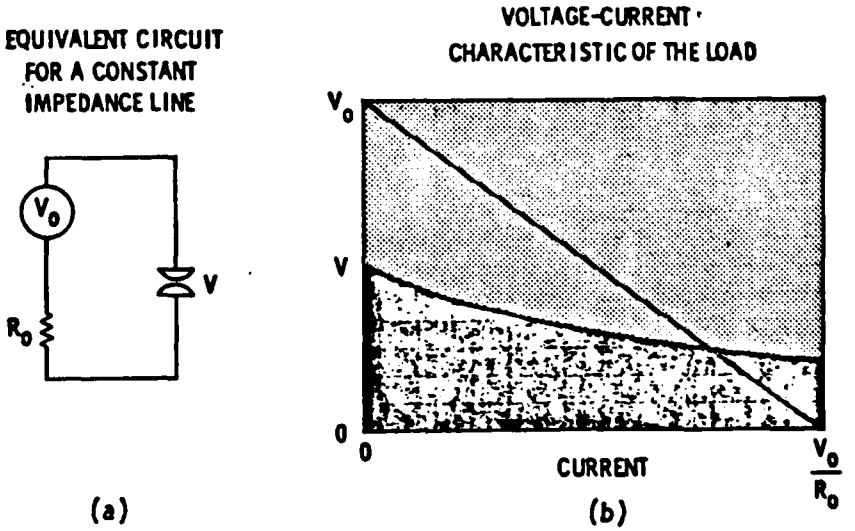

FIGURE 5.1-1 IMPEDANCE MATCHING

In the discussion above, we refer to the quasi-steady-state regime, but the discharge must first break down. The initial impedance of the discharge after preionization is on the order of 1 MΩ. The voltage across this load approaches the full charging voltage for a transmission line and double the charging voltage for a Blumlein line. If the driver is set up for maximum power transfer, then the peak voltage will be twice the quasi-steady-state voltage in either configuration. The ionization rate at this voltage may be such that a considerable delay is introduced in bringing the electron density from 10^7 cm^{-3} to 10^{15} cm^{-3}. An increase in breakdown time is clearly evident in Figure 5.1-2 as the charging voltage is lowered from 28 kV to 16 kV. The quasi-steady-state voltage in this case is about 10 kV. However, at the lower power densities, this value is never reached due to incomplete vibrational excitation of the HCl.

5.2 Sidelight Fluorescence and Saturation Intensity

A systematic analysis of sidelight fluorescence was made during Phase I to determine the laser saturation intensity and to establish whether bottlenecking was a problem. The sidelight measurement was made using a vacuum planar photodiode, with appropriate filters for eliminating wavelengths greater than 310 nm. The discharge was viewed at 90° to the optical axis. The resonator consisted of external mirrors with Brewster angle windows, so that the cavity could be easily spoiled. The scope traces are shown in Figure 5.2-1 for two values of output mirror reflectivity and three charging voltages. The lower curve in each case was taken with lasing and the middle curve without lasing. However, even with the cavity spoiled, considerable superfluorescence was observed which resulted in some residual saturation of the sidelight. The upper dashed curve is an extrapolation representing the expected sidelight without superfluorescence, based on observed pulse shapes at lower voltages.

The ratio of sidelight fluorescence with and without lasing is a measure of the saturation of the upper laser level. This quantity is plotted in Figure 5.2-2 as a function of intracavity intensity. In the absence of bottlenecking, the upper state density is given by

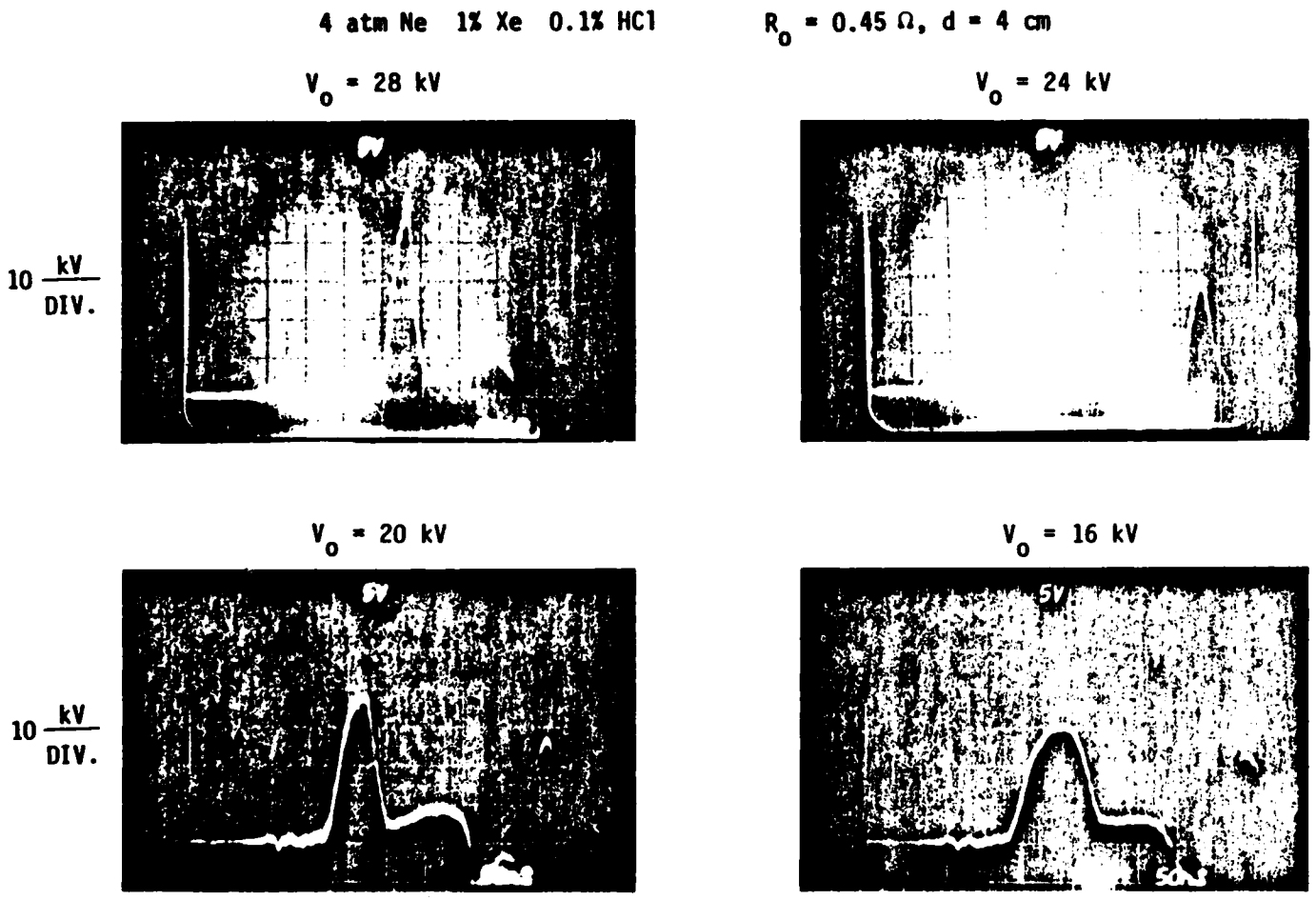

FIGURE 5.1-2 LIMITATIONS ON IMPEDANCE MATCHING

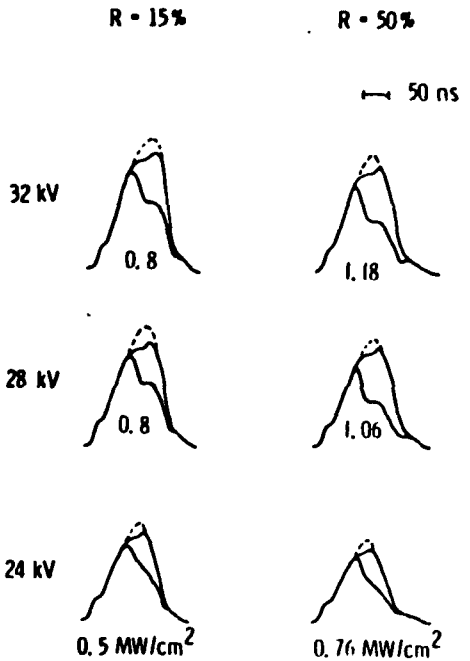

FIGURE 5.2-1 SIDELIGHT MEASUREMENTS WITH AND WITHOUT LASING

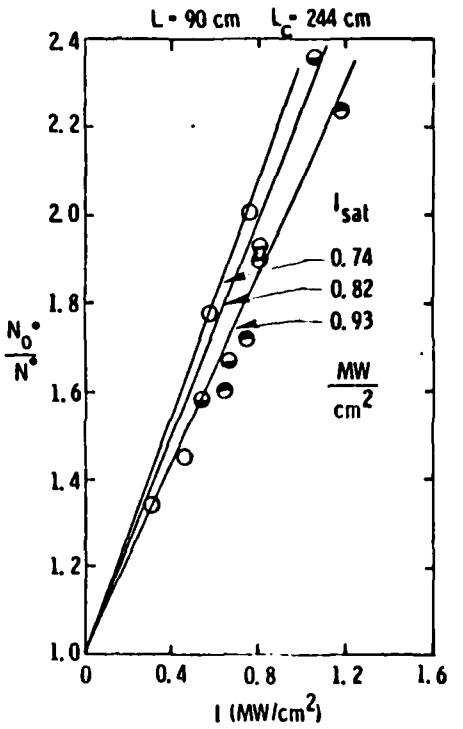

FIGURE 5.2-2 GAIN SATURATION (2% Ne 0.2% HCl in 2 atm He)

$$N^* = \frac{N_o^*}{1 + I/I_{sat}}$$

where N_o^* is the density without lasing. A plot of N_o^*/N^* versus I should be a straight line with slope equal to $1/I_{sat}$. No deviation from straight line behavior is evident in Figure 5.2-2, which indicates that bottlenecking is not a problem, at least up to I = 1.2 MW/cm^2. The saturation intensities are derived for three different power densities and plotted in Figure 5.2-3. The horizontal lines in this figure represent the saturation intensity based on neutral quenching only. The sloping lines were calculated by including electron quenching with a rate constant of 3 X 10^{-7} cm^3/s. This value seems to be consistent with the data.

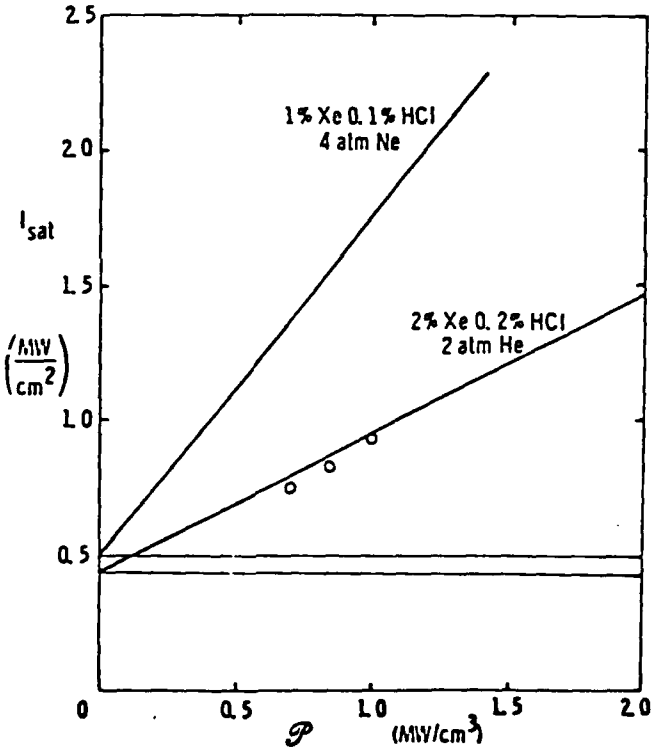

FIGURE 5.2-3 SATURATION INTENSITY OF XeCl

The model prediction for the sidelight is shown in Figure 5.2-4. The shape is very similar to that observed, including the knee on the leading edge of the pulse which is due to neutral channel pumping.

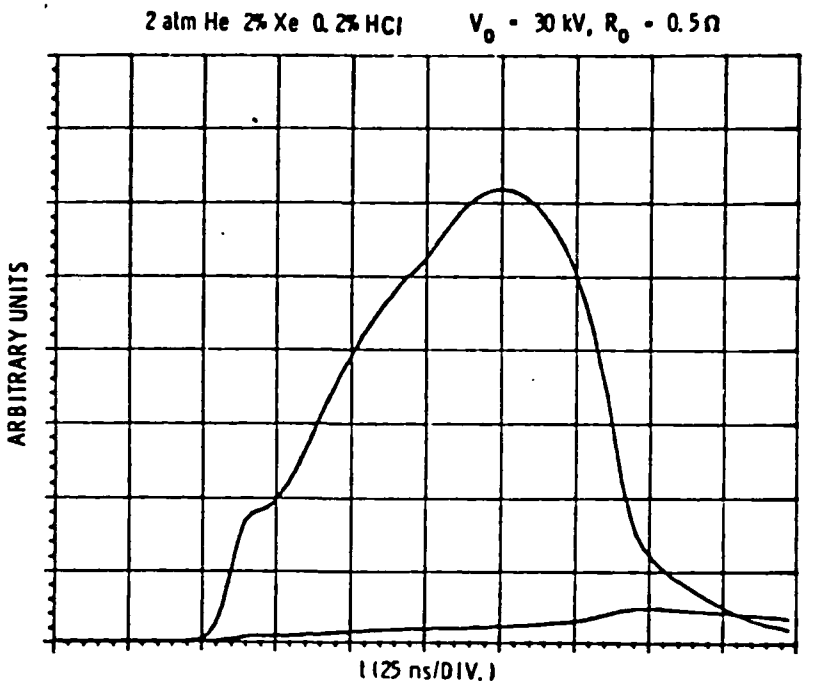

FIGURE 5.2-4 MODEL PREDICTIONS OF SLIDELIGHT FLUORESCENCE

5.3 Small Signal Gain and Loss Measurements

Small signal gain and loss were measured using a doubled CMX-4 dye laser. The wavelength was tunable from 300 nm to 313 nm and the linewidth was 5 cm^{-1}. After making a single pass through the XeCl laser, the beam was sent through a spatial filter to eliminate superfluorescence. Both incident and transmitted waveforms were recorded and compared to obtain gain and absorption coefficients. Several shots were taken under each set of conditions. The shot-to-shot fluctuation was typically less than 5%.

Oscilloscope traces of the transmitted signal are shown in Figure 5.3-1 for a helium mixture at two different wavelengths. The first feature on each trace is a timing mark for synchronization of the incident and transmitted pulses. Figure 5.3-2 shows similar data obtained in a neon mixture. The superfluorescence was stronger in this case and some residual signal is evident in the trace at 312 nm. This background was corrected for by taking a shot without the dye pulse and subtracting.

2 atm He 2% Xe 0.2% HCl

V_o = 28 kV, R_o = 0.5 Ω, d = 3.5 cm

GAIN

λ = 308 nm

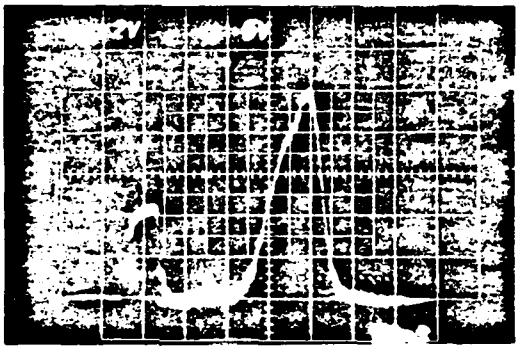

6.5% cm^{-1}

50 ns/DIV.

LOSS

λ = 312 nm

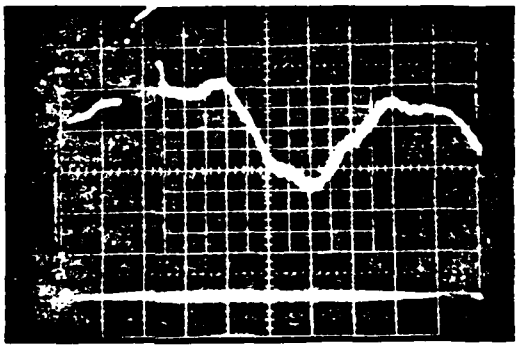

0.7% cm^{-1}

50 ns/DIV.

FIGURE 5.3-1 MEASURED GAIN AND LOSS IN XeCl

AD-A133 078 RAMAN-SHIFTED XECL LASER DEVELOPMENT FOR A SPACEBORNE BLUE-GREEN SOURCE..(U) NORTHROP RESEARCH AND TECHNOLOGY CENTER PALOS VERDES PENINSUL.. E A STAPPAERTS ET AL.

2/2

UNCLASSIFIED FEB 82 NRTC-82-5R N00123-80-C-1137 F/G 20/5 NL

END

DATE FILMED

DTIC

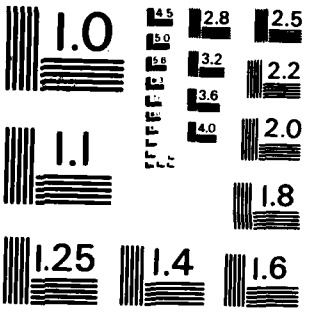

4 atm Ne 1.88% Xe 0.13% HCl

V_o = 30 kV, R_o = 0.45 Ω, d = 4 cm

GAIN
308 nm

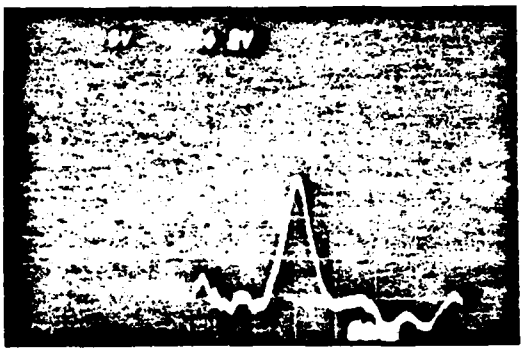

8.4% cm^{-1}

LOSS
312 nm

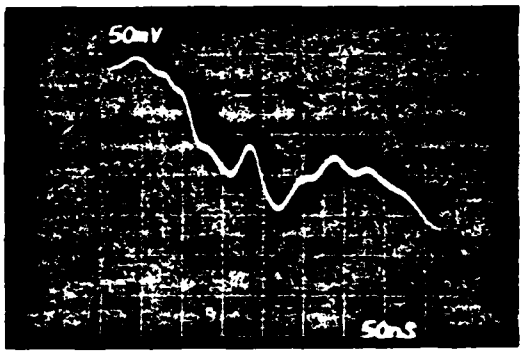

0.7% cm^{-1}

FIGURE 5,3-2 MEASURED GAIN AND LOSS IN XeCl

The measured gain and loss coefficients are plotted in Figure 5.3-3 as a function of wavelength. The solid curve was generated from spectroscopic data for XeCl and fitted to the data points. The fit indicates an XeCl(B) vibrational temperature of about 500°K. The background absorption increases slightly at long wavelengths, which is characteristic of the Xe_2^+ component. On the short wavelength side there is probably some absorption due to the XeCl(X) ground state.

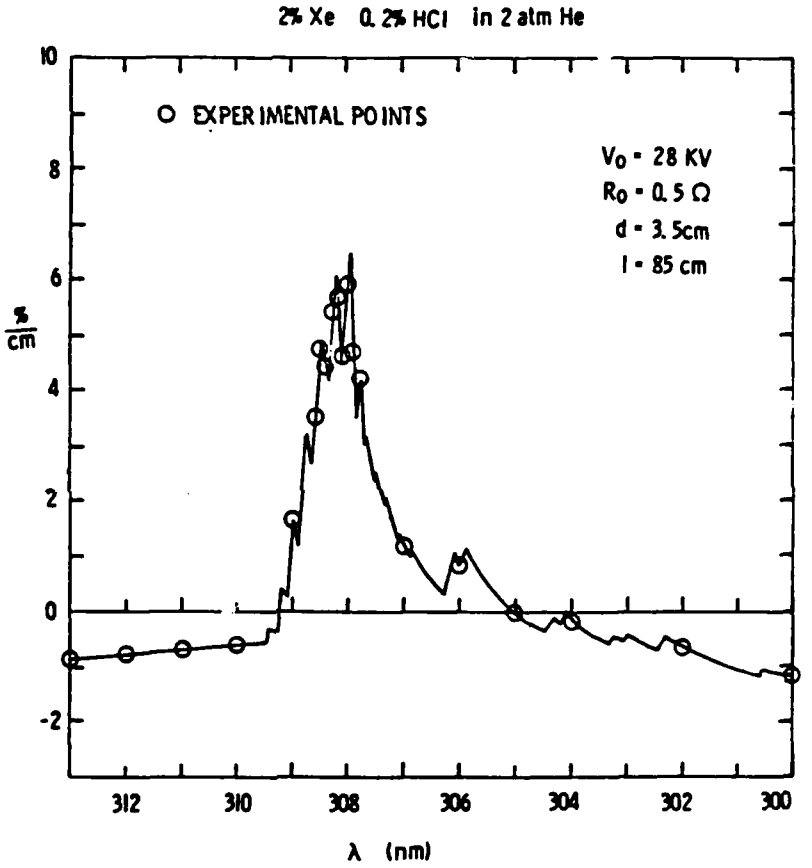

FIGURE 5.3-3 GAIN AND ABSORPTION IN XeCl VS λ

The experimental gain and loss waveforms were digitized and used in an optical cavity model to predict the laser performance. Laser output and saturated gain are shown in Figure 5.3-4. The output pulse is 60 ns long with a peak intensity of 1.6 I_{sat}. With I_{sat} = 0.8 MW/cm^2, the output energy is 1.2J in good agreement with the experimental value for these conditions. The ratio of small-signal gain to loss varies during the pulse as shown in Figure 5.3-5. In the helium mixture this ratio is typically 8 to 10,

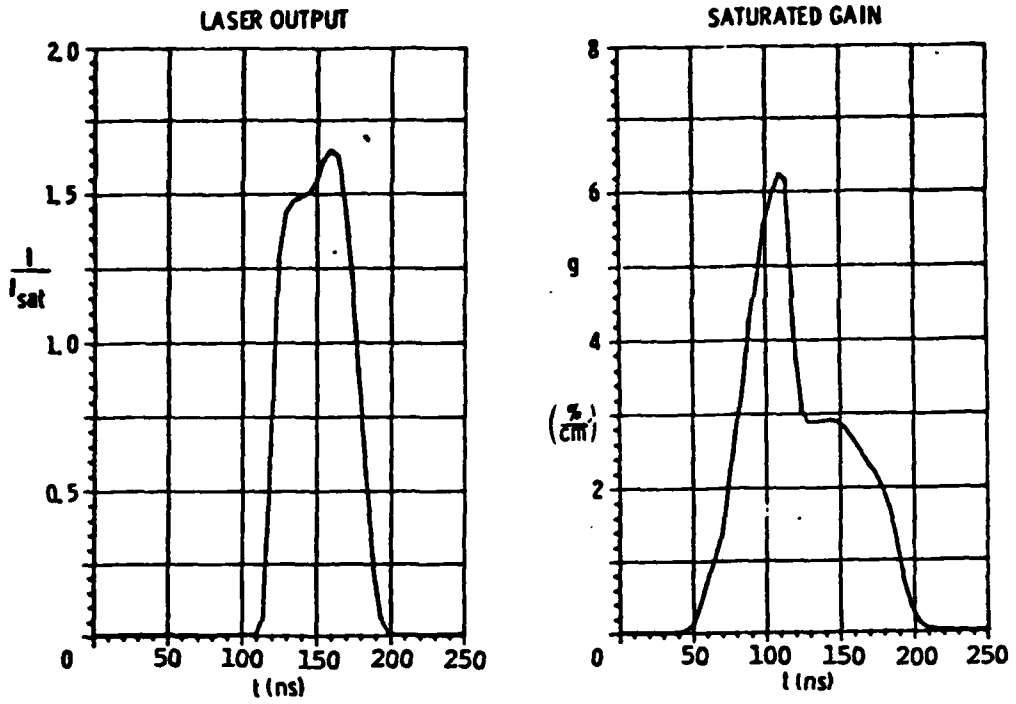

FIGURE 5.3-4 CAVITY MODEL RESULTS

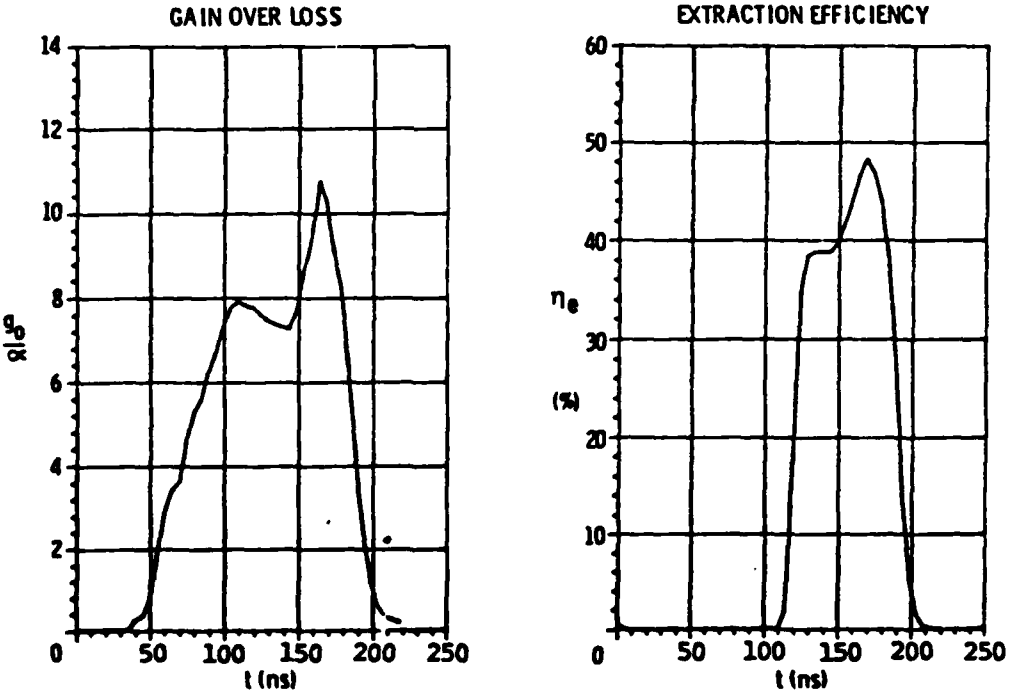

FIGURE 5.3-5 CAVITY MODEL RESULTS

while in neon mixtures it varies from 12 to 15. The instantaneous, extraction efficiency in Figure 5.3-5 has a maximum value of 48% but the integrated extraction is only 30%.

5.4 Analysis of Laser Efficiency

A detailed breakdown of the experimental laser efficiency was made for comparison with the model and to determine where improvements could be made. The various factors going into the efficiency are defined in Table 5.4-1. They are written as instantaneous or power efficiencies. The corresponding energy efficiencies are simply obtained by integrating over time. The starting point is the energy stored on the Blumlein PFL:

$$U_0 = \frac{V_0^2}{R_0} \tau_p$$

The power deposited in the discharge is $\mathcal{P}$xAxL where $\mathcal{P}$ is the power density and AxL the active volume. The energy transfer efficiency takes into account the losses in the switch and in the line due to skin effect. The power going into the upper laser level is $g_0 I_{sat}$ per unit volume and the laser output power is $I_{out}A$. All of these quantities were experimentally determined and the resulting efficiencies are given in Table 5.4-1 for helium and neon. The first number in each entry is the energy efficiency while the number in parentheses is the power efficiency.

TABLE 5.4-1 DEFINITION OF EFFICIENCIES

TRANSFER		FORMATION		EXTRACTION		TOTAL
η_t		η_f		η_e		η
$\frac{\mathcal{P}AL}{V_0^2/R_0}$	X	$\frac{g_0 I_{sat}}{\mathcal{P}}$	X	$\frac{I_{out}}{g_0 L\ I_{sat}}$	=	$\frac{I_{out}A}{V_0^2/R_0}$
				INTRINSIC		

V_o = 28 kV	R_o = 0.45	d = 4 cm
	2 atm He	4 atm Ne
TRANSFER η_t	70% (84%)	46% (56%)
FORMATION η_t	4.8% (5.0%)	13% (14%)
EXTRACTION η_e	28% (42%)	34% (47%)
TOTAL η	0.9% (1.8%)	2.1% (3.8%)
LASER OUTPUT UC	1.9 J	4.4 J
PULSE LENGTH τ_Q	60 ns -	65 ns
POWER DENSITY	1.0 MW/cm^3	0.7 MW/cm^3
GAIN: g_o	6.5% cm^{-1}	8.4% cm^{-1}
SATURATION INTENSITY	0.8 MW/cm^2	1.2 MW/cm^2

TABLE 5.4-2 EXPERIMENTAL EFFICIENCY BREAKDOWN

REFERENCES

ARP 74 R. Azria, L. Roussier, R. Painean, and M. Tronc, Rev. Phys. Appl. (Paris) 9, 469 (1974)

AW 81 M. Allan and S. F. Wong, J. Chen, Phys. 74, 1687 (1981)

BS 80 H. C. Brashears, Jr. and D. W. Setser, J. Chen. Phys, 84 224 (1980)

BS 81 I. J. Bigio, M. Slatkine, Opt. Lett. 6, 336 (1981)

BW 80 J. N. Bardsley and J. M. Wadehra, Chom, Phys. Lett. 72 477 (1980)

CFM 79 R. F. Caristi, S. Friedman, S. S. Merz, and D. U. Turnquist, IEEE Trans. on Electron Devices, ED-26, 1427 (1979)

Ch 63 C. L. Chen, Phys. Rev. 131 2550 (1963)

Ch 73 T. Y. Chang, Rev. Sci. Instrum. 44, 405 (1973)

Ch 81 R. S. F. Chang, Naval Research Laboratory, unpublished

FI 78 M. R. Flannery, Chem. Phys. Lett., 56 143 (1978)

FCP 80 T.G. Finn, R.S. F. Chang, L. J. Palumbo, and L. F. Champagne, Appl. Phys. Lett. 36, 789 (1980)

HD 78 P. J. Hay and T. H. Dunning, Jr., J. Chom. Phys. 69, 2209 (1978)

He 66 D. R. Herschbach, Adv. Chom. Phys. 10, 319 (1966)

HR 79 A. U. Hazi, T. N. Rescingo, and A. E. Orel, Appl. Phys. Lett., 35, 477 (1979)

HRO 79 A. U. Hazi, T. N. Rescingo, and A. E. Orel, Appl. Phys. Lett. 35, 477 (1979(

Hs 76 J. Hsia, Appl. Phys. Lett. 30, 101 (1977)

JW 70 D. A. Jennings and E. D. West, Rev. Sci. Instr. 41, 565 (1970)

KVS 79 J. H. Kotts, J. E. Velazco, D. W. Setser, J. Chem. Phys. 71 1247 (1979)

La 81 J. Laudenslager, private communication (1981)

LD 78 S. Lawton and T. A. DeTemple, Contract Report No. AFAPL-TR-78-107 (December, 1978)

Ma 70 J. C. Martin, "Multichannel Gaps," Switching Note 10, Atomic Weapons Research Establishment, Aldermaston, England (1970) unpublished

MWB 80 W. L. Morgan, B. L. Whitten, and J. N. Bardsley, Phys. Rev. Lett., 45, 2021 (1980)

Pa 74 A. J. Palmer, Appl. Phys. Lett. 25, 138 (1974)

Pa 81 L. J. Palumbo, private communication

RL 76 L. Dube and A. Herzenberg, Phys. Rev. Lett. 38, 820 (1977)

Ro 69 D. E. Rothe, J. Quant. Spectrosc. Radiat. Transfer, 9, 49 (1969)

Ro 78 K. Rohr, J. Phys. B: Atom. Molec. Phys., 11, 1849 (1978)

SBS 77 Y-J Shiu, M. A. Biondi, and D. P. Sipler, Phys. Rev. A 15 494 (1977)

Se 80 D. Setser, Proc. 33rd GEC, Norman, Oklahoma, 67 (1980)

SLK 80 E. A. Stappaerts, W. H. Long, Jr., and H. Komine, Opt. Lett. 5, 4 (1980)

THT 76 J. Tellinghuisen, J. M. Hoffman, G. C. Tisone, and A.K. Hays, J. Chem Phys. 64, 2484 (1976)

Wa 80 W. R. Wadt, J. Chem. Phys. 73, 3915 (1980)

WB 78 J. M. Wadehra and J. N. Bardsley, Appl. Phys. Lett. 32, 76 (1978)

WE 80 R. W. Waynant and J. G. Eden, to be published.

END

DATE
FILMED

10 — 83

DTIC